9-5-2007

Raman Scattering Study of Supercritical Bi-Component Mixtures Injected into a Subcritical Environment

Young Man An

RAMAN SCATTERING STUDY OF SUPERCRITICAL BI-COMPONENT MIXTURES INJECTED INTO A SUBCRITICAL ENVIRONMENT

THESIS

Young Man An, Captain, ROKA

AFIT/GA/ENY/07-S01

DEPARTMENT OF THE AIR FORCE
AIR UNIVERSITY

AIR FORCE INSTITUTE OF TECHNOLOGY

Wright-Patterson Air Force Base, Ohio

The views expressed in this thesis are those of the author and do not reflect the official policy or position of the United States Air Force, Department of Defense, or the U.S. Government.

AFIT/GA/ENY/07-S01

RAMAN SCATTERING STUDY OF SUPERCRITICAL BI-COMPONENT MIXTURES INJECTED INTO A SUBCRITICAL ENVIRONMENT

THESIS

Presented to the Faculty

Department of Aeronautics and Astronautics

Graduate School of Engineering and Management

Air Force Institute of Technology

Air University

Air Education and Training Command

In Partial Fulfillment of the Requirements for the

Degree of Master of Science in Astronautical Engineering

Young Man An, BS

Captain, ROKA

September 2007

AFIT/GA/ENY/07-S01

RAMAN SCATTERING STUDY OF SUPERCRITICAL BI-COMPONENT MIXTURES INJECTED INTO A SUBCRITICAL ENVIRONMENT

Young Man An, BS

Captain, ROKA

Approved:

/signed/	5 September 2007
Paul I. King	Date
/signed/	5 September 2007
Richard D. Branam	Date
/signed/	5 September 2007
Mark F. Reeder	Date

Abstract

This research studies the species distribution profiles of methane/ethylene bi-components at downstream locations filled with subcritical nitrogen in a closed chamber. Unique thermodynamic and transport properties of supercritical fluids along with phase transition phenomena during fuel injection process can significantly change combustion characteristics inside a scramjet combustor. Plume properties of supercritical jets are of great interests to the studies of fuel/air mixing and subsequent combustion. The primary goal of this research is to help to clarify whether there is any preferential condensation within the condensed jets. The Raman Scattering technique is used to quantify spatial distribution of injected methane and ethylene. Each species distribution profile is developed in terms of mole fraction. Results demonstrated there is ethylene preferential condensation within the supercritical bi-component mixture of the jet. It also showed the condensation phenomenon is less desirable for combustion.

To My Great Country, Korea, and My Lovely Wife and Sons

Acknowledgments

The scope what was accomplished in this work far exceeded my own vision, and would not have been possible without patient instruction of many along the way.

I would like to express my sincere appreciation to my faculty advisor, Dr. Paul King for his guidance and encouragement throughout this effort and advising at key points. My appreciation also to my faculty members, Major Richard Branam, Dr. Mark Reeder for their critical advises.

I also would like to thank my sponsor, Dr. Mike Ryan, from the Air Force Propulsion Directorate for the support and knowledge that he provided me. Dr. Mike Ryan provided the patient teaching and the proper guidance form all the basics and presented genuine interest in the experiment to make this thesis an enjoyable experience.

Finally, I would like to give a great thanks to my lovely wife. Without her continuous support and dedication, I would not have achieved what I have in my life. Thank you for supporting and being with me throughout this long journey, once again.

In addition, there were many who provided assistance along the way. I would like thank the laboratory technicians, John Hixenbaugh for getting me out of trouble and his friendship.

Young Man, An

Table of Contents

List of Figures

Figure Page

Figure Page

Figure Page

Figure Page

Figure Page

Figure Page

List of Tables

Table Page

Nomenclature

Roman

a	Slopes
b	Intercepts
C	Constant
C_i	Molar density
d	Groove distance
d	Orifice diameter
dz	Path length of the laser in the sample
E_i	Molecular energy level
E	Electric field strength
E_0	Vibrational amplitude
h	Planck's constant
I_R	Raman signal intensity in Watts
I_0	Incident laser intensity in Watts
m	Diffraction order
M	Vibrational energy level
N	Number of atom
n_i	Number density of species i
n	$10^{-9}\ m$
N_A	Avogadro's number
P	Pressure
P	Induced dipole moment
P_R	Raman signal intensity in photon counts
P_0	Incident laser intensity in photon counts
R_e	Reynolds number
T	Temperature
u_∞	Jet velocity
u_0	Chamber velocity
X_i	Mole fraction of species i
z	Axial distance from nozzle exit

Greek

α	Polarizability
α_0	Inherent polarizability of the moleucule
β	Groove angle
δ	Jet divergence angle
σ	Integrated Raman cross section
ρ_0	Jet center line density
ρ_∞	Ambient density
μ	$10^{-6}\ m$

λ	Frequency
η	Differential Raman cross section
θ_i	Angle between the incident light and the reflected light
ν_0	Incident photon frequency
ν_m	Molecular vibrational frequency
Ω	Solid angle of collection
ϕ	Constants

Subscripts

CL	Center line
c	Property at critical point
c	Local axial centerline, core
chm	Property inside the chamber
inj	Property at injection condition
r	Ratio of injection property to critical property
rc	Ratio of injection property to chamber property

RAMAN SCATTERING STUDY OF SUPERCRITICAL BI-COMPONENT MIXTURES INJECTED INTO A SUBCRITICAL ENVIRONMENT

I. Introduction

Background

The human needs and desires of achieving high-speed flight led to the development of advanced air-breathing flight vehicles utilizing Supersonic Combustor Ramjet or scramjet technology which can increase the vehicle flight speed into the hypersonic regime (beyond Mach number of 5). The scramjet engine is the key enabling technology for future seamless space access facilitating the delivery of military power anywhere in the world in a couple of hours. Civil transport can also benefit from this technology in long distance travel. Traditional turbojet-based engines provide the flight speed around Mach 1-2. Ramjet engines can be operated in an extended Mach range (Mach 3-4) while the scramjet engine can provide the flight speed further into the hypersonic domain.

The scramjet engine is operated by burning fuel in a stream of supersonic air compressed by the forward speed of the aircraft. Unlike conventional jet engines, the scramjet has no moving parts such as rotating blades compressing the air. The most distinguishing difference between scramjet and ramjet engines is whether the core flow speed inside the combustor is supersonic or not. There is a strong normal shock in the ramjet inlet which causes the flow speed to decelerated below Mach one. While the

concept behind the scramjet is very simple, formidable problems must be overcome to achieve hypersonic flight. In general, as the vehicle speed increases, the vehicle will experience large heat loads that can cause serious problems on materials, structures or various aircraft components. The heat loads for different aircraft and components are shown in Figure 1. As can be seen, the heat loads of the Mach 6 Interceptor are significantly larger than that of the F-4 [1].

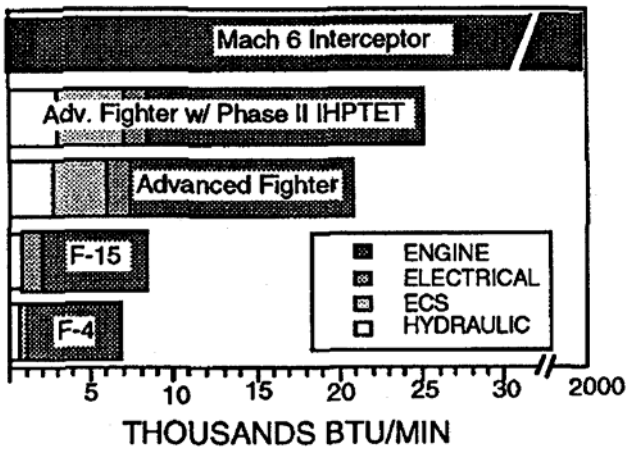

Figure 1. Maximum estimated excess heat loads for various aircraft [1].

The main heat source is in the engine where combustion takes place. In the case of the scramjet combustor, the entrance temperature is well over 2500K because of the supersonic flow speed and friction with the wall. Most metal is melted away and the structural integrity decreases under this extreme temperature condition. Therefore, the principal engineering challenge is using thermal management to control heat.

The conventional way to accommodate large amount of heat loads is using the fuel as a main coolant. This is done by directing the fuel flow across the heated combustor and re-circulating it back to the fuel tank, where the fuel can be cooled by exchanging the heat with outside low temperature air [1]. However, this re-circulating

system has a limitation for use in hypersonic aircraft due to the high stagnation temperature of the air. Another attractive method that has been undergoing extensive research is the use of endothermic fuel as a heat sink as discussed by Maurice et al [2]. to absorb the large heat flux from the engine and flight vehicle skin by the endothermic reaction of the fuel. Endothermic fueling is beneficial because it acts almost as a pre-burner for the fuel. Extensive research has been done to find the right endothermic fuel for hypersonic aircraft to reduce the excessive heat using storable fuel without sacrificing flight efficiency. Figure 2 shows the cooling capacity of various endothermic fuels.

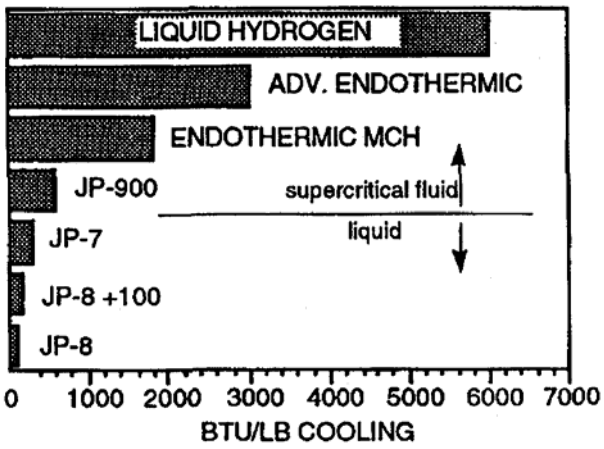

Figure 2. Different cooling capacities of various fuels [1].

According to Figure 2, the liquid hydrogen has significant cooling capacity over the JP-type hydrocarbon fuels. However, the hydrogen has a drawback. Hydrogen has to be stored cryogenically or in heavy pressurized tanks which require additional design considerations. Hydrogen is also a highly reactive gas to work with. Thus, liquid hydrogen fuel may only be suitable for agencies such as NASA, which have an appropriate infrastructure for using hydrogen fuel.

Hydrocarbon fuels have been used for over a century. They are liquid at room temperature and are not as volatile as hydrogen which makes their handling easier. Hydrocarbon fuel is used everyday in numerous applications in various operating environments. Thus, JP-type hydrocarbon fuels can also be used in supersonic combustion applications. The United States Air Force (USAF) has been evaluating the use of the conventional hydrocarbon fuel as a coolant for use in future aircraft to absorb the heat. Therefore, a large amount of heat load has to be managed with the on-board endothermic fuel such as JP-type hydrocarbon fuel to increase thrust-to-weight ratio and aircraft speed [1].

Problem Statement

The faster the flight speed and the longer the flight time, the more likely it is the fuel condition will be well above the thermodynamic critical point, absorbing large amounts of heat. Since hydrocarbon fuel that is currently used in both scramjet and gas turbines engines can exceed its practical temperature limit, it may be thermally cracked into simpler components before it is injected into the combustion chamber.

After thermal cracking, the fuel consists of small gaseous hydrocarbons (C1-C4) and large hydrocarbons (-C10), such as ethylene, methane and ethane [3]. Therefore, the fuel becomes a multi-component mixture at a supercritical condition which has different chemical and physical properties. These physical properties can consist of a liquid like density, zero latent heat, zero surface tension, high compressibility, large specific heats and speeds of sound, as well as enhanced values of thermal conductivity, viscosity, and

mass diffusivity [1]. Thus, it is expected for supercritical fuel to have a different behavior from that of liquid fuel when it is injected into the combustor.

Consequently, unique thermodynamic and transport properties of supercritical fluids along with phase transition phenomena during the fuel injection process can significantly change combustion characteristics inside a scramjet combustor. Plume properties of supercritical jets are of great interests to this study of fuel/air mixing and subsequent combustion.

Research objectives

- Determine species distribution profile in terms of mole fraction downstream of a supercritical methane/ethylene mixture jet using spontaneous Raman scattering.
- Determine whether the condensation process within the jet affects the fuel dispersion rate into the air.
- Determine whether the far-field species distribution still preserves the same concentration ratio, compared to that of fuel mixing ratio.
- Determine which nozzle design performs better than others based on the distribution profile.

Research focus

Previous research by Lin et al. [4] for the study of methane/ethylene mixture is to see whether this mixture will act the same as pure ethylene in terms of global visualization, but it did not look into the detailed species distribution within the fuel

plume. The use of the Raman scattering technique to study the far-field distribution profile of pure ethylene jet was done by Wu et al. [5].

The main research focus of this work is to measure the species distribution profiles in terms of mole fraction of supercritical methane/ethylene mixture injection down-stream of the jet using the Raman scattering technique in order to clarify whether there is any preferential condensation within the condensed jets. In other words, it will show whether the down-stream species distribution still has the same concentration level. For example, a supercritical methane/ethylene mixture with a methane concentration of 10% is injected from the injector, maintaining temperature and pressure of the injection fuel to be in condensed phase, determine whether the methane concentration can still be maintained at 10 % relatively at that down-stream location. Is it possible the methane still in the condensed phase will or will not diffuse or be convected like gaseous methane 10% level be maintained throughout the entire fuel plume?

Methodology

First, shadowgraph imaging technique is used in order to visualize the global jet appearance and determine the injection temperature condition of where the condensed jet is produced. Then, Raman scattering measurement is employed to study the species distribution profiles at that down-stream location. A supercritical methane/ethylene mixture with a methane concentration of 10% and 20% is injected into a nitrogen gas chamber at room temperature. The injection temperature and pressure are maintained at such a condition that the injected jet exhibited the condensation phenomenon. This is done with four different nozzle configurations.

II. Literature Review

Chapter Overview

The following chapter contains a discussion of the previous fundamental research covering the injection of a supercritical mixture of methane and ethylene into quiescent environment. In addition, theoretical approaches of Raman spectroscopy as well as the shadowgraph imaging technique are introduced. Previous research provides valuable insight into near field jet structure and its phase transition conditions. In essence these transitions are described by the condensation and jet expansion angle as a function of injection temperature and pressure.

Raman spectroscopy is a useful technique for molecular identification using light scattering characteristics. The technique is a linear, inelastic, two photon phenomena employing the laser as a monochromatic light source and the spectrometer to examine light scattered by the molecular species. Shadowgraph is a well known visualization technique using the deflection angle characteristic of light that relates different density medium to specific deflection angles.

Relevant Research

Many research efforts have progressed both experimentally and numerically to characterize the near-field jet structure of the supercritical methane/ethylene mixture injected vertically downward into a sub-critical nitrogen filled chamber at room temperature. The supercritical methane/ethylene fuel mixtures with methane mole fractions of 0.1 and 0.9 along with different nozzle orifice diameters are primarily used to

investigate temperature and pressure effects on the jet condensation phenomena using the shadowgraph imaging technique. Downstream of the plume, the Raman scattering technique is used to explore mixing characteristics of pure ethylene jet by Wu et al. [5].

Supercritical Region.

At the triple point, three different phases co-exists, and as the temperature and pressure keeps increasing above the triple point, the liquid will become less dense due to the thermal expansion while the gas will become denser due to the increasing pressure. Eventually, the densities of the liquid and gas will converge to what is known as a critical point where the liquid and gas boundary disappear.

Once the substances are above the critical point, they are said to be supercritical and exhibit thermodynamic properties of both a liquid and gas. For example, a supercritical substance could have gas like diffusivity and viscosity while displaying a liquid like density [6]. The critical pressure and temperature of ethylene are 5.04Mpa and 282K as can be seen in Table 1. Those values could be acquired using the SUPERTRAPP program which is a product of National Institute of Standards and Technology (NIST) [7]. SUPERTRAPP is an interactive computer database designed to predict the thermodynamic and transport properties of fluid mixtures. For this research, SUPERTRAPP is used to develop the required critical temperature and pressure for pure ethylene and mixtures of ethylene/methane with methane mole fractions of 0.1 and 0.2. This data is provided by Air Fore Research Laboratory Propulsion Directorate (AFRL/PR), which is presented in Table 1. The other critical values of different mole fractions are also presented in Figure 3 for a quick reference.

Table 1. Critical temperature and pressure point according to the ethylene and methane mixture ratio.

X_{CH4}	P_c (MPa)	T_c (K)
0.0	5.04	282.4
0.1	5.34	276.5
0.2	5.64	270.0
1.0	4.60	190.4

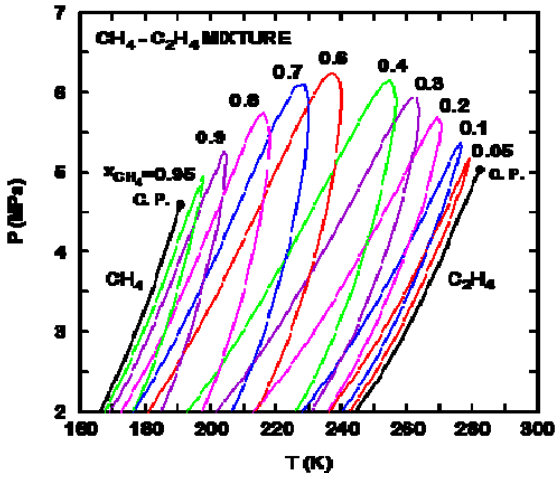

Figure 3. Critical temperature and pressure diagram of different methane/ethylene mixture fuel from SUPERTRAPP Program [7].

Phase Transition.

When the supercritical fuel is injected into a low pressure quiescent environment, it will undergo phase transition during the isentropic expansion process (i.e., there is no entropy change during the injection process). According to the entropy-pressure phase diagram shown in Figure 4, the supercritical fuel near the critical point around T_{inj}/T_c = 1.03 can be forced into the two-phase region (Liquid and Vapor) whereas the higher

temperature, around $T_{inj}/T_c = 1.23$ enters only the vapor region causing the vapor to experience an ideal-gas like expansion path [4].

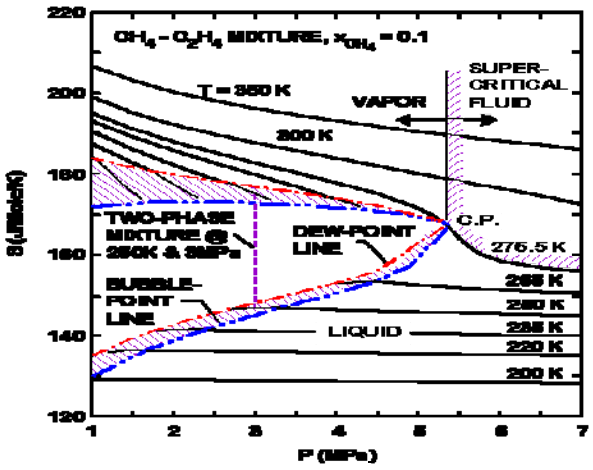

Figure 4. Entropy-pressure phase diagram for the methane/ethylene mixture, $X_{CH4} = 0.1$, from the SUPERTRAPP program [7].

Therefore the phase transition is a strong function of temperature that is expected to occur only near the critical temperature. In addition, the probability of a phase transition occurring is independent of temperature once the temperature exceeds the critical point.

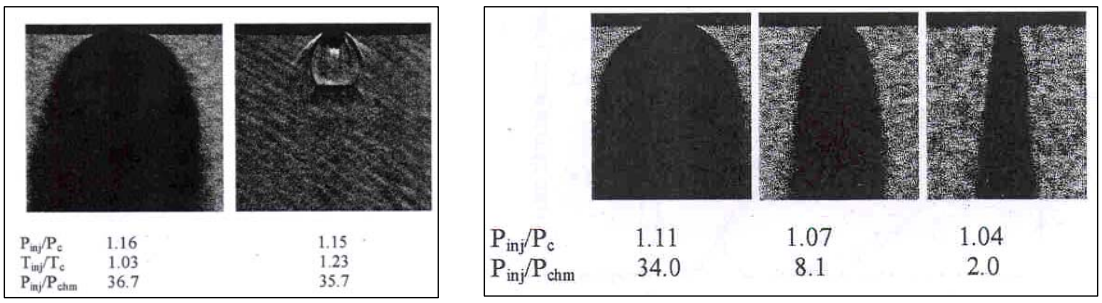

(a) (b)

Figure 5. Condensation phenomena for different temperature ratios at the same pressure ratios (a). Jet expansion angles for different pressure ratios at the same temperatures (b) [4].

Figure 5 (a) is clearly showing the condensation phenomenon is a function of injection temperature rather than injection pressure [4]. This condensation phenomenon can be considered as homogeneous nucleation that is free of foreign objects [4]. In case of homogenous nucleation, the vapor will not be condensed at the saturation point but at supersaturation point. At that time a delayed massive condensed droplets can occur almost spontaneously [4]. The degree of supersaturation is a key factor of determining the nucleation rate and critical droplet radius [8]. It is reported that the nucleation rate increases at the same supersaturation condition with a higher temperature; however, the critical nucleus radius decreases [8]. Therefore, a large number of small droplets can be produced if the injection temperature of a supercritical fluid approaches the critical temperature [8]. Also, it is observed that the starting point of condensation moves towards the inside of the nozzle as injection temperature ratio (T_{inj}/T_c) approaches unity and moves toward the nozzle exit as the injection temperature ratio moves away from unity.

Characteristics of the Near-Field Jet.

The location and size of the Mach disk is determined by measuring the distance between the center of the Mach disk and the injector orifice as well as the distance between the two triple points. Moreover the shock expansion angle is measured as the angle between the jet centerline and the line tangent to the jet boundary passing through the edge of the orifice.

An ethylene and nitrogen are used to measure the axial distance from the injector exit to the Mach disk. The result shows that it increases as the ratio of injection pressure to chamber pressure increases [9]. Additionally, it is reported that the axial location of the

Mach disk relies only on the pressure ratio and is independent of fuel types and fuel condensation [5].

The diameters of Mach disks for the supercritical ethylene and nitrogen jets are measured and the Mach disk size increases as the ratio of the injection pressure to the chamber pressure increases. However at the lower injection temperature (lower than 325K) the Mach disk size increases as the injection temperature approached the critical temperature, possibly due to the effects of larger fuel mass and condensation [5].

The shock expansion angle demonstrats the same behavior, as shown in Figure 5 (b), The expansion angle increases as the pressure ratio increases and also, at a lower injection temperatures (lower than 311K) the angle is substantially increased as injection temperature decreases approaching critical temperature.

It is observed that the condensation is less significant and that fuel penetration length shortens as the ambient temperature increases on the near-field while maintaining the constant injection temperature [5].

Mixing Characteristics at the Downstream of the Ethylene Jet.

Far-field expansion and mixing characteristics of supercritical ethylene injected into superheated nitrogen environment are studied using Raman spectroscopy [5]. The number density of ethylene and nitrogen are measured at z/d = 112 (1mm nozzle diameter), P_{inj} = 5.8MPa, varying injection temperatures from 293-358K with P_{chm} = 0.2MPa, and a constant chamber temperature of 300K. It is reported that the maximum ethylene number density value is at the jet center and decreases as the radial distance increases whereas the nitrogen number density shows a deficiency at the jet center due to the presence of the ethylene jet [5]. The total gas number density of nitrogen and ethylene

peaks at the jet center when T_{inj} = 293K and become constant value as the injection temperature increases to 358K due to the decrease in the ethylene number density. In addition, the mole fraction is calculated based on the number density of each gas and this value decreases as the injection temperature increases, but there is no significant variation between 325K and 358K [5]. With the assumption of the uniform pressure distribution at the measurement station, the temperature distribution of the jet plume exhibits that the temperature at the center of the jet plum is lower than that of the outside because of the presence of fuel condensation and near-field expansion [5].

Jet Flow

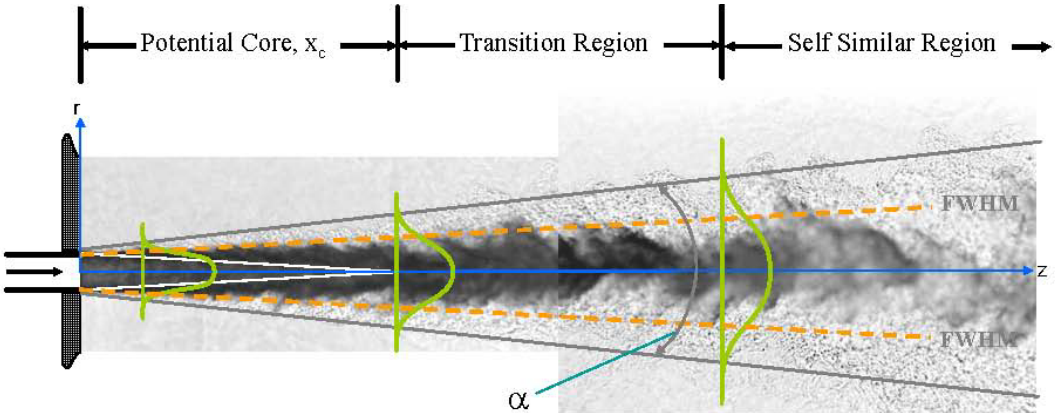

Figure 6. Nitrogen injection shadowgraph image for jet flow structure [10].

Figure 6 is a shadowgraph image of nitrogen injection at supercritical pressure done by Branam et al. [10]. The figure is overlaid with some of the characteristics for free jet flow such as velocity, divergence angle as well as jet width of full width half maximum (FWHM). This image is showing the turbulent jet structure of three distinctive zone: potential core, transition region, and a self-similar region. Usually the jet is categorized as either laminar (R_e < 2000) or turbulent (R_e > 3000) with a transition region

between the two flow regimes [10]. The jet regime of this research is well in the turbulent regime based on the calculation of Reynolds number ($R_e = 7.2 \times 10^5$).

The potential core length is the closest region to the injection plane containing most injected mass and it is calculated using the density ratio provided by Chehroudi et al. [11] shown the relation below:

$$\frac{z}{d} = C\left(\frac{\rho_0}{\rho_\infty}\right)^{\frac{1}{2}} \qquad 3.3 < C < 11 \tag{1}$$

where ρ_0 , ρ_∞ are centerline density and ambient density respectively. This representation is based on the empirical data and derived from the intact core of liquid sprays. However, the potential core computation is done for all the Raman scattering injection conditions to compare the condensed phase jet core length to gaseous phase jet of increased injection temperature. The 3.4 is selected as a proportional constant in this research.

As the jet moves away further downstream of the potential core, the jet continues to transit to a fully mixed condition [10]. The injected mass is more spread out to the surrounding environment in the radial direction. Far downstream, the jet finally becomes self similar where the radial profiles of density and bulk velocity can be described as a function of only one variable [10]. Schetz reported that this behavior is observed at about $z/d \geq 40$ [12].

Raman Spectroscopy

Nature of Raman Scattering.

Light is a stream of photon particles. When incident light interacts with matter, some of the particles may be scattered out with different wavelength than that of the

incoming incident light photon particles. Raman spectroscopy has been used for molecular identification by light scattering characteristics less than 1 μm of molecular size, since it was first observed in 1928 by C.V. Raman [13].

As can be seen in Figure 7, if light is directed to a molecule the vast majority of the photons simply bounce off the molecule without energy exchanging that is elastically scattered with nearly the same frequency or wavelength to the incident photons. This phenomenon is referred to as Rayleigh scattering. However, a very small fraction of incident photons, approximately 1×10^{-7}, is scattered in an inelastical fashion (i.e., exchanging energy between the photon and the molecule). In this case, a scattered photon has a different frequency than the incident photon. This shifted frequency or energy difference between incident and scattered photon is equivalent to the vibrational energy taken from the molecule, thus it can provide molecular chemical and structural information [14].

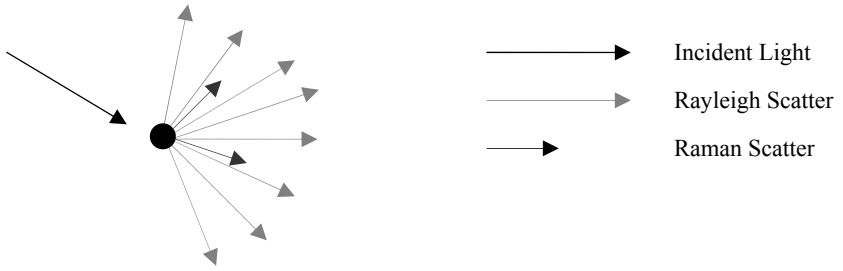

Figure 7. A simple sketch of light scattering presented when incident light interacts with the sample. Rayleigh scattering occurs with the same wavelength as the incident light and Raman scattering occurs when new particle wavelengths are scattered out.

Electromagnetic Wave.

It is important to understand the radiation characteristics of a laser as an excitation source for Raman Spectroscopy. As briefly mentioned earlier, a Raman signal is very weak and its intensity is linear with the intensity of a incident light source. Thus, it

requires a strong light source such as a laser. The basic concept of laser radiation will be discussed briefly, since a comprehensive discussion of every available laser is beyond the scope of this research.

Advantages of employing a laser as an excitation source include the fact that the laser is a linearly polarized beam, which can provide optimal incident power to obtain a suitable Raman signal. It can be easily focused employing simple optical geometry set up focused with small diameters in the range of 1-2 mm [15]. Its radiation properties can be characterized by monocromaticity, directionality, and coherence, which can be described as a sum of sine waves as a function of time. Laser radiation is composed of waves at the same wavelength, which start at the same time and maintain their relative phase as they advance. As shown in Figure 8, laser wave is composed of electric and magnetic fields which are perpendicular to each other. The direction of the propagation of the wave is at right angles to both field directions: this is known as an electromagnetic wave which carries energy as it propagates forward.

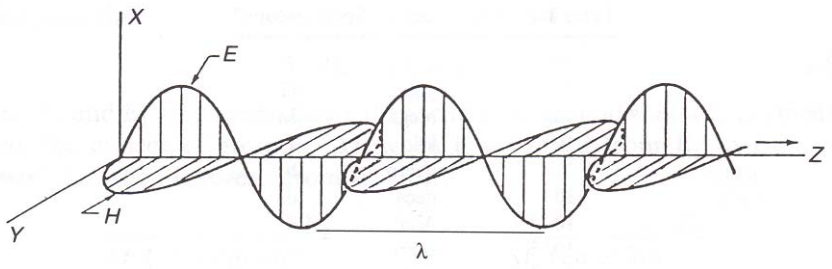

Figure 8. Electromagnetic radiation [16].

Classical Theory Overview.

The principle of Raman scattering can be described according to the classical point of view, depicted in Figure 9. Consider a wave of polarized electromagnetic radiation propagating in the *z*-direction. This wave consists of two components; electric

(*x*-direction) and magnetic (*y*-direction) components that are perpendicular to each other. The research presented in this thesis does not include magnetic phenomena.

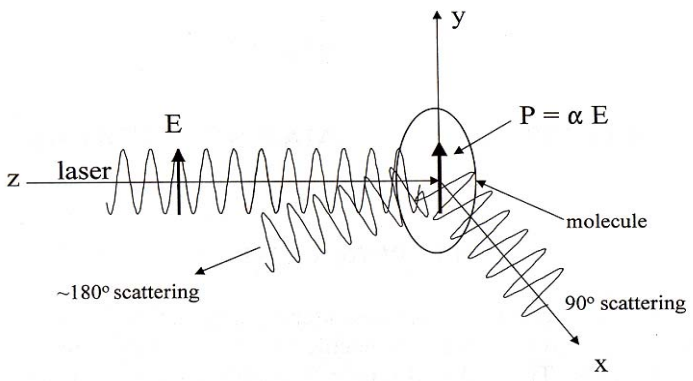

Figure 9. Polarization (*P*) induced in a molecule's electron cloud by an incident optical electric field *E* [17].

According to Gauss's Law for electric fields, the polarization P, is induced when the molecule originates from the oscillating electric field of incident light. This forms equal but opposite charges in an electron cloud, which is termed an electric dipole moment for its strength. This induced dipole scatters the light, with or without exchanging energy by vibrations in the molecule, as mentioned earlier. The relations between the strength of the induced polarization, and the incident electric field, E, is described by the equation below:

$$P = \alpha E \tag{2}$$

where α is defined as polarizability. The strength of the oscillating electric field, E, is shown as the equation below:

$$E = E_0 \cos(2\pi\nu_0 t) \tag{3}$$

where E_0 is the vibrational amplitude and ν_0 is the incident photon frequency of the laser (16). Combing with equation 1 and 2:

$$P = \alpha E_0 \cos(2\pi \nu_0 t) \tag{4}$$

The polarizability can be expanded as the summation of a static term, α_0 as shown in the equation below:

$$\alpha = \alpha_0 + \left(\frac{\partial \alpha}{\partial q} \right)_0 q + \cdots \tag{5}$$

where *q* pertains to the normal modes of molecular vibrations such as 3N-6 (or 3N-5 for a linear molecule) in *N* atoms of a molecule [17]:

$$q = q_0 \cos 2\pi \nu_m t \tag{6}$$

where ν_m is the characteristic harmonic frequency of the molecule's m^{th} normal mode. Therefore, combining equation 4 with equations 5, 6 and using trigonometric identities to obtain the electric dipole moment split gives [15, 16, 17]:

$$P = \alpha_0 E_0 \cos(2\pi \nu_0 t) + \frac{1}{2}\left(\frac{\partial \alpha}{\partial q} \right)_0 q_0 E_0 \left[\cos\{2\pi(\nu_0 + \nu_m)t\} + \cos\{2\pi(\nu_0 - \nu_m)t\} \right] \tag{7}$$

The induced polarizability defined above radiates light at the frequency of their oscillations [17]. If the rate of change of polarizability, $\left(\frac{\partial \alpha}{\partial q} \right)$, along with the vibration cannot be zero to yield the Raman scattering [16], the first term, oscillating dipole, is Rayleigh scattering which is at the same frequency, ν_0, and has a magnitude proportional to α_0, the inherent polarizability of the molecule. The second and third terms represent Raman scattering, which is specific to the vibrational frequency of the molecule: the frequency of Raman scattering is "shifted" from that of the incident laser by the characteristic frequency of a specific molecule [15]. The scattered signal occurs at

$\nu_0 + \nu_m$, which is historically described as the anti-Stokes component while the signal with $\nu_0 - \nu_m$ is considered the Stokes component.

A simplified energy diagram illustrates the processes shown in Figure 10 (a). The incoming photon with initial energy $h\nu_0$ increases the energy of the molecule form the ground state to an excited virtual energy state, which occurs for a very short period of time since this is not a real excited state, such as E_1. Then, the molecule relaxes to a lower state emitting a photon with energy. This emitted photon can have the same energy as an incoming photon, which is the case of Rayleigh scattering.

In the case of Stokes photon, an excited molecule relaxes to a lower state, the vibrational level energy state, giving off a photon with a frequency of $(\nu_0 - \nu_m)$. Stokes radiation allows the initial energy state of the molecules to be in the vibrational ground state for the anti-Stokes case [16]. In the case of anti-Stokes photon, the vibrationally excited ground state is raised to a virtual state by an incoming photon, when eventually decays to the ground state emitting a photon of higher energy at a frequency of $(\nu_0 + \nu_m)$.

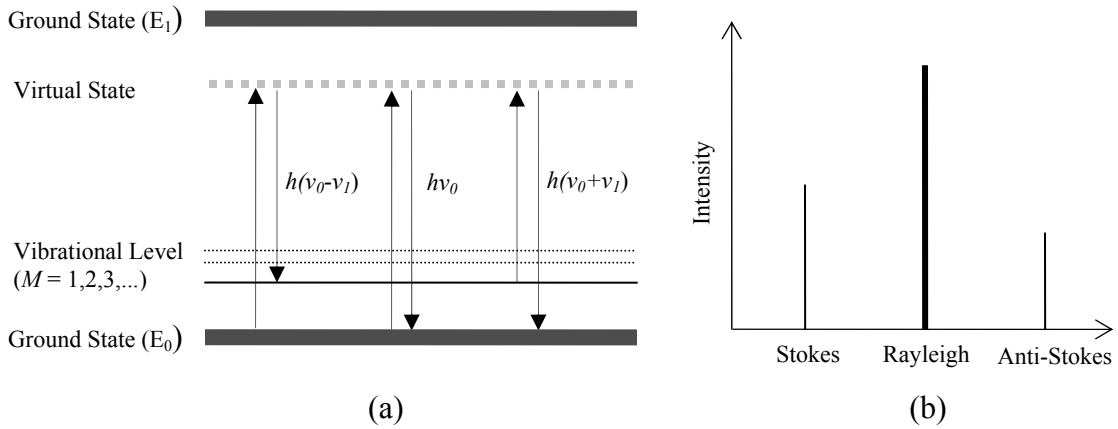

Figure 10. (a) Simplified energy diagrams, (b) Schematic of a Raman spectrum.

In a gas mixture, each species at a given initial energy level will produce a certain degree of Raman signal intensity depending on its species number density, n_i [16]. As can be seen in Figure 10 (b), it is seen that the Stokes and anti-Stokes component are equally spaced from the Rayleigh component suggesting that they contain the same information about the vibrational quantum energy.

The intensity of the Stokes component is much stronger than the anti-Stokes component since the vibrationally excited number of molecules prior to irradiation is much smaller than that of the ground state. Therefore, only the Stokes side of the spectrum is normally measured in Raman spectroscopy. As will be described later, the spectrometer collects this scattered light and separates a Raman signal from other scattered signal in terms of frequency.

The intensities of Raman signal are related to the number density of the gas. Although it is not apparent on equation 7, since $\left(\frac{\partial \alpha}{\partial q}\right)$ is generally much smaller than α_0, the Raman scatting signal is much weaker than the Rayleigh scattering signal and the intensity is proportional to that of the incident light [17]. Hence, a powerful laser source is required to produce adequate Raman scattering signal strength [16].

According to the classical theory, the intensity of a vibrational Raman signal, I_R, can be introduced relating frequencies as shown in equation below [17]:

$$I_R = \phi(\nu_0 \pm \nu_m)^4 \alpha_m^2 q_m^2 \tag{8}$$

The equation above shows that the Raman signal intensity is the fourth power of the observed frequency. In addition, it is proportional to the cross section, σ_m, which is related to $\left(\frac{\partial \alpha}{\partial q}\right)$ with units of centimeters squared per molecule [17]. By the definition for

the cross section, it is the effective area for the collision region. The Raman cross- section is an empirically determined value [15]. Q-branch cross sections for molecules of interests are tabulated in Table 1. The values are determined under room temperature with a 532 nm frequency doubled Nd:YAG laser [18].

Table 2. Raman cross sections for molecules of interest in combustion [18].

Species	Vibrational frequency (cm^{-1})	Cross Section (532 nm) $10^{-30}cm^2/sr$
N_2	2330.7	0.46
O_2	1556	0.65
H_2O	3657	0.9
CH_4 v_1	2915	2.6
v_3	3017	1.7
C_2H_4 v_1	3020	1.9
v_2	1623	0.76

Thus, the intensity of a Raman signal can be described relating the cross section, σ_m, with the laser intensity, I_0, in Watts [17] :

$$I_R = I_0 \sigma_m n_i dz \tag{9}$$

where n_i is the number density of each species with units of molecules per cubic centimeter and the dz is the path length of the laser in the sample. Since all modern spectrometer are designed to measure photons rather than power in Watts the above expression should be replaced with the photon counting system as shown:

$$P_R = P_0 \eta n_i dz \tag{10}$$

where $\eta = \frac{d\sigma_m}{d\Omega}$ is a differential of the Raman cross section, Ω represents the solid angle of collection with units of centimeter squared per molecule per steradians, and σ_m is the integrated cross-section with respect to all scattering directions from the sample molecule. P_0 and P_R are Raman signal intensities generated by a laser beam with a $1cm^2$ cross section and a path length of *dz*. It is important to note that the Raman signal intensity is a function of the physical parameter of the sample (η, n_i) and the laser (P_0) instead of depending on the collection parameter such as the collection angle or quantum efficiency.

After an incident laser beam interacts with a sample, all of the scattered signals are emitted with different wave lengths and intensities entering a spectrometer, an optical instrument that allows images to form from an incident signal according to its wavelengths [16]. As mentioned earlier the Raman scattering signal is very weak and can be easily obscured by elastic scattering from solid samples, optics, and dusts [17]. Thus, it is necessary to separate a Raman signal from other radiation sources at the various wavelengths and intensity levels. Laser rejection filters such as dielectric, holographic, and absorption notch filters are the most commonly used for single spectrograph of Raman spectroscopy [17]. Therefore, all other interfering lights such as stray light, Rayleigh and Mie scattering are rejected and only Raman scattering signals can enter the spectrograph. The signal can be split or dispersed into a spectrum by either using a prism or diffraction grating. This effect is based on the different wavelengths or energies of light.

In general, gratings are more efficient and provide a better linear dispersion of wavelengths without absorption effects, when compared to a prism. Thus almost all

spontaneous Raman spectrometers employ diffraction gratings [17]. A zoomed-in illustration of a diffraction grating is shown below in Figure 11.

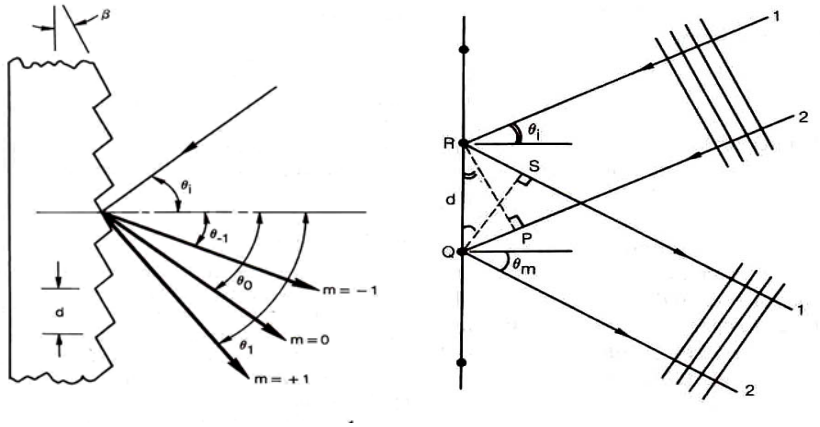

Figure 11. Illustration of the behavior of a reflection phase grating [15].

A diffraction grating consists of equally spaced small parallel grooves that disperse polychromatic light into its constituent wavelengths. The incident light entering the spectrometer is reflected and dispersed onto the grating coated in a very thin reflective layer and each wavelength is detected to the detection system at a focal plane.

The dispersion relation between the incident and the reflected light from the diffraction grating, with groove spacing (d) is given below [15]:

$$\mathrm{d}(\sin\theta_m - \sin\theta_i) = m\lambda \tag{11}$$

where θ_i is the angle between the incident light and the surface normal of the grating plane, and *m* is the diffraction order which depends on the grating design. The dispersion and the efficiency of a grating system rely on the groove spacing and it's angle, β. Usually, the grating is designed to be efficient at orders of 15°-30° of the groove angle [15]. Hence according to the above equation, radiation will be reflected from the grating at an angle dependent upon its wavelength for the Raman scattering application, this

wavelength is the Stokes component. Figure 12 is briefly showing the internal structure of the spectrometer.

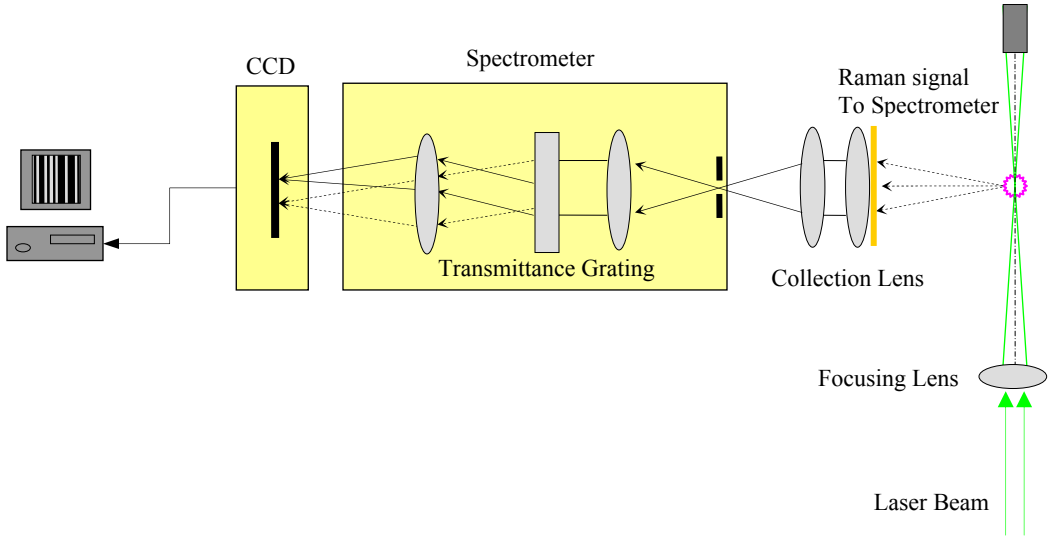

Figure 12. Schematic of spectrometer system.

Low-noise is always a number one consideration for a detection system, since noise degrades the weak Raman scattering signal [17]. Several detection systems have been developed and commonly used such as photon counting, photodiode array detection and a CCD basis detection system.

The CCD has been increasingly used for its advantages such as high quantum efficiency and low readout noise, the sensitivity over the wide range of wavelengths (120-1000nm) [16]. The CCD is a silicon-metal-oxide semiconductor based optical-array detector, forming a two-dimensional matrix of photo sensors (pixels). The pixel size ranges from 6-30μm. A typical 1024×256 two-dimensional CCD detector is depicted in Figure 13.

The principle of operation is that a certain amount of an incident signal generates photoelectrons in the silicon. The potential well formed by a circuit pattern deposited on

the silicon surface attracts photoelectrons and store approximately 10^4-10^6 photons before reaching full capacity. These potential wells form an array across a two-dimensional silicon panel, with each column of potential wells corresponding to a different wavelength [17]. Each of large number, narrow pixels of different wavelength represents corresponding Raman shifts. After this integration period, each group of stored electrons is amplified and converted to a digital value, by an analog to digital converter (AD). Finally, the resulting value is constructed as a plot of the number of electron counts versus Raman shifts, as illustrated in Figure 14 using two different sample species.

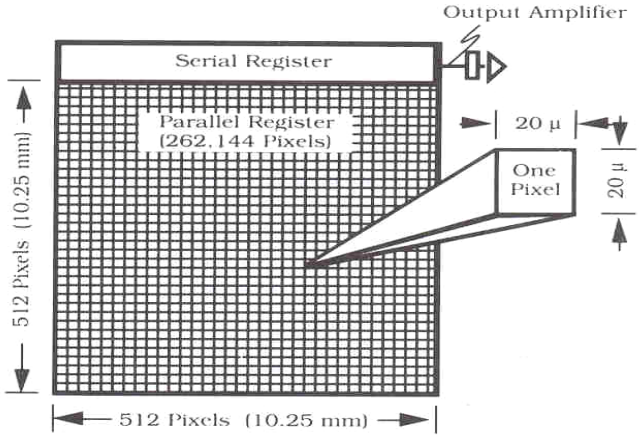

Figure 13. Schematic of a CCD Detector for 512×512 pixel array [16].

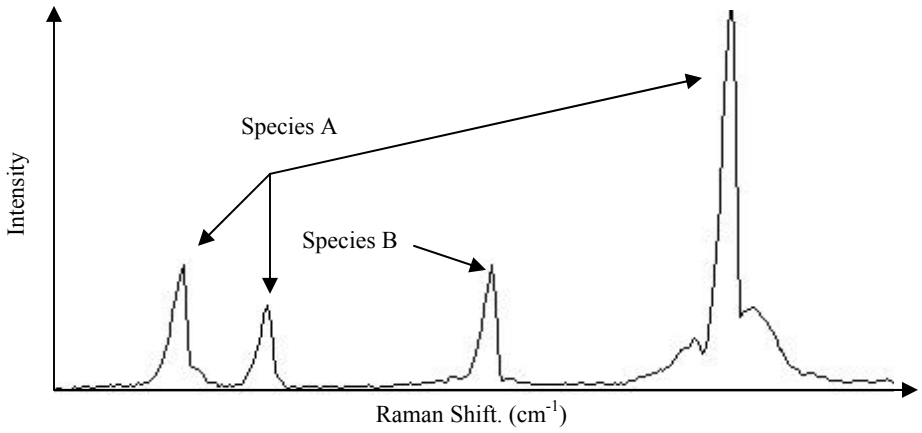

Figure 14. Example of Raman shift of bi-species medium.

Shadowgraph Imaging System

The shadowgraph imaging technique has been used for visualizing non homogeneities in transparent media with simple optical arrangement without disturbing the test section. This imaging method is based on the principle that the refractive index of light changes in accordance with density. The ratio of the speed of light in a medium to the speed of light in a vacuum is the index of refraction [19]. A ray of light is bent toward regions of a higher refractive index. Figure 15 displays a two-dimensional flow in the *x*-direction with a density gradient in the *y*-direction.

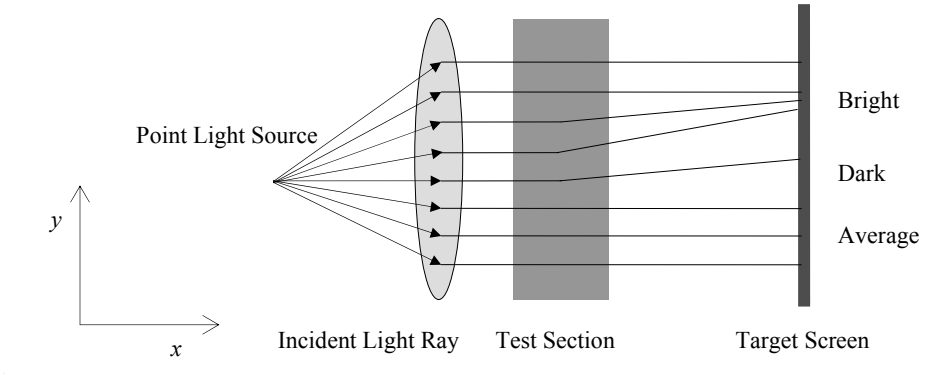

Figure 15. Schematic of the shadowgraph technique for 2-D transparent flow.

Consider a ray of light from a light source propagating in the positive *x*- direction. This ray can be collimated by a lens then, the light passes through a transparent test section with a density gradient. The parallel light ray is deflected from its incident path angle due to a different index of refraction based on the density gradient [19]. After the light passes through the test section, the deflected ray is imaged on the screen which is placed other than the focal plane and then focused or defocused according to the index of refraction of the test section. On the screen, the bright region corresponds to where the ray of light is focused or converged and dark region corresponds to where the ray of light

is defocused or diverged. If the test section has a uniform density gradient, all of the incoming light is deflected at the incident angle and would produce a uniform image on the screen. Thus, the combination of the bright and dark regions on the screen generates a precise image of the density gradient of the flow field.

The shock wave can be seen on the screen as a dark region with a light region. The net effect of a shadowgraph depends on the second derivative of density hence, it is an appropriate imaging instrument for flows with large, sudden density changes (strong shock waves) [19]. A CCD camera captures the image, which is then saved on a computer.

III. Methodology

Chapter Overview

In order to accomplish this research goal, the region of supercritical condition has to be determined in terms of temperature and pressure based on the results of the SUPERTRAPP data program. Then, the supercritical fuel near the critical point is injected into the chamber vertically varying the injection temperature each time to find the condition where the condensation occurs. The shadowgraph imaging technique is employed with each temperature change. Once the condensation condition and global jet structure are visualized, the 532nm continuous wave Nd:YVO4 laser is applied to the down-stream location where is the self similar region and the jet plume starts becoming a fully developed turbulent jet. Then, the scattered signal is collected by the spectrometer placed at 90 degrees to the beam path. Then, the Raman signal is isolated and captured by a CCD camera at the focal plane. The number density of each species can be determined by the correlation constants which gives information about the species distribution profile.

This chapter starts by describing the research apparatus and instrumentation which is fundamentally same as Wu et al. [5]. However, the chamber pressure transmitter is replaced by a new one which gives more accurate pressure readings for determining number density. It is followed by three different calibrations which are critical steps for the success of Raman spectroscopy. Then, test strategy and experimental procedure are introduced. It is followed by the data processing method of both shadowgraph and Raman spectroscopy.

Apparatus

The supercritical methane/ethylene mixture gas is injected vertically downward through the nozzle into a quiescent environment filled with nitrogen gas at room temperature and constant pressure. The basic schematic of the apparatus, as shown on Figure 16, consists of five major components: the fuel supply bottles, the accumulator which mixes the fuel at a constant pressure, the chiller which controls the injection temperature, the injection nozzles, and the chamber units.

Commercially available AL size fuel cylinders ($0.0295m^3$ internal volume) are used to supply nitrogen, methane, and ethylene gases with initial pressures of 15.2MPa, 8.3MPa, 13.8MPa, respectively. The nitrogen gas used for back pressure is industrial grade 99.95% pure gas and the methane/ethylene gases are 99.99% chemically pure grade. The appropriate gas regulator is placed on the outlet of each gas cylinders and is connected to one side of accumulator (designed maximum working pressure is 20.7MPa) through the pressurized flexible gas line (designed working pressure is up to 0.7MPa). Once the methane/ethylene gas is charged, the fuel gas inlet valve is closed and the nitrogen gas is charged on the other side of accumulator until the desired supply pressure is reached. The supply pressure is controlled by the nitrogen regulator. The fuel is manually mixed and a detailed description will be introduced in the experimental procedure section. Four different bridge-type pressure transmitters are used for measuring the static pressure of the fuel supply, the nitrogen back pressure of accumulator, and the fuel injection pressure having an accuracy of ± 7 KPa. Since the fluid velocity of fuel delivery line is negligible, the measured static pressure is used for stagnation pressure. Also, the thermocouple is placed at the same location with pressure transmitter

monitoring the fuel supply, injection, chamber temperature. These flow properties are saved on the control laptop computer as a data log file automatically initiated by the fuel injection isolation valve (IV).

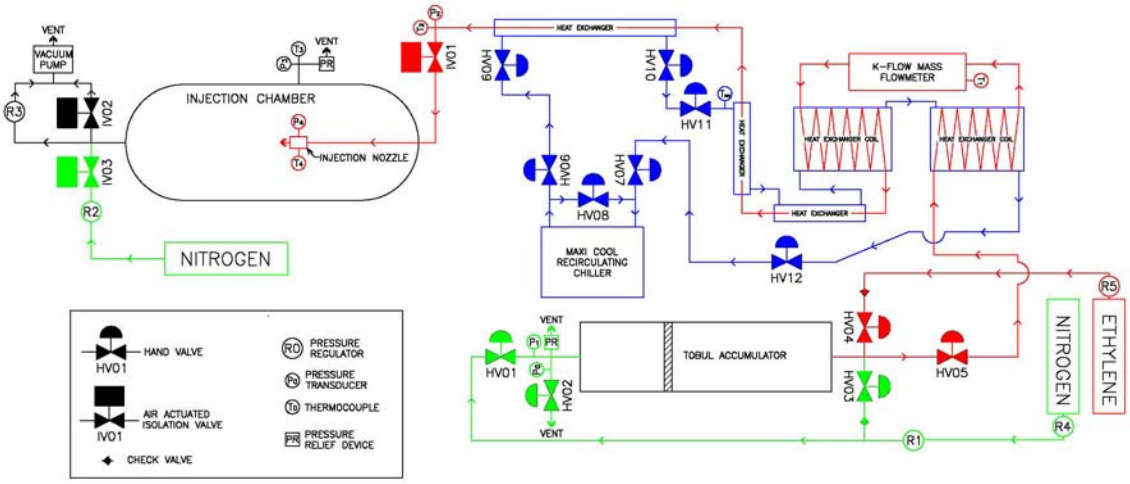

Figure 16. Sketches of Supercritical fuel injection apparatus.

It is important for current research to accurately control the injection temperature since the condensation process is highly dependent on the injection temperature near the critical point. Thus, thermocouples measured the supercritical fuel injection temperatures at the nozzle holder and the injection temperature was controlled by Maxi-Cool™ Re-circulating Chiller circulating ethylene glycol as the main coolant. The ethylene glycol flows through the double layered fuel passage pipe in the opposite direction of the fuel flow. The chiller is remotely operated by the main control laptop computer temperature set point. The total length of fuel passage pipe is approximately 5m. The first one third of this is insulated. It is expected that the heat transfer between the ambient air and coolant is much greater than that of fuel. Therefore, there is some inaccuracy between the chiller set point, the fuel supply temperature, and the injection temperature; although the chiller provides very good temperature control in the range of 270K to 300K with ±1K accuracy.

However, it is reported that the temperature difference between the final fuel temperature and the coolant temperature was within 2K.

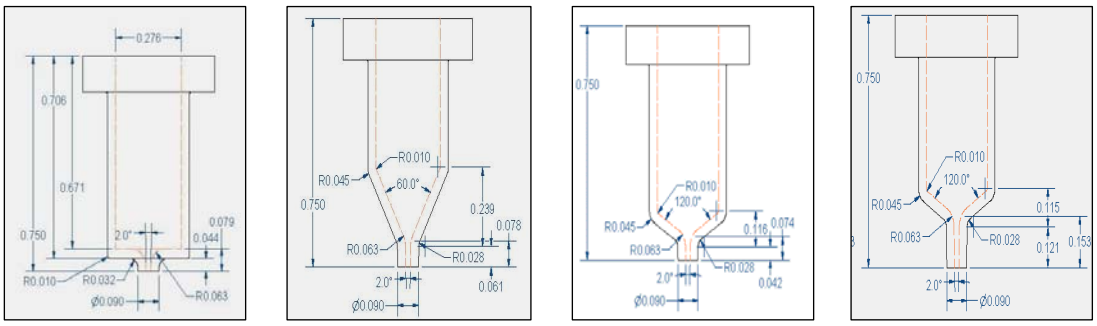

(1) (6) (7) (9)

Figure 17. Sketch of the nozzles used for this study, d = 0.5mm.
(See Appendix A for more information)

The injection nozzles are attached to the end of nozzle holder. The nozzle holder's length is designed to be adjustable by inserting spacers, thus both the far and near field of the jet can be seen through the chamber viewing port. Four round nozzles are used to examine the effects of nozzle internal configurations on the condensation process as well as species distribution. The detailed internal nozzle geometry description is shown in Figure 17 having the same orifice diameters, 0.5mm. Each nozzle has the same entry radius of 0.7mm but different convergence angle and final passage length. Nozzles #7 and #9 have different final flow path length. The final flow passage of every nozzle is designed to have a 1-degree convergence to the nozzle exit to make sure a flow choke point could occur only at the nozzle exit.

The fuel is injected and mixed with air molecules flowing at subsonic (ramjet) or supersonic (scramjet) speeds. The chamber for this research is designed to simulate the temperature and pressure profiles encountered in ramjet and scramjet engines [5]. The chamber is mounted vertically and leveled on the supporting structure, then connected to

a heavy laser table for stability. This structure minimizes vibrational disturbances which could be generated at the moment when highly pressurized fuel is injected to the low pressure chamber. The chamber diameter is 0.31m and its height is 0.91m, resulting in an internal volume of 0.067m^3. It has two 6.35cm diameter optical windows placed 180° apart 1/3 of the chamber length from the top for optical test measurements allowing the laser beam to pass through. Another 10cm viewing port is placed at the same height at a right angle to the two optical windows allowing the Raman signal to pass to the spectrometer. Also, the chamber viewing port is 25.4cm above the laser table to make sure that it has the same height as the spectrometer camera lens detecting the signal. During the Raman spectroscopy, the exit window of two optical windows is replaced by laser beam trap for safety purposes minimizing laser beam scattering and absorbing most the beam energy; thus, minimizing backscattering. A relief valve is set at 0.7MPa for safety purposes since this chamber is designed to have 0.7MPa as a maximum working pressure at a room temperature. Chamber pressure is monitored by Omegadyne PX5500L1-100AI pressure transducer installed at the bottom of the chamber having an uncertainty of ±0.1%, and can be used up to 0.7MPa. The chamber pressure regulator is installed to minimize pressure rise during the injection time for constant pressure conditions. The facility vacuum pump is connected to the bottom of the chamber to vent the injected fuel out of building.

Instrumentation

Raman Scattering System.

A simple schematic of the instrumentation setup for the Raman spectroscopy is shown in Figure 18. A Spectra-Physics Millenia Pro, continuous wave (CW), Nd:YVO4 laser is used as the light source producing 10 Watts at 532 nm frequency. This diode pumped solid state laser (DPSSL) generates the vertical polarization with 2.3mm±10% beam width. The beam is turned 90 degrees twice by two different mirrors mounted on each side of the laser rail arm and focused after passing through a 1-meter focusing lens placed between the two mirrors. The beam then, enters the chamber optical window and focuses at the center of the chamber perpendicular to the direction of jet injection allowing for one-dimensional measurements in the beam path direction.

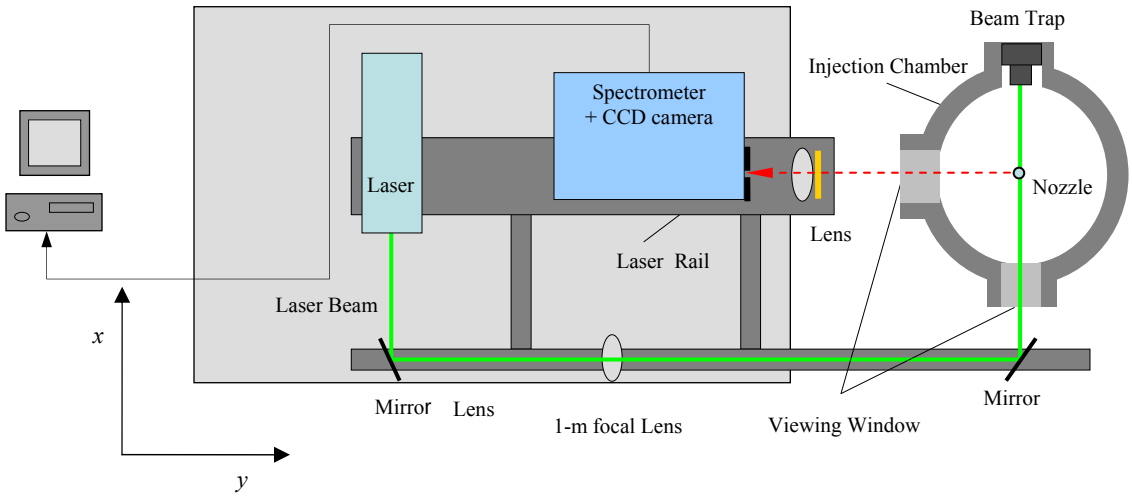

Figure 18. Schematic of Raman spectroscopy instrumentation.

The exit window is replaced by the beam dump to minimize backscattering and reflection that cause signal disruption. The scattered signal is collected by the spectrometer. It is focused by a 58mm, $f/1.2$ Noct Nikon camera lens mounted on the

laser table just outside of 10cm viewing window at right angles to the beam path. The Rayleigh and Mie scattering as well as stray light, is either minimized in intensity or filtered out by the colored, 3mm thick, Schott glass OG570 long path filter before entering the focusing camera lens. The Raman signal passing through the camera lens then focuses on the 1mm width entrance slit. Once again, the Holographic Notch Filter is employed to separate the Q-branch vibrational Raman signal component. The 3600 grooves/mm Holographic transmittance grating is selected to obtain the signal spectrum throughout this research. Its wavelength range selection is only for nitrogen, methane, and ethylene wavenumbers, (Table 2).

Each wavelength is captured by Andor's iXon^{TM}+, back-illuminated with 512×512 pixel array (24×24 μm each pixel size), Electron Multiplying Charge-Coupled Device or EMCCD detector at the focal plane. Several different binning factors are available to perform the statistical analysis. The vertical 2×2 binning factor (total 4 pixels) is selected for all images captured in the present research. This is because only the variation in concentration along the laser-beam axis is of interest. Since the camera field of view is set to view 4.2mm, the corresponding length of space viewed by each pixel is 0.016mm along the beam axis.

The Andor software controls the CCD camera and saves captured images to the computer as a Tagged Image File Format (TIFF or TIF) file. The camera shutter is precisely controlled by an external trigger, Stanford Research Systems DG535 digital delay generator, for the signal acquisition with 2 seconds of exposure. For better signal to noise ratio (SNR), the Electron Multiplying (EM) gain is set to 75 at 223K. Ten images are captured and averaged for the calibration and are used to determine the number

density. The entire spectrometer and CCD camera setup is synchronized with the laser table, so the entire set can be traversed in the *y*-direction (Figure 18) to determine the jet centerline where a maximum scattering signal is produced.

Shadowgraph Imaging System.

A direct shadowgraph technique is used to visualize the jet structure and to find the condition where the condensation occurs. Based on that result, the desired down stream location can be determined. The light source is a continuous wave, high pressure mercury arc lamp providing an average brightness of 140,000 candles per square centimeter. As can be seen in Figure 20, the pin hole aperture is placed between two lenses to produce a point light source. The optical lens is accurately placed to collimate the light. The two optical windows are cleaned before being placed on the chamber to take dust free image data.

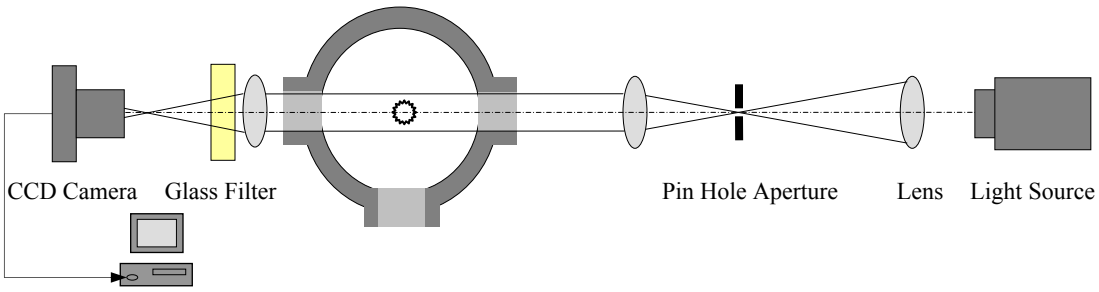

Figure 20. Direct shadowgraph imaging instrumentation.

The 5cm square FGL495S 495nm frequency glass filter is used as a long pass cutoff filter between the camera and the focusing lens to allow semi-monochromatic light to pass through. Then, images from the injection jet are captured by the FASTCAM-X1280 PCI high speed video camera.

On the CCD camera, the sharp density gradient (shock wave of the jet) and condensation can be detected as a dark region whereas the transparent gaseous jet is illuminated as a bright region and the corresponding image is sent to the computer. The camera is controlled by the software installed on the computer. Images taken for the present study are 125 frames per second with a shutter speed of 1/32000 second. The full size, 1280×1024 pixels, and the highest sensitivity, ×8, are selected for the CCD detector. The image file sent to the computer is stored as a TIF, one frame per file.

For this condition, the camera can capture 1024 frames for each record, hence it can provide about 8.2 seconds recording time for each run. Tests show the injection jet mass flow rate becomes steady about 4 seconds after injection begins. The camera can record the entire injection process from the beginning to the end. The nozzle injection diameter is very small, 0.5 mm. The axial distance of the Mach disk from nozzle exit plane and the disk diameter is a few orders of magnitude larger than the injection diameter. The camera is arranged to capture an image with a 7.3×9.1 mm field of view.

Calibration

Before calibrating the laser table and optical instruments, the chamber has to be positioned exactly. The chamber is vertically standing with two optical viewing ports aligned in the same direction as the laser beam path (*x*-direction). The center of the viewing ports has a height of 10cm, the same height as the spectrometer camera. The laser table is moved to level the beam path in the *x*-direction and to ensure the beam is at a right angle with the second mirror.

Three different types of calibrations are involved to measure accurate data of each species condensation profile. A Pen-Ray Neon lamp is used for spectral calibration because it covers a wide spectral range and line positions are well known as shown in Figure 21. A light ray from one side of a double-bore quartz neon tube is focused by the camera lens and enters through a fine entrance slit with width of 0.05mm. The spectral lines spread out along the *x*-axis denoting wavenumber instead of pixel numbers. Care must be taken to locate neon lamp carefully on the laser beam path. Since the wavenumber range of each species of interest (methane, nitrogen, ethylene) is from 5700 to 6400cm^{-1}, the CCD camera is adjusted to cover this wavenumber range on the neon calibration image.

As a result of spectral calibration, the CCD camera is capturing the signal of all three species with different vibrational modes on the same image plane having the nitrogen signal (wavenumber is 6073cm^{-1}) at the center and the other two on the right side of it. Also, the CCD camera has to be positioned right at the focal plane to achieve narrow signal peaks.

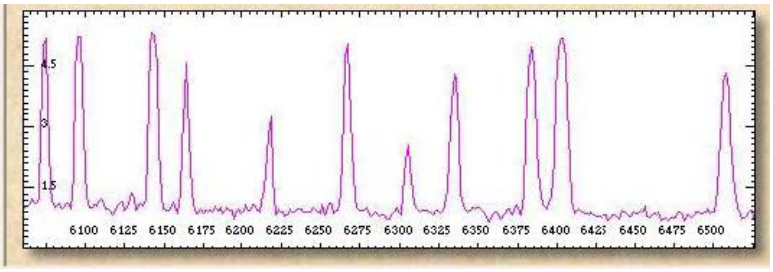

Figure 21. Neon calibration image, number counts on the vertical-axis versus wavenumber on the horizontal-axis [20].

Determining the camera's field of view is done by imaging a razor blade. The sharp edge of razor blade can be easily seen on the image plane. The razor blade is placed right on the beam path near the predicted jet location in the same way as the neon lamp

case. The spectrometer entrance slit is set to 1mm width for this calibration. There is a sharp change of black and white color on the focused CCD camera image where the razor blade edge is located. Then, the razor blade is moved along the beam path to determine where the right and left limitations are. The distance moved is the camera's field of view can be expressed in terms of the length of space viewed by each pixel. Based on the previous research, the injection jet plume width itself has a size of about 30mm [5]. The camera distance relative to the jet location is adjusted to have a suitable field of view, 4.2mm of spatial distance, each pixel is viewing 0.016mm for this study. The jet center has to be placed right at the center of the camera field of view for achieving a symmetric data signal.

The number density of each species can be determined by establishing the linear relationship between the number density of each gas and the intensity of signal image acquired by the CCD camera. This calibration was performed by filling the injection chamber with known concentrations of nitrogen, methane, and ethylene each time. Assuming uniform distribution, the number density inside the chamber is following the perfect gas relation, that is

$$\rho_{species} = \frac{P_{species}}{R_{species} T_{species}} \tag{12}$$

The chamber pressure and temperature of each gas is the same as the chamber, those two parameters can easily be determined. The molar density, $C_{species}$, can be determined by the equation below:

$$C_{species} = \frac{\rho_{species}}{MW_{species}} \tag{13}$$

where MW_{specie} is the molecular weight of each nitrogen, methane, and ethylene which is 28.01, 16.04, 28.05 respectively [21]. Then, the number density can be founded by

$$N_{species} = C_{species} N_A \tag{14}$$

where N_A is Avogadro's number (6.02×10^{23}). The purity of gases used for this calibration is the same purity of the gases used for actual data acquisition, 99.95% of nitrogen, 99.99% of methane and ethylene. The chamber is evacuated using shop air before filling each time. It is observed 10Kpa is always left inside the chamber, however that does not affect the signal calibration at all. As mentioned earlier, the chamber pressure transmitter is providing ±0.1% accuracy. The background signal of ambient light condition is taken for each gas without the laser, before taking the calibration data for the use of background image subtraction, assuming the background intensity of the calibration image is the same and uniform as the background intensity of ambient light condition. However, as will be described more in the data processing section, the three background images on its image itself is used for background subtraction, due to the different background patterns caused by reflection, scattering and other light sources. It has a different background intensity profile compared to the background images taken before without the laser.

Before the background subtraction, it is necessary and important to select proper signal area for calibration. After the background signal was first subtracted, selected area of each species signal is integrated over each column pixel along the field of view, i.e. *x*-axis. The least square correction method is used to determine the best line fit over each integrated column for seven different number density cases. From the result of this method, 256 different calibration line fits are made for each species. Overall validity of

these lines are above 99.4% accuracy and the calibration line constants are displayed on Figure 22. Each line represents averaged slopes and intercepts values. The standard deviations of those numbers are shown in Table 3.

A small number of nitrogen signal intercepts show the calibration for nitrogen is more accurate than other species. The different slopes result from the different Raman scattering cross section as discussed in the previous chapter. The signal intensity is proportional to its cross section. The methane cross section of v_2 is close to that of ethylene (reference Table 2). Thus, the number density of each injecting species can be determined from measured signals using these linear curve constants of calibration.

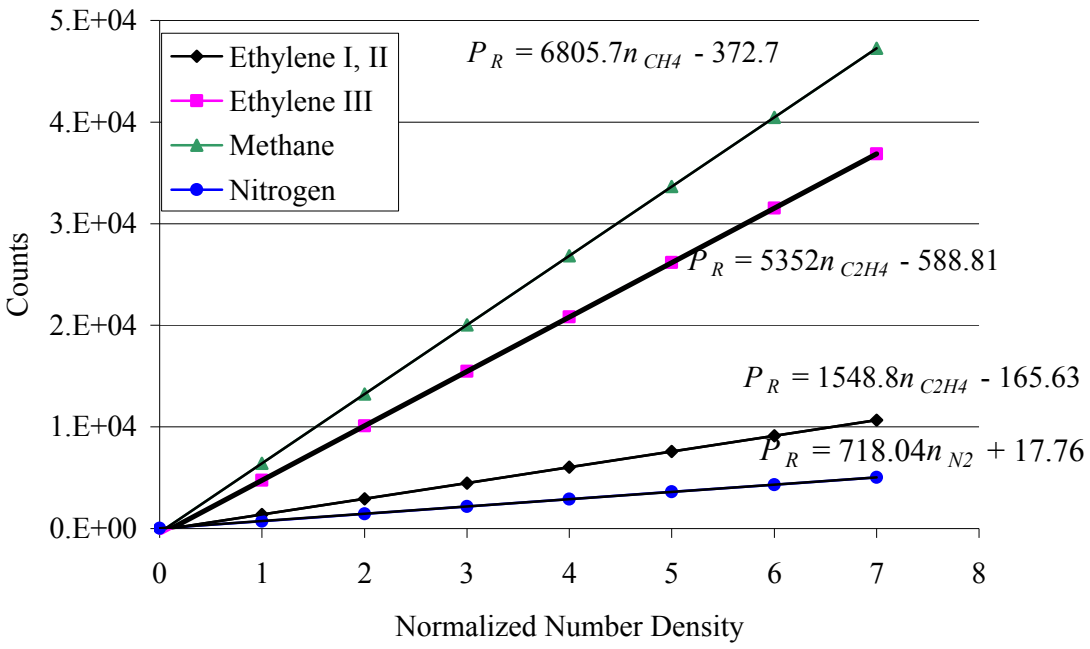

Figure 22. Calibration curve fit of Raman scattering signal.

* Ethylene I, II: v_3, v_2 vibrational modes, Ethylene III: v_1 vibrational mode (Appendix E)

Table 3. Averaged calibration curve fit constants with standard deviations.

Raman Line	Slope	Intercept
Nitrogen	718.04 ± 43.3	17.76 ± 8.5
Methane	6805.7 ± 440.4	-372.7 ± 29.7
Ethylene I, II	1548.8 ± 123.6	-165.63 ± 13.6
Ethylene III	5352 ± 628.5	-588.81 ± 64.9

Experimental Procedure

Overview.

There are two main experimental sets. One is shadowgraph and the other is Raman spectroscopy. Both the shadowgraph and the Raman spectroscopy are for characterizing and determining the species distribution profile of the supercritical jet. Since the Raman spectroscopy is sensitive to molecular species, the accumulator is flushed out once before the initial filling of fuel to avoid the presence of unwanted gas species. Then, the fuel is charged in one side of the accumulator and nitrogen in the other side to control the desired supply pressure by the regulator. A methane/ethylene mixture is prepared manually, by Dalton's law of partial pressure. The number of moles of each gas is the partial pressure. The desired mole fraction of methane, X_{CH4}, can be found by

$$\frac{n_{CH4}}{(n_{CH4} + n_{C2H4})} = \frac{P_{CH4}}{(P_{CH4} + P_{C2H4})} = X_{CH4} \tag{15}$$

where n is a number density and P is a partial pressure.

The chamber regulator is pre-adjusted to provide a constant pressure level during the injection. After each injection, the 1.03Mpa shop air is on to vent the injected fuel and nitrogen gas out of the chamber. The chamber is flushed with nitrogen once again to

minimize the effect on the signal by the injected fuel remaining in the chamber for the Raman spectroscopy.

Shadowgraph.

The shadowgraph technique is relatively simple and similar to Raman spectroscopy once the image resolution and appropriate field of view is determined. Four different runs are performed for each nozzle, each run is corresponding to each temperature condition. The mass flow rate of the jet becomes steady state four seconds after injection begins. The entire image is acquired and saved to the computer. Then, 40 consecutive time-averaged images in the four second time frame are selected and averaged for improving the image quality.

Raman scattering.

Before testing begins, the laser is set to safe mode and proper alignment between optical set and chamber is observed at the beam off-angle. Then, the laser transition table is moved in the positive *y*-axis direction to the predetermined position. Since the Raman signal is very sensitive to light, all the unnecessary light in the laboratory is turned off. A dark covering is provided between the collection camera lens and the entrance slit. The spectrometer assembly is sealed off by black tape to minimize the interference of background lighting. Three sets of runs are performed for each temperature condition with four different nozzle configurations. After finishing four temperature conditions, the chamber is filled with air at ambient pressure and the laser intensity is reduced back down to safe mode. Then the chamber is closed until the nozzle is changed to another one. Each time the nozzle is changed, the laser needs to be realignment to the center of the jet. Assuming the jet has a circular cone shape and uniform distribution of molecules,

the center line is where the largest number of molecules is detected. At the centerline, the larger number of molecules scatter the signal much more than other areas. Then, the stronger signal intensity can be acquired on the CCD camera. Just as with the shadowgraph, the jet becomes steady four seconds after the injection begins. The jet is controlled to not exceed eight seconds because the accumulation of the fuel in the chamber will affect the signal. The external trigger for the camera shutter is used to accurately measure the jet. It is connected to the apparatus initiated by the injection valve. The shutter is opened for two seconds and the image is viewed on the computer screen and saved as a TIF file. Three runs are performed for the same temperature and the intensity is averaged. Before running the jet, ten time averaged images are taken for background signal and subtracted from the signal image to have a better signal to noise ratio.

Testing Strategy

Test fuels for this study are pure ethylene, a mixture of ethylene and methane with methane mole fractions of 0.1 and 0.2. As mentioned earlier, typical fuels above the critical point start to crack down to simpler molecular species, particularly ethylene and methane. Thus, ethylene and methane are selected. Ethylene's critical point is near room temperature which minimizes system safety requirements. Also 0.1 and 0.2 mixture ratios are chosen to maintain the same test fluid as previous work. Nitrogen is used as the ambient gas because it is inert and its properties are close to the air. Fuel critical temperature and pressure point are calculated by the SUPERTRAPP program. The fuel temperatures for this study are chosen near the fuel critical point, as can be seen in Table

4 and are expressed as a reduced value, i.e., relative to the critical point values of each fuel. The pressure ratio of the injection pressure to the critical pressure is maintained constant throughout the test as are the injection pressure to the chamber pressure. The chamber regulator maintains constant chamber pressure according to the fuel injection pressure.

Table 4. Temperature and pressure ratios used for this study.

	T_r (T_{inj}/T_c)	P_r (P_{inj}/P_c)	P_{rc} (P_{inj}/P_{chm})
X_{CH4}	1.001	1.03	32
	1.01		
	1.02		
	1.04		

For the shadowgraph technique, the nozzle having the same orifice diameter, d = 1.0mm, is first used to identified the supercritical jet condensation process. This nozzle is the same nozzle as used by Wu et al. [5]. It is expect to show the same condensed jet process near the critical point and set the standard conditions of injection temperature. Then, the nozzle is replaced by four different nozzles. Injection image data and the Raman scattering data is obtained with the same injection temperature condition set by the 1.0mm nozzle. The Raman signal is very sensitive to the ambient light condition, so it is preferable to take all the data under the same ambient condition. The tests were performed with X_{CH4} = 0.1 mixture fuel. And pure ethylene fuel in one day and X_{CH4} = 0.2 mixture fuel on the following day.

This research is one of only a few to use Raman spectroscopy to study similar phenomena. There is only one research study conducted similarly using supercritical pure ethylene jets. Therefore, determination of data accuracy is one of the critical steps to

proof whether the resulting data is valid or not. The certified methane/ethylene mixture gas with methane mole fraction 0.1 is used for filling up the tank with known concentration to determine mole fraction ratio of the ethylene to the methane. If the resulting mole fraction ratio is exactly nine, the overall data processing and calibration are accurately done. The same data processing method can then be applied to the Raman signal data with manually mixed fuels.

During the course of the experiment, the entire laser table is moved 5.0mm in the negative *x*-axis direction to relocate the jet centerline at the center of the camera field of view. For this reason, each species Raman signal is moved three pixels to the right along the wavenumber axis. This could affect the background pattern. Therefore, there might be inconsistency between the calibration data and the injection data. Also, the certified fuel with the methane mole fraction 0.1 was not enough to cover all amount of testing. The manually mixed fuel is used for the Raman spectroscopy. Thus, it is not sure how accurate the mole fraction is for the mixture fuel. The only way to determine the fuel mole fraction is taking the Raman signal data of the injection fuel after filling the chamber with known concentrations. It can be determined using the calibration correlation constants. The detailed results of this step are discussed on the next chapter.

Data Processing

Shadowgraph Image.

The imaging process for the shadowgraph is fairly simple and straightforward. Entire sets of images taken during each run are stored in an external hard drive. Forty consecutive images are averaged in terms of intensity using the Image J® program. By

doing so, the shock wave structure and condensation can be recognized more clearly as seen in Figure 23 (b). The undesirable disturbances appearing in a couple of images along with turbulent irregularity around the jet structure are either removed or minimized. The averaged image is separated to the red, green, or blue color component. Blue color is filtered out by the glass filter, so it does not contribute to any image information. The green component image is selected and filtered by the custom made filter which uses Fast Fourier Transform to refine the image. As can be identified in Figure 23, the barrel shock structure looks clearer. The dark regions appeared on both sides of the image (c) can be easily identified that are not clear on the first two images, (a) and (b). Generally, on the shadowgraph image, the denser region appears as a dark region. For this image, the dark region represents a change in density gradient. The condensed phase molecules are represented in the gaseous phase. This kind of small condensed jet is hard to be distinguished on the raw image. The same shadowgraph image data processing procedures are applied throughout this research.

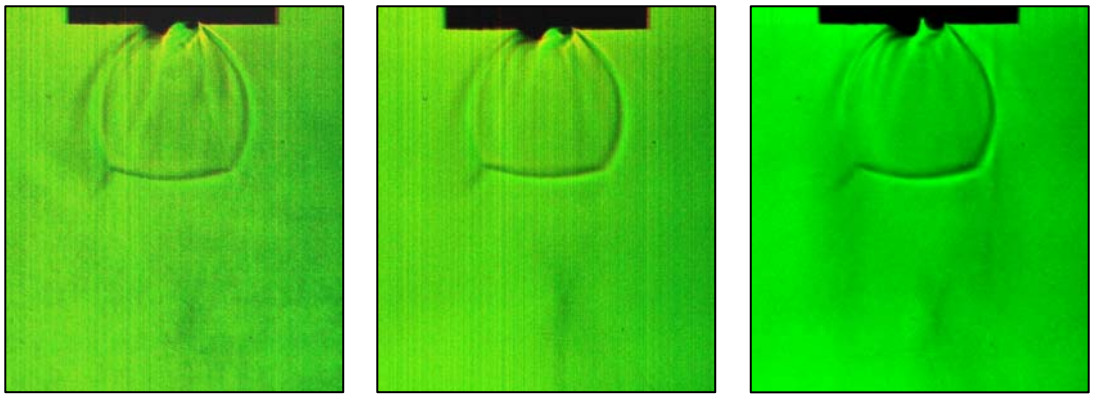

(a) (b) (c)

Figure 23. (a) The raw shadowgraph image data, (b) Averaged, (c) Filtered.

Raman Scattering Data.

The data processing of the Raman signal is relatively complicated and requires delicate processing due to the fact that the signal and the background intensity are sensitive to the area of selection. Any changes must be done uniformly across all images and any artificial data manipulation to make it look aesthetically pleasing must be avoided. Three images were taken for each test condition. The raw images of the CCD camera were saved on the computer as a Tiff file format and the Mathcad® program is used for the Raman scattering data processing. There are a few steps that need to be taken to reach the final destination of determining each species concentration profile. The raw image is a 256×256 pixel matrix containing intensity information of each species as wavenumber on the *x*-axis versus field of view on the *y*-axis. It is rotated 90° to the right to reorient as field of view on the *x*-axis as shown in the Figure 24 (a). The white line represents the corresponding species intensity profile and the dark region is the background signal on the image plane. Figure 24 (b) is the intensity profile along the wavenumber, *y*-axis. The peaks represent ethylene I and II spikes, nitrogen, and methane/ethylene III from the left respectively. The methane signal is hard to identify on the image of the Figure 24 (a) due to the small amount of methane mole fraction compare to ethylene. Although the intensity diagram of the Figure 24 (b) is showing there is a small peak of the methane signal right before the ethylene signal peak, it is impossible to separate the methane signal from the ethylene signal. The intensities of those species are overlapped and mixed together. Readjusting the spectral resolution risks loosing some species number density information because it can degrade the intensity of both gases.

Therefore, the method employed here is integrating methane and ethylene III line together over the field of view and subtracting ethylene I and II intensity from it. The methane intensity will be left and the number density can be determined from it. This process follows the background subtraction. In addition, Figure 24 (b) is showing there is no other foreign gas species signal appearing on the intensity diagram. Oxygen line is supposed to be located between ethylene II and nitrogen, but it is completely removed from the chamber by the shop air. It must be noted ethylene has three distinguishable signal lines containing different types of vibrational information for the same ethylene molecules. Ethylene I is at 1342frequency (H-C-H scis), ethylene II is at 1623nm frequency from v_2 vibractional mode (C=C stretching), ethylene III is at 3020nm frequency from v_1 vibractional mode (H-C-H stretching). The reason of integrating ethylene I and II together at the same time is to increase SNR. It is found another small methane signal line is located between the two.

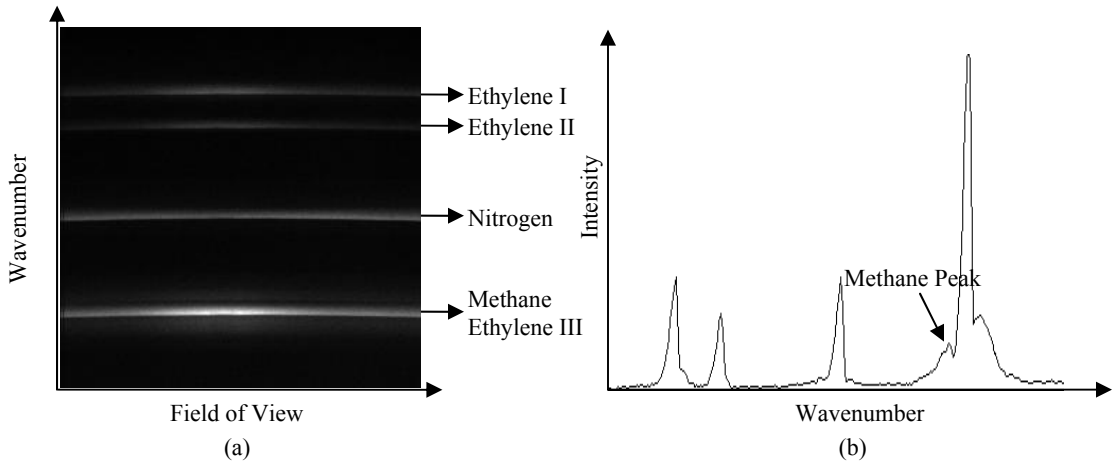

Figure 24. (a) Raman Image, (b) Intensity profile along the *y*-axis.

Figure 25 is showing the 3-dimensional intensity diagram of the image of Figure 25(a). The intensity is on the *z*-axis and its profile is different along the field of view axis. It needs to be noted relatively small signal intensity is still appearing around the ethylene III signal even though it is not clear on the image of Figure 25 (b), this is generally the same for all other signal lines. Thus, this kind of region must be avoided for selecting the background image area. Also, the brightest region of the ethylene III line on the image (Figure 24 (a)) corresponds to the peak area of intensity where the largest number density of ethylene III species exists on the 3-D diagram. It is expected that the peak intensity area is where the jet center is. In addition, the signal intensity deficit at the ethylene peak is caused by CCD camera defect. It is always at that location and this deficit affects the species mole fraction profile.

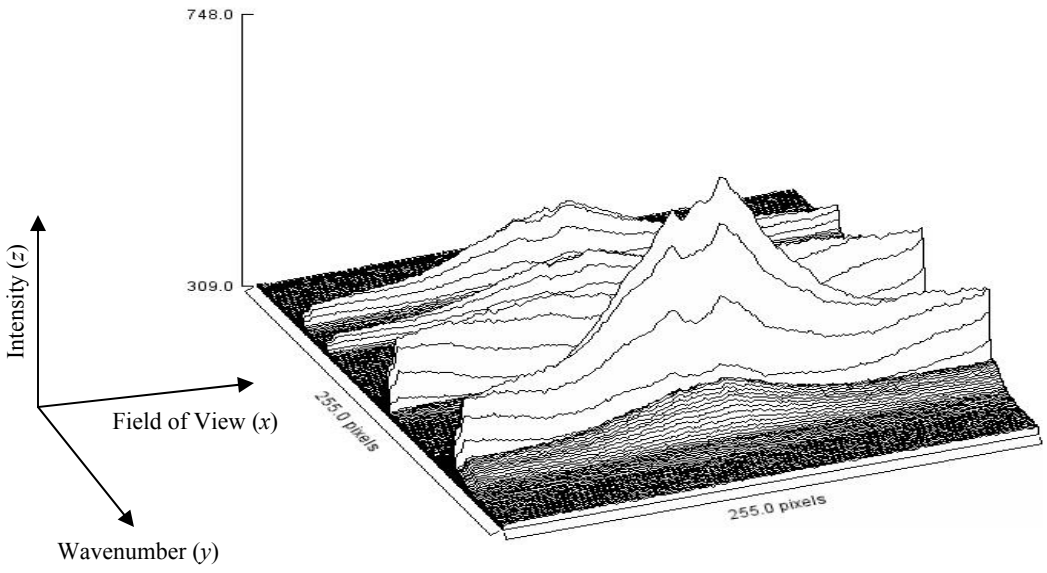

Figure 25. 3-D signal intensity profile by Image J® surface plot.

Subtracting appropriate background signal is the key to the success of this study for accurate results. However, the problem is every each image has different background

intensity profiles making the background subtraction difficult as shown in Figure 26. It appears as every image has the same and uniform background. However after adjusting the brightness of the image with Image J® program, it does not have a uniform intensity distribution on the background area. This irregular background is caused by the reflecting from internal structure of the chamber and the window of viewing port. It is expected also the signal line is affected by this back scattering too. It is also observed every image has different background intensity and the intensity profile is different from the area of selection on the same image itself. It tends to proportionally increase as the signal intensity increases for the calibration image data. Therefore, the image taken for background signal is no more useful because it has a uniform intensity. The appropriate background signal has to be selected and subtracted from both calibration and injection data processing consistently.

Three background images are taken from its own image data. The area between the signal lines are selected and averaged along the field of view axis and subtracted from the image data. Figure 26 shows how the background intensity profile varies along the *x*-axis as well as *y*-axis. Care must be provided to select the background image which contains the closest intensity profile to the signal line, while also avoiding the signal line. Once the background area is determined, the same area is used for background image subtraction for all the data images throughout the processing for consistency. For this study, the areas between ethylene II and oxygen, oxygen and nitrogen, nitrogen and methane/ethylene III lines are selected. Each area of selection has seven rows. Those areas are integrated over field of the view axis and averaged to give a single line intensity profile.

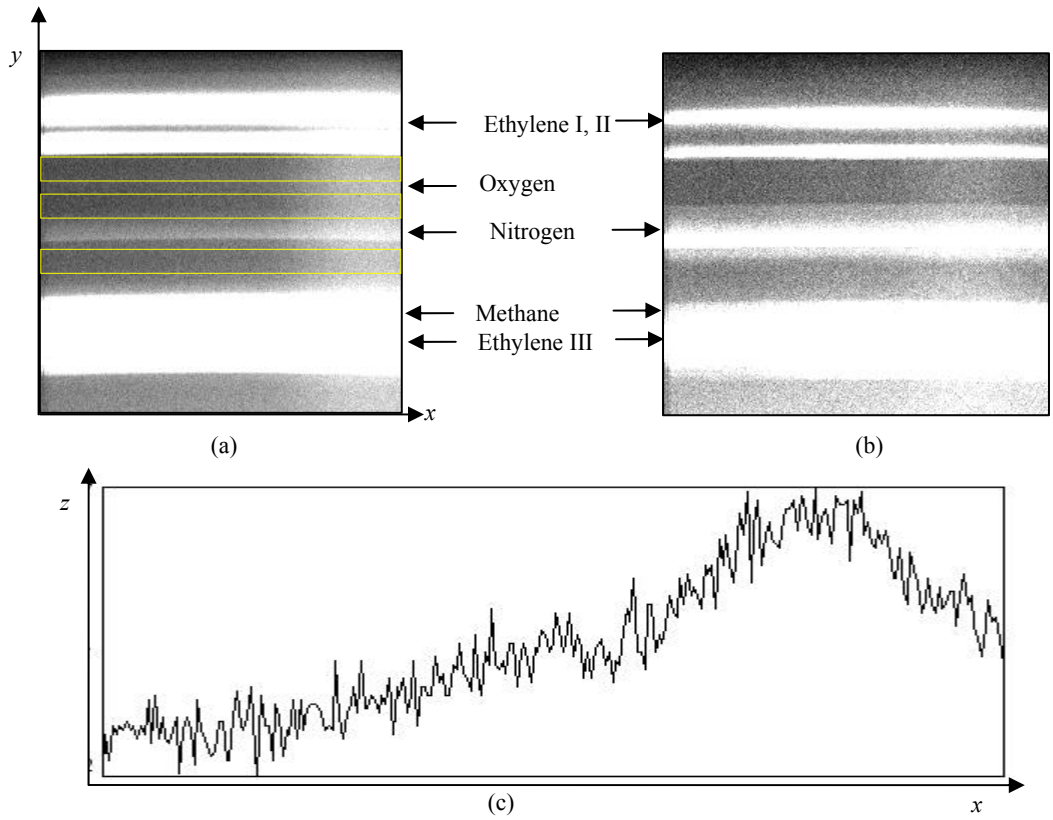

Figure 26. Different background intensity profile. (a) Ethylene calibration data, (b) X_{CH4} = 0.1 mixture data, (c) Background intensity profile.

Once the proper background signal is subtracted from the data, the number density of methane and ethylene has to be determined. Since the methane and ethylene signal is located very close to each other, it is difficult to separate them. Fortunately, there are two more ethylene lines located at different wavenumber. These lines are from different vibrational modes of the same ethylene molecules. The ethylene intensity of those two lines are smaller than of the ethylene III line because the cross section is much smaller. However, the number density will be the same. Therefore, inserting the intensity from those ethylene I and II lines into the corresponding calibration curve fit determines

the ethylene number density, which is eventually the same number as the ethylene line close to the methane signal. The equation for determining ethylene number density is:

$$P_{RC2H4} = an_{C2H4} + b \tag{16}$$

where a and b are coefficients of the corresponding calibration line and P_R and n_i are number density and intensity, respectively. The next step is to insert this number density into the calibration curve fit of the ethylene III signal to determine the intensity. The integration of the main ethylene and methane signal produces the total intensity of ethylene and methane. Subtracting off the ethylene III intensity determined by its own calibration curve from the total intensity gives just the methane intensity itself. Finally, the methane number density can be determined by inserting the methane intensity into its own calibration curve fit. Consequently, the methane and ethylene number density are determined individually and the mole fractions of each gas can be derived from the number density.

The exact same manner is applied to the nitrogen signal; integration over the field of view axis to determine the intensity profile. The nitrogen number density can be determined by inserting the intensity profile into its own calibration curve fit.

IV. Results and Discussion

Chapter Overview

The main purposes of the shadowgraph images are the identification of the jet global appearance and finding the jet condensation condition in terms of injection temperature. The previous research explored the injection temperature effects on the supercritical jet condensation process. The near-field jet characteristics are well discussed in terms of axial location and size of the Mach disk and expansion angle. Therefore, it is not necessary to repeat the whole process in this study, but the same procedure is repeated to find the jet condensation condition which might be slightly different from the previous work since a smaller nozzle diameter is used. The nozzle with the same nozzle diameter is used to compare the difference between a smaller nozzle diameter and the previous work. The shadowgraph image results for the different nozzles are compared to identify the nozzle design effects on the jet shape and condensation. The Raman scattering technique is employed at the jet down stream location to determine molecular profiles.

The mole fraction of ethylene, methane, and nitrogen at different injection temperature conditions are studied to identify the condensation effects on the fuel mixing process with the air (nitrogen in this study). The mole fraction ratio of ethylene to methane for each fuel condition is also studied to clarify whether there is any preferential condensation within the jet. In addition, each species mole fraction for the different nozzles is compared to determine which nozzle design is better than another in terms of mixing characteristics, which is the fast spreading rate. Those three main themes are the main discussion points. The methane's signal to noise ratio (SNR) is relatively lower than

ethylene and nitrogen due to its small mole fraction, significantly adding uncertainty to the results. Therefore, the main discussion will be on the ethylene and the nitrogen signal data. In addition, each nozzle's potential core length is computed using the relation provided by Chehroudi et al. for characterizing the jet (Chapter II).

This chapter begins with the discussion of the shadowgraph results over various temperature range and different nozzles. It will be followed by the Raman scattering results discussion in terms of ethylene mole fraction and mole fraction ratio of ethylene/methane. Both the shadowgraph and the Raman scattering result are presented in the order of supercritical ethylene, X_{CH4} = 0.2, 0.1 mixture fuel. Also, it needs to be noted that a lot of discussions presented in this chapter are the comparison to the previous work done by Wu et al. [5]. The jet divergence angle and potential core length are also discussed to identify nozzle and condensation effects.

Shadowgraph Results

Supercritical Ethylene Fuel Injection.

Figure 27 is showing the actual injection condition with the injection temperature ratio ($T_r = T_{inj}/T_c$) versus injection pressure ratio ($P_r = P_{inj}/P_c$) for each nozzle. These data points are taken at four second after injection begins. All the injection conditions are in the supercritical region, although there are variations due to the system inaccuracy. Generally, the injection pressure ratio is maintained at a constant for all the cases varying within 0.01 pressure ratio range. The injection temperature ratios are varied also from 1.01 to 1.04 which are well agree with the ratio values of the testing strategy. For nozzle #8, three runs are conducted with T_r = 1.01, 1.04, 1.08 for the comparison to the previous

work done by Wu et al. [5]. The pressure ratio of the injection pressure to the chamber ($P_{rc} = P_{inj}/P_{chm}$) is maintained a constant, $P_{rc} = 30$, although this is not shown in Figure 27.

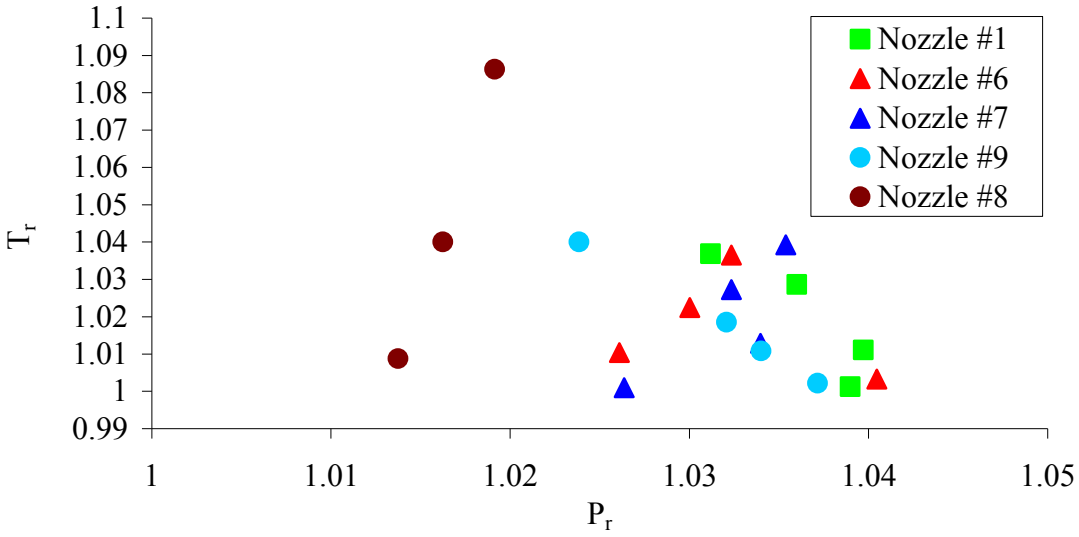

Figure 27. Shadowgraph image injection condition, ethylene fuel.

Generally, a lot of condensation is observed as the injection temperature approaches the critical temperature. Figure 29 is showing the condensed jet shadowgraph image with $d = 1.0$mm nozzle at $T_r = 1.01$, $P_r = 1.01$ condition. The dark region is considered a condensed jet since the density of the liquid phase is higher than gaseous phase. According to Wu et al, the barrel shock is still formed inside the condensed jet, but it is hard to recognize. It is obvious as the injection temperature increases shown in Figure 29. The increased injection temperature does not produced as much condensed jet as the previous case. As shown in Figure 29, less condensation is observed at $T_r = 1.04$, $P_r = 1.01$ injection condition, but there is still small amount of condensed jet around the barrel shock structure. The barrel shock is formed because this is a supersonic jet and an under expanded shock structure forms. As the injection temperature moves further away to $T_r = 1.08$, the jet becomes transparent. This is predicted trend based on the entropy-

pressure diagram as shown in Figure 4 in chapter II. Since the supercritical injection jet is considered isentropic expansion process, as the injection temperature is approached the critical temperature point, it enters the two phase region (liquid and vapor) which is depicted in the same Figure 5 of chapter II. However, as the injection temperature increases and moves away from the critical temperature, the injection process enters the vapor regime. There is no condensed jet in this region. The shadowgraph result of nozzle #8 shows as the injection temperature increases the condensation is less significant. This result is well agreed with the result of previous study done by Wu et al. [5].

In addition, the Mach disk size and the jet plume are bigger than those of the smaller nozzle diameter. The bigger nozzle diameter produces larger mass flow rates which is proportional to the nozzle diameter. The condensed jet does not appear at T_r = 1.08, therefore the injection temperature ratio for the rest of the research is focused on the very near critical temperature point; T_r = 1.00, 1.01, 1.02, 1.04. The first case of injection temperature ratio case, T_r = 1.00, is rounded off number. The actual value is greater than T_r = 1.00, but very close to it. It needs to be noted the triangle pattern in the jet plume is not shock structure, it is the background pattern caused by the chamber optical windows.

It must be noted that the injection jet shows isentropic expansion (barrel shape shock structure) and after that it is no more isentropic expansion. Also, the jet is not in the supercritical condition at z/d = 100 location.

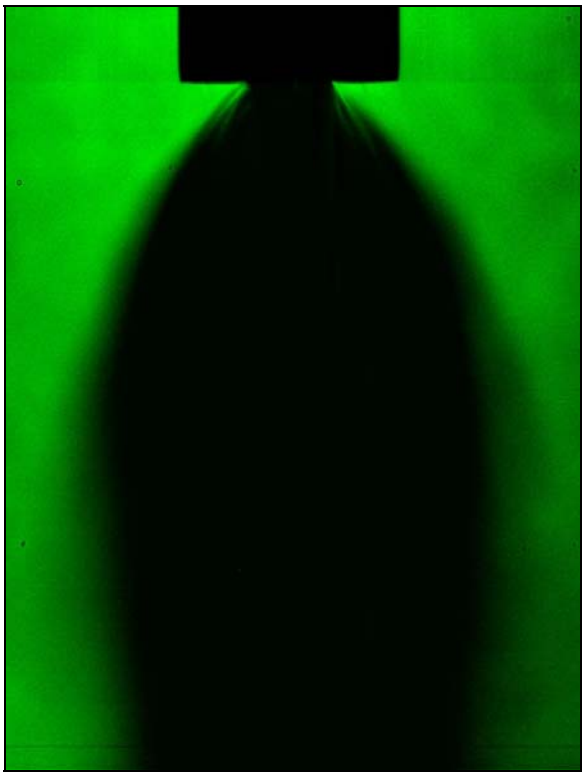

Figure 28. Shadowgraph image, ethylene, nozzle #8, d = 1mm, T_r = 1.01, P_r = 1.01

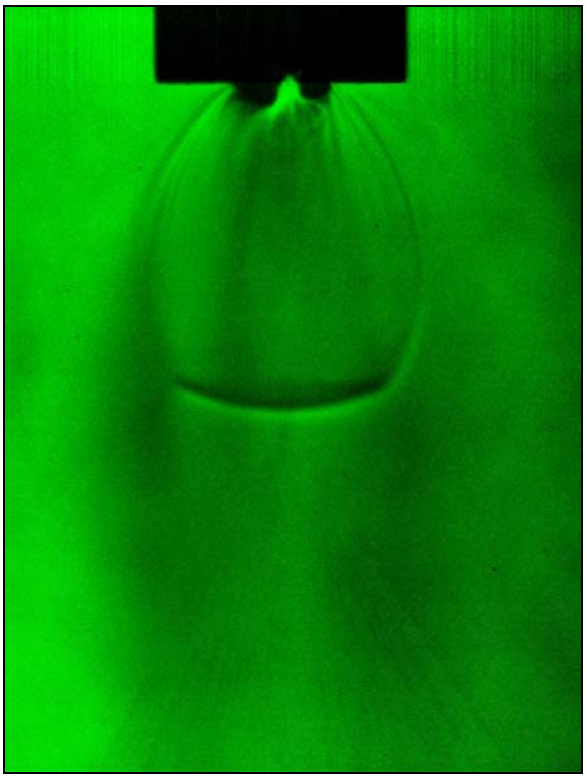

Figure 29. Shadowgraph image, ethylene, nozzle #8, d = 1mm, T_r = 1.04, P_r = 1.01

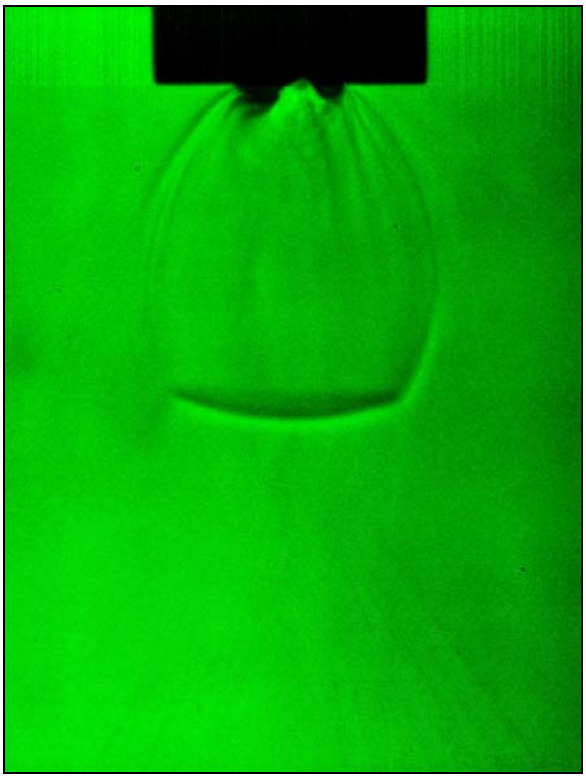

Figure 30. Shadowgraph image, ethylene, nozzle #8, d = 1mm, T_r = 1.08, P_r = 1.02

Four nozzles with a small nozzle diameter (d = 0.5mm) are used to study the condensation process, whether it occurs the same way or not, as well as whether any particular condensation is observed depending on the nozzle configuration. The fuel critical temperature and pressure point are different from those of pure ethylene. However, the injection pressure ratio remained at the same value as nozzle #8. Each nozzle has four different injection temperature ratios; 1.00, 1.01, 1.02, 1.03. The chamber pressure ratio also maintains a constant value of P_{rc} = 30.

The same jet condensation process is observed throughout the different injection temperatures and nozzles. The barrel shock size is smaller than for the nozzle #8 cases due to the smaller nozzle diameter (mass flow rate). Also, the amount of condensation is

slightly reduced comparing to the nozzle #8 cases. Figure 31 and 35 show the condensations are occurring at the outer edge of the barrel shock.

Nozzle #6 is producing a relatively small amount of condensation on both sides of the barrel shock. Most of the shadowgraph image is showing the jet has a symmetrical shape. In addition, as the injection temperature increases the condensation is hard to identify. There might still be a very small amount of condensation where still noticeable amounts of condensation are produced in the same case of nozzle #8, Figure 29.

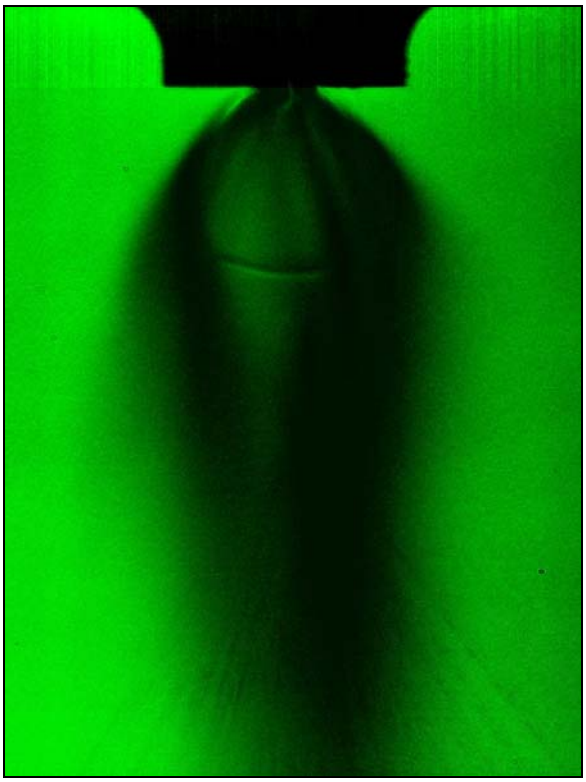

Figure 31. Shadowgraph image, ethylene, Nozzle #1, d = 0.5mm, T_r = 1.00, P_r = 1.03

Figure 32. Shadowgraph image, ethylene, nozzle #1, d = 0.5mm, T_r = 1.01, P_r = 1.03

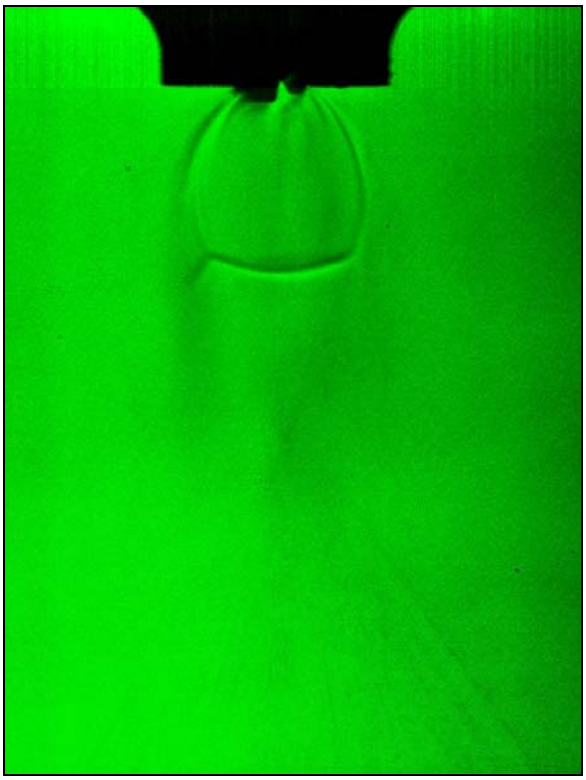

Figure 33. Shadowgraph image, ethylene, nozzle #1, d = 0.5mm, T_r = 1.02, P_r = 1.03

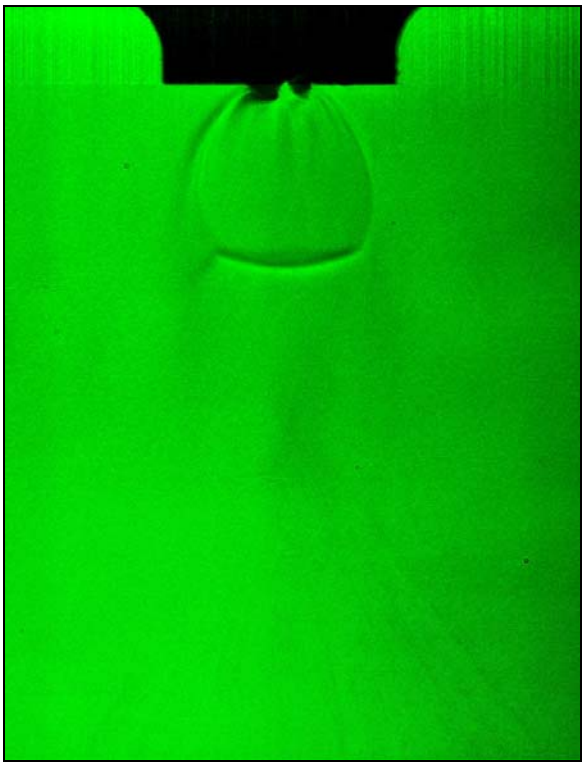

Figure 34. Shadowgraph image, ethylene, nozzle #1, d = 0.5mm, T_r = 1.03, P_r = 1.03

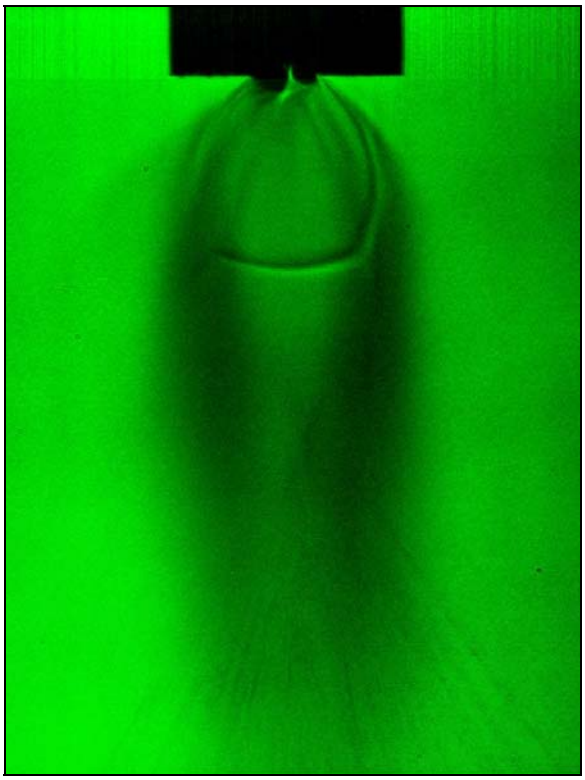

Figure 35. Shadowgraph image, ethylene, nozzle #6, d = 0.5mm, T_r = 1.00 P_r = 1.04

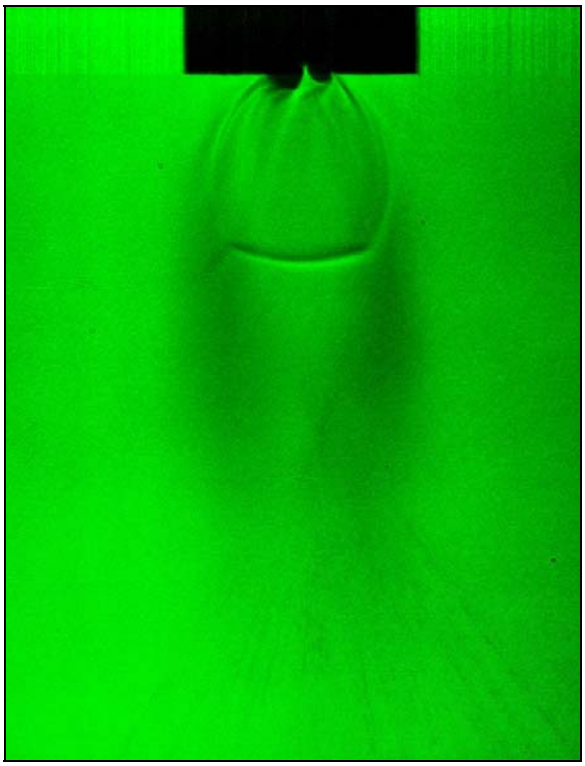

Figure 36. Shadowgraph image, ethylene, nozzle #6, d = 0.5mm, T_r = 1.01 P_r = 1.03

Figure 37. Shadowgraph image, ethylene, nozzle #6, d = 0.5mm, T_r = 1.02 P_r = 1.03

Figure 38. Shadowgraph image, ethylene, nozzle #6, d = 0.5mm, T_r = 1.03 P_r = 1.03

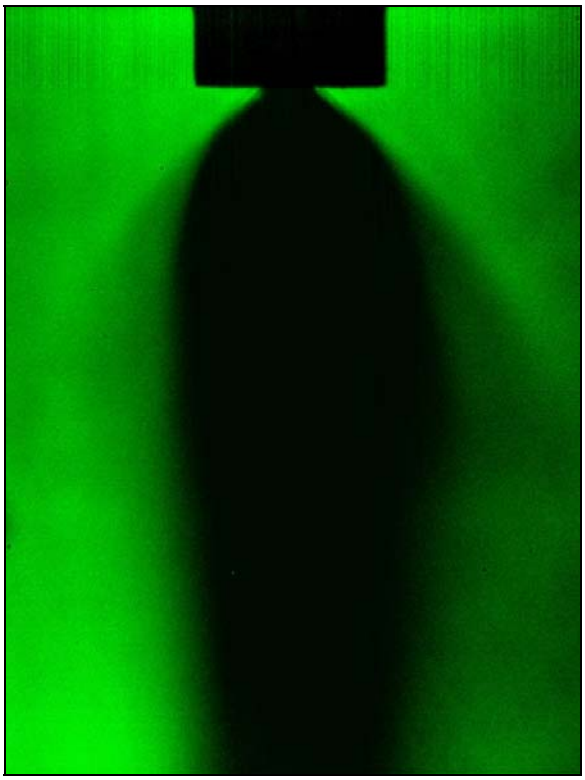

Figure 39. Shadowgraph image, ethylene, nozzle #7, d = 0.5mm, T_r = 1.00 P_r = 1.02

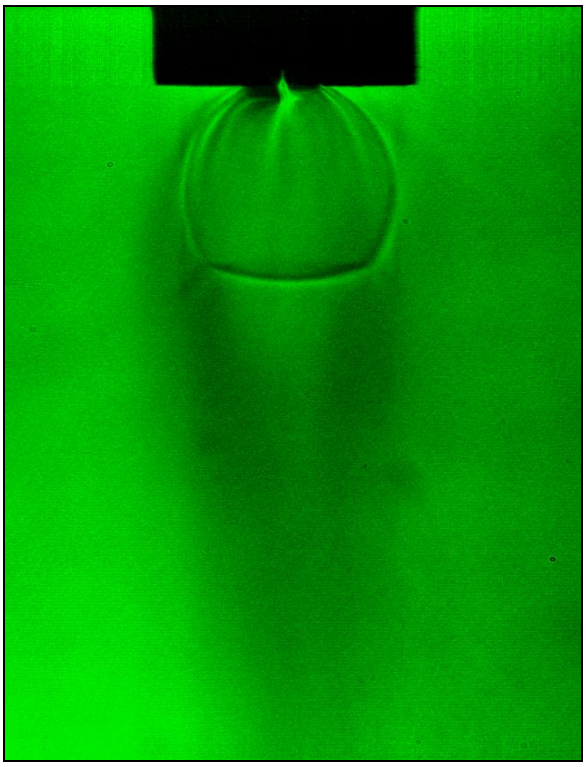

Figure 40. Shadowgraph image, ethylene, nozzle #7, d = 0.5mm, T_r = 1.01, P_r = 1.03

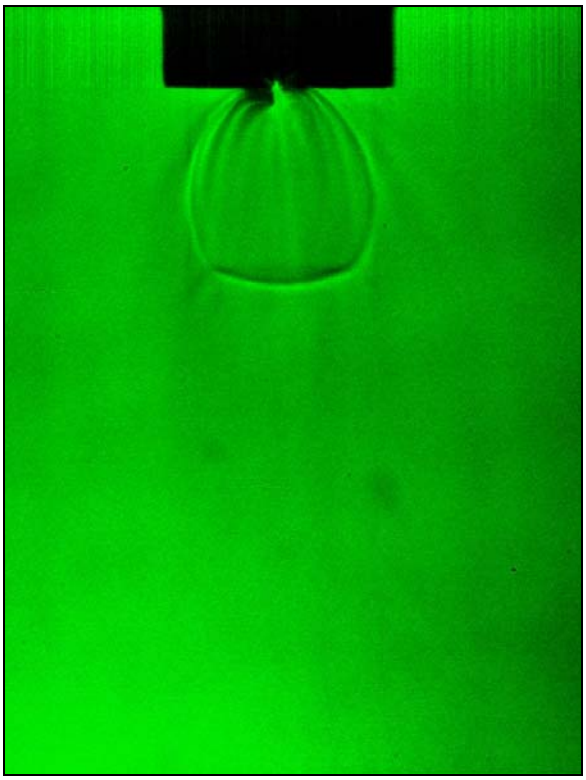

Figure 41. Shadowgraph image, ethylene, nozzle #7, d = 0.5mm, T_r = 1.02, P_r = 1.03

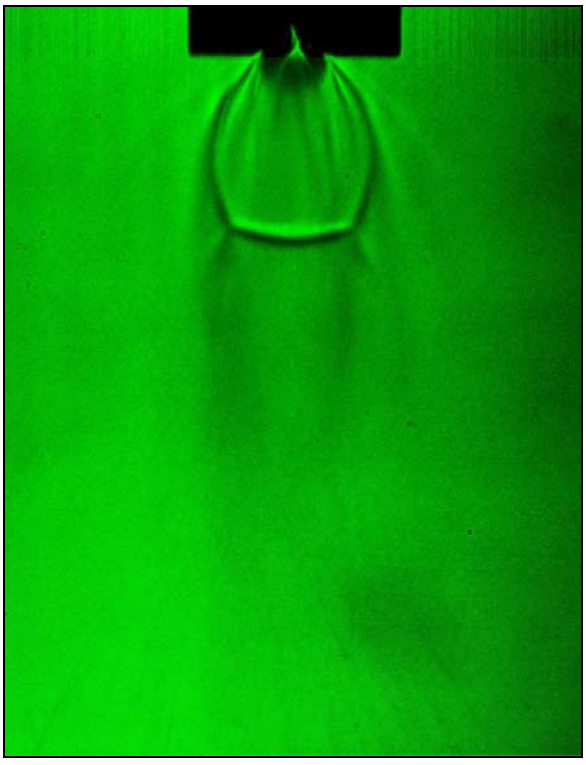

Figure 42. Shadowgraph image, ethylene, nozzle #7, d = 0.5mm, T_r = 1.03, P_r = 1.03

Figure 43. Shadowgraph image, ethylene, nozzle #9, d = 0.5mm, T_r = 1.00, P_r = 1.03

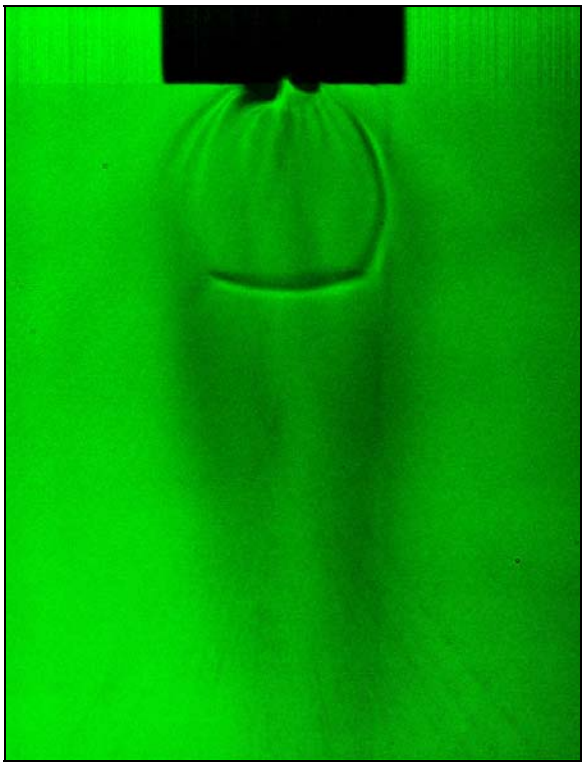

Figure 44. Shadowgraph image, ethylene, nozzle #9, d = 0.5mm, T_r = 1.01 P_r = 1.03

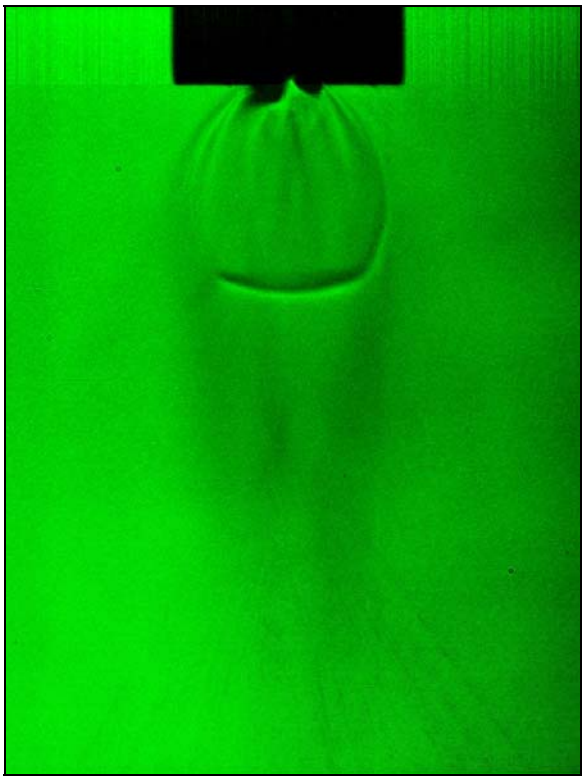

Figure 45. Shadowgraph image, ethylene, nozzle #9, d = 0.5mm, T_r = 1.02 P_r = 1.03

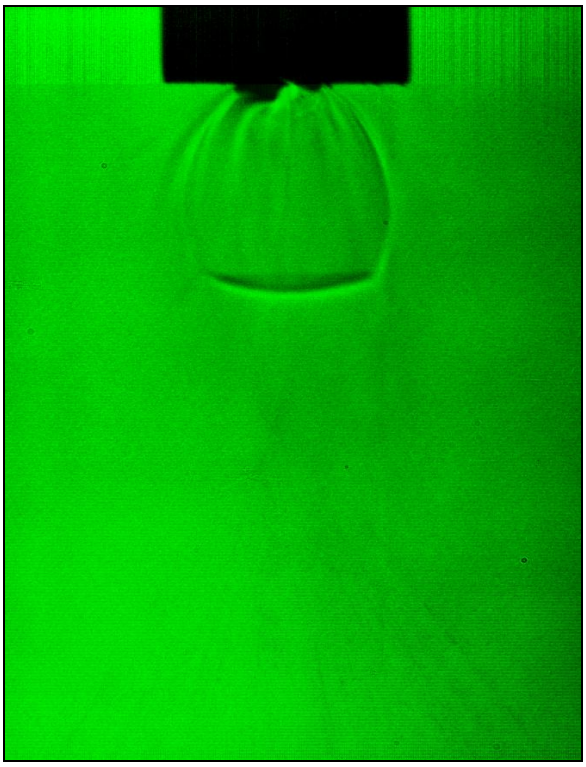

Figure 46. Shadowgraph image, ethylene, nozzle #9, d = 0.5mm, T_r = 1.04 P_r = 1.02

Supercritical Methane and Ethylene Mixture (X_{CH4} = 0.1) Fuel Jet.

The same injection condition is maintained fro these test cases, while the injection pressure ratio is a little bit higher than the ethylene injection. The pressure ratio of nozzle #9 and nozzle #7 are lower than others. This is because the fuel supply is limited. But, all the injection conditions are inside the supercritical region.

Also, the same result is observed. An asymmetric condensed jet is produced possibly caused by injection tube machining irregularities.

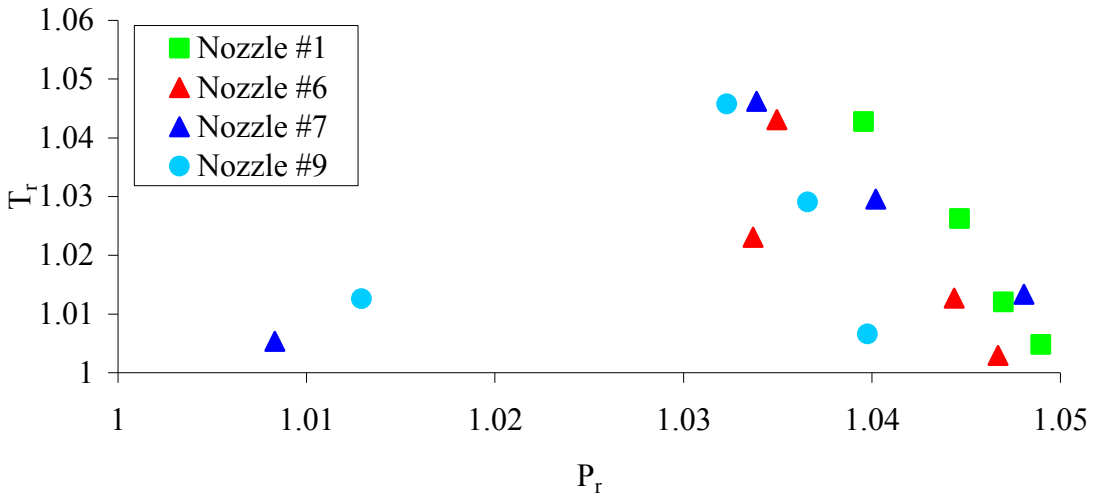

Figure 47. Shadowgraph image injection conditions, X_{CH4} = 0.1 mixture fuel.

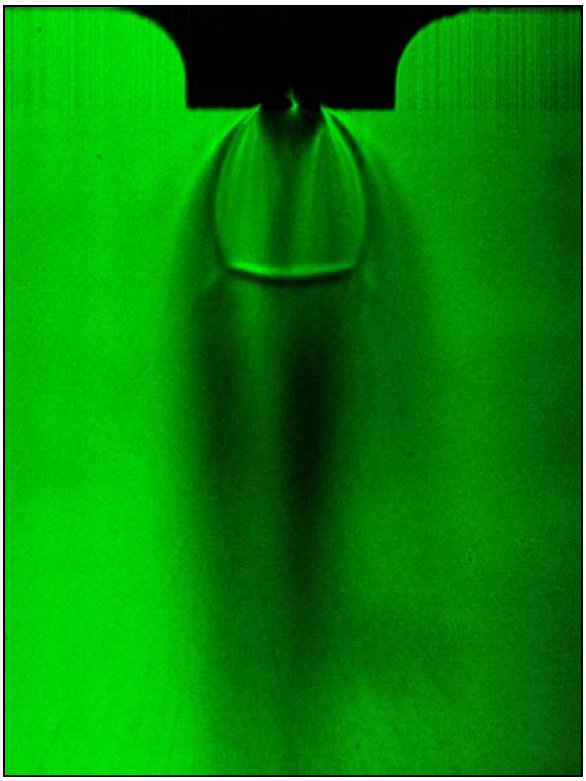

Figure 48. Shadowgraph image, $X_{CH4} = 0.1$, nozzle #1, $d = 0.5$mm, $T_r = 1.00$, $P_r = 1.04$

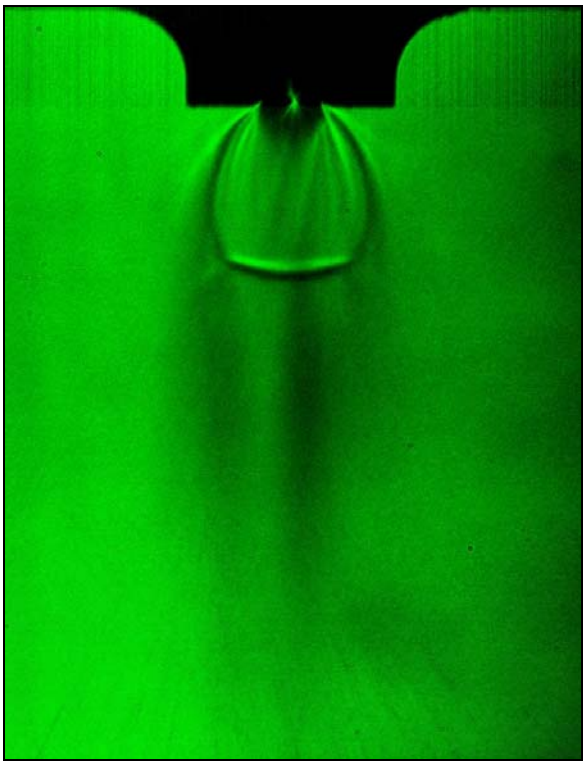

Figure 49. Shadowgraph image, $X_{CH4} = 0.1$, nozzle #1, $d = 0.5$mm, $T_r = 1.01$, $P_r = 1.04$

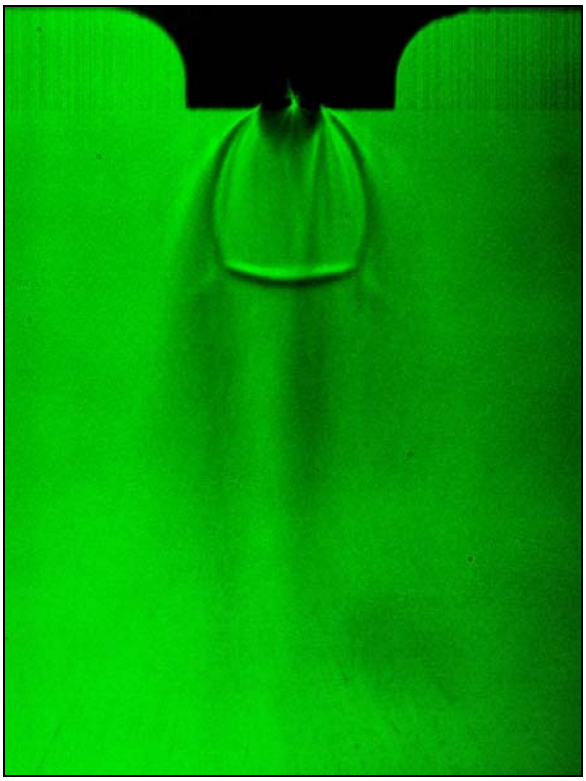

Figure 50. Shadowgraph image, $X_{CH4} = 0.1$, nozzle #1, $d = 0.5$mm, $T_r = 1.02$, $P_r = 1.04$

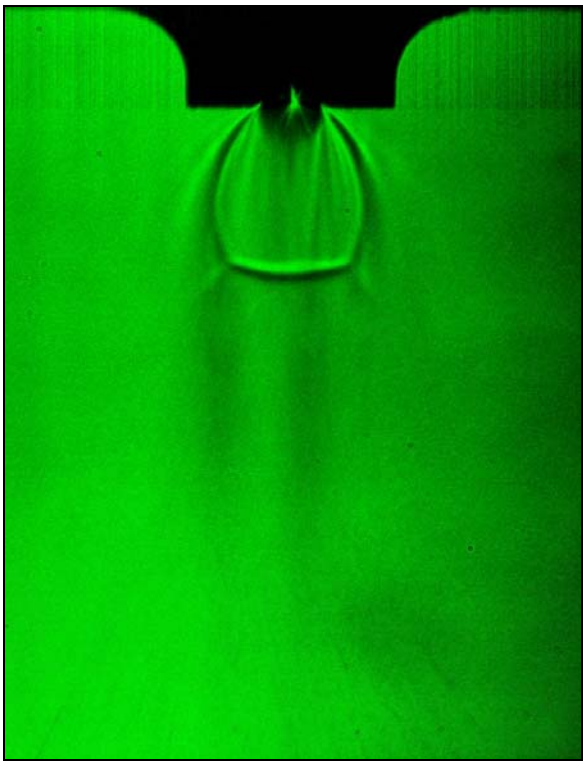

Figure 51. Shadowgraph image, $X_{CH4} = 0.1$, nozzle #1, $d = 0.5$mm, $T_r = 1.04$, $P_r = 1.04$

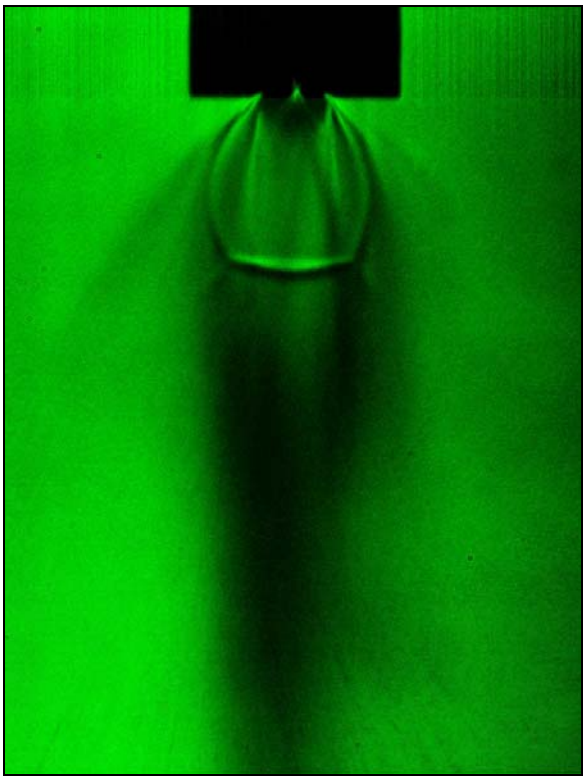

Figure 52. Shadowgraph image, $X_{CH4} = 0.1$, nozzle #6, $d = 0.5$mm, $T_r = 1.00$, $P_r = 1.04$

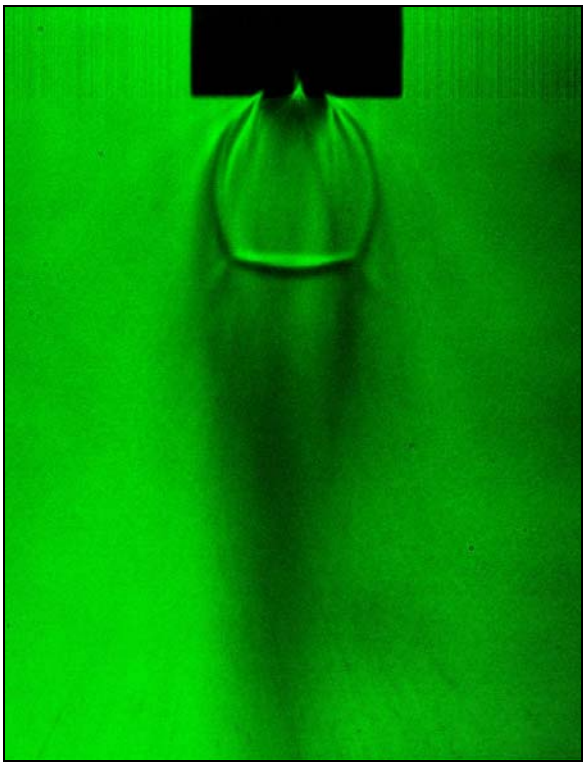

Figure 53. Shadowgraph image, $X_{CH4} = 0.1$, nozzle #6, $d = 0.5$mm, $T_r = 1.01$, $P_r = 1.04$

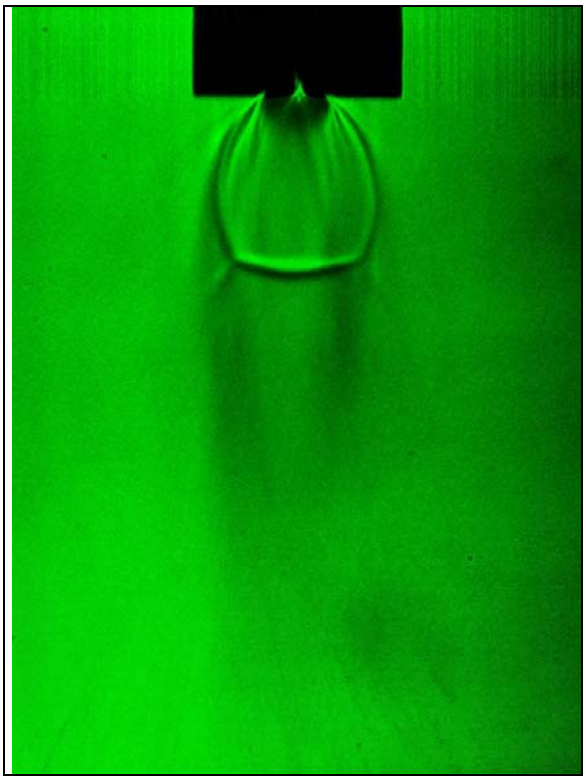

Figure 54. Shadowgraph image, X_{CH4} = 0.1, nzzle #6, d = 0.5mm, T_r = 1.02, P_r = 1.03

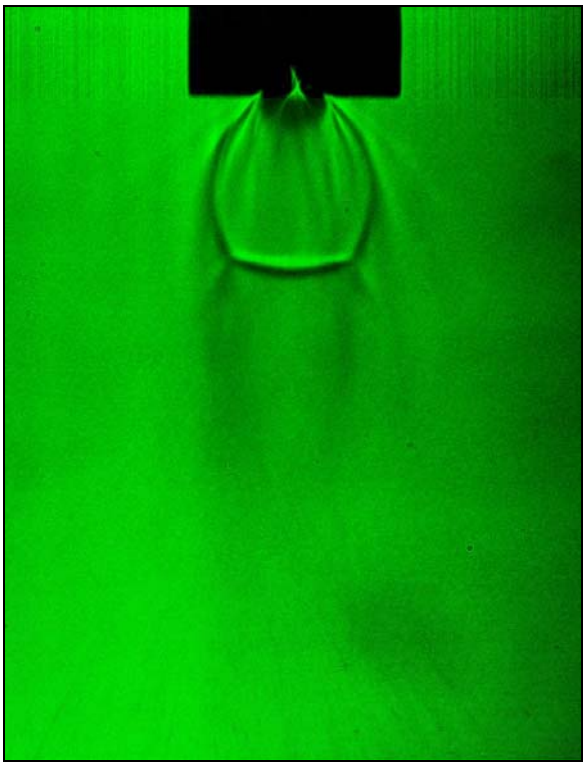

Figure 55. Shadowgraph image, X_{CH4} = 0.1, nozzle #6, d = 0.5mm, T_r = 1.04, P_r = 1.03

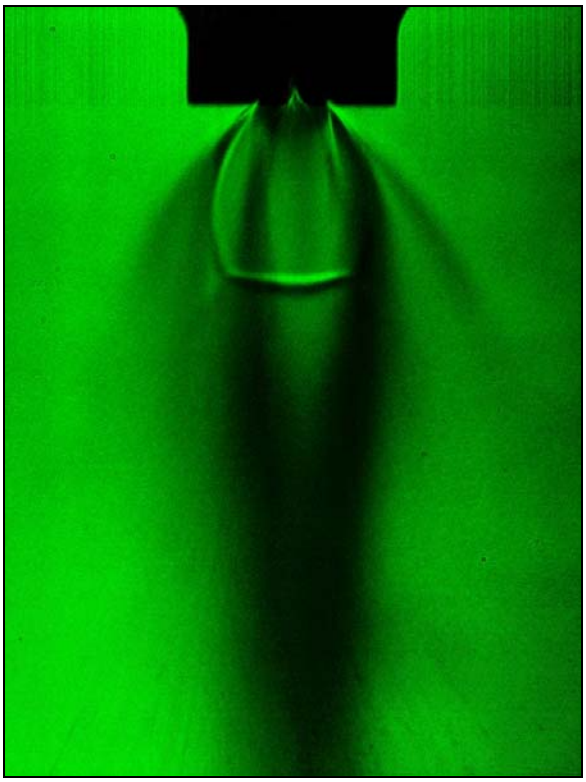

Figure 56. Shadowgraph image, $X_{CH4} = 0.1$, nozzle #7, $d = 0.5$mm, $T_r = 1.00$, $P_r = 1.01$

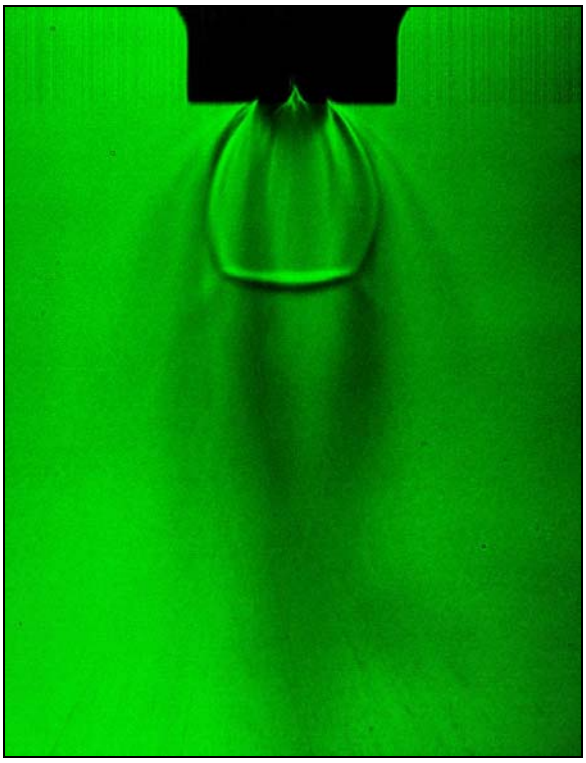

Figure 57. Shadowgraph image, $X_{CH4} = 0.1$, nozzle #7, $d = 0.5$mm, $T_r = 1.01$, $P_r = 1.04$

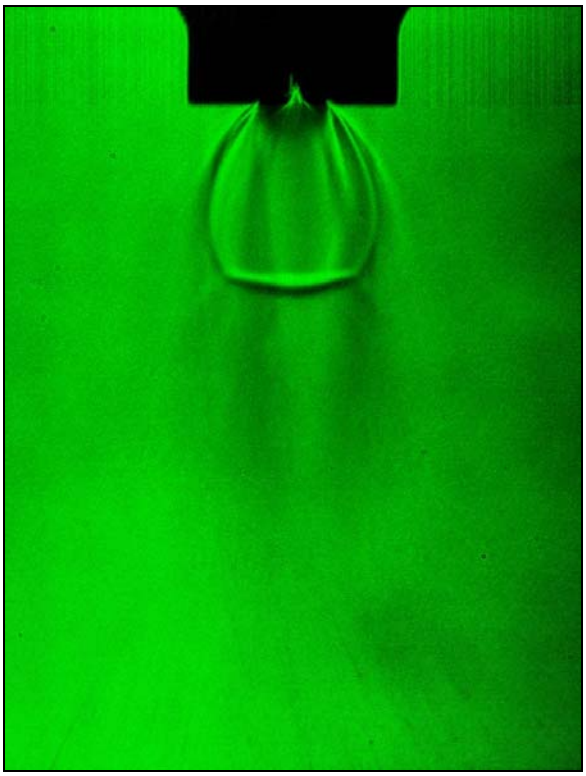

Figure 58. Shadowgraph image, $X_{CH4} = 0.1$, nozzle #7, $d = 0.5$mm, $T_r = 1.03$, $P_r = 1.04$

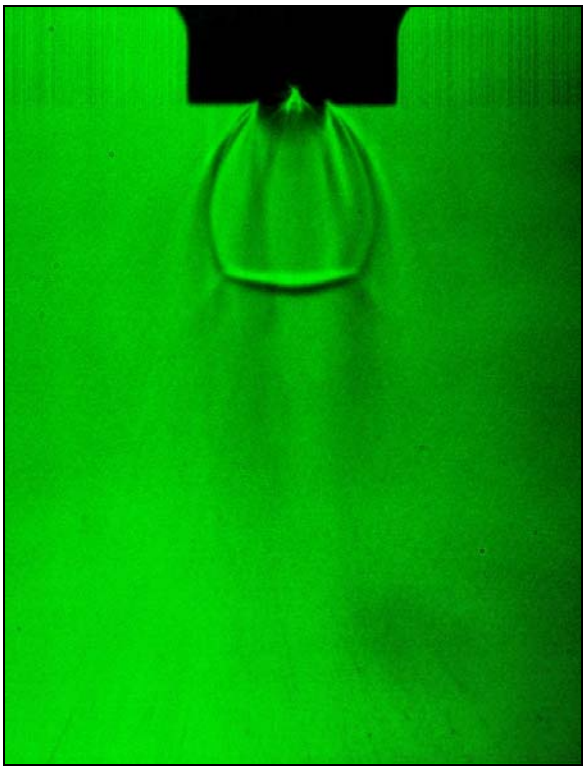

Figure 59. Shadowgraph image, $X_{CH4} = 0.1$, nozzle #7, $d = 0.5$mm, $T_r = 1.04$, $P_r = 1.03$

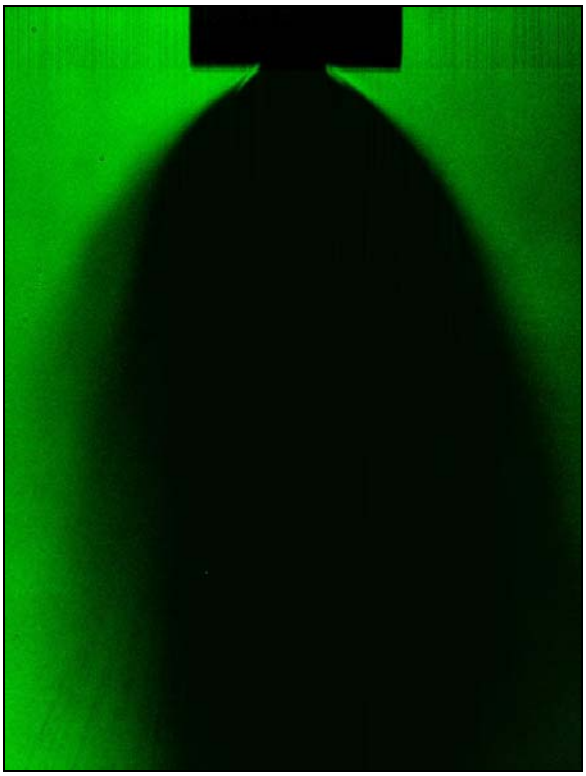

Figure 60. Shadowgraph image, $X_{CH4} = 0.1$, nozzle #9, $d = 0.5$mm, $T_r = 1.00$, $P_r = 1.04$

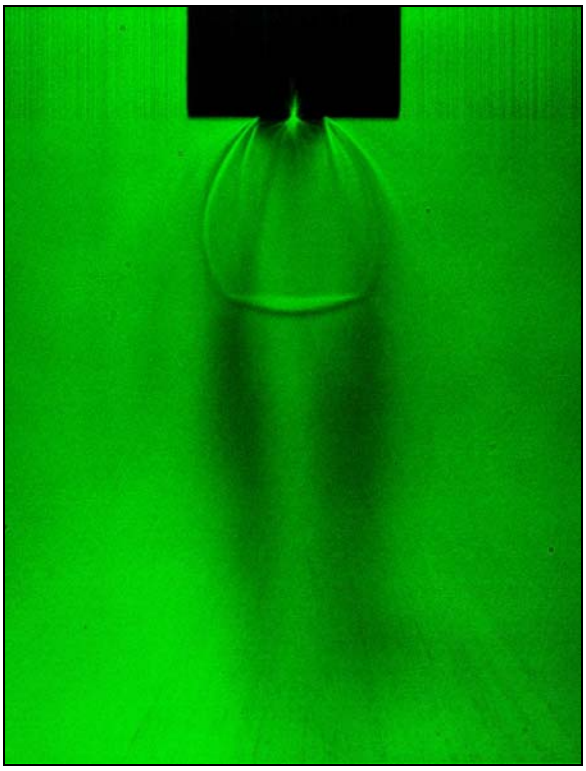

Figure 61. Shadowgraph image, $X_{CH4} = 0.1$, nozzle #9, $d = 0.5$mm, $T_r = 1.01$, $P_r = 1.01$

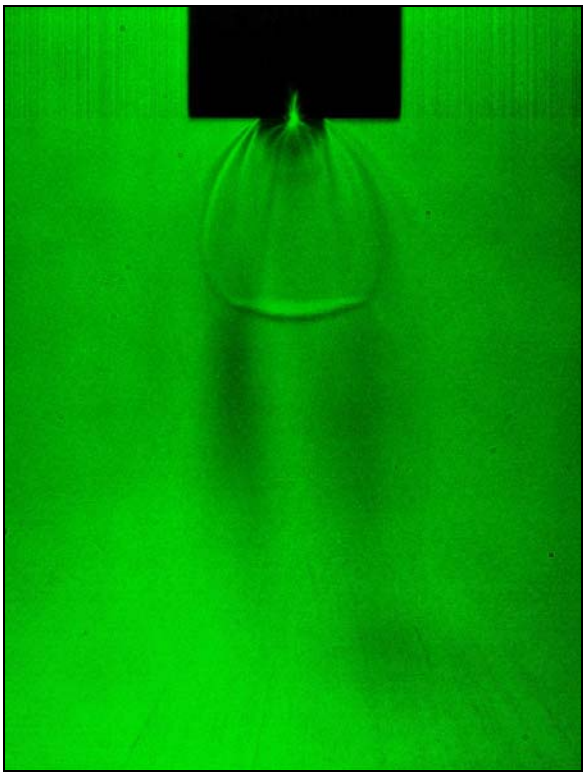

Figure 62. Shadowgraph image, $X_{CH4} = 0.1$, nozzle #9, $d = 0.5$mm, $T_r = 1.03$, $P_r = 1.04$

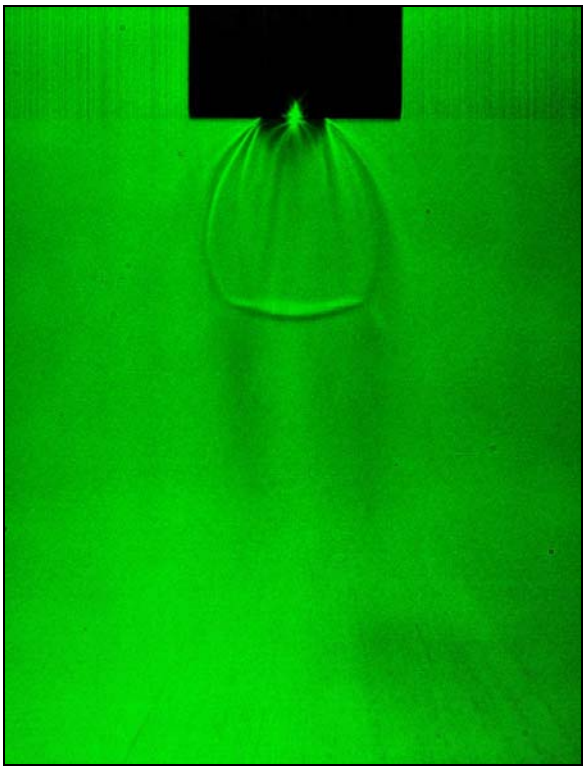

Figure 63. Shadowgraph image, $X_{CH4} = 0.1$, nozzle #7, $d = 0.5$mm, $T_r = 1.04$, $P_r = 1.03$

Raman Scattering Results

Molecular concentration profiles of nitrogen, methane and ethylene at a $z/d = 100$ downstream location are measured using the Raman scattering. Three different fuels are used. Pure ethylene jet species profiles are first compared to the previous study done by Wu et al. [5]. The $X_{CH4} = 0.1$ and 0.2 mixture concentration profiles of different nozzles and injection temperatures will be discussed. Figure 64 shows the overall data processing accuracy. The movement of the laser table is expected to cause some inconsistency between the calibration and injection data. The blue line of Figure 64 is the mole fraction ratio of ethylene to methane determined from the number density of each gas for the certified gas with $X_{CH4} = 0.1$.

The actual methane concentration is 10.378 ± 0.02 of error, thus the expected mole fraction ratio is 8.636 based on the certification document. The averaged mole fraction of data processing is 8.736 ± 0.113. The average value and standard deviation value is calculated from five different pressure cases. This result is proving the data processing method is very accurately performed and both mole fraction ratios agree well with each other. Although the intercept values of the calibration data curve fits are not quite zero, the calibration constants provide accurate and consistent measurement. The $X_{CH4} = 0.1$ mixture fuel data was taken before moving the laser table. Thus, it is necessary to check the mole fraction ratio of the fuel used for the actual Raman signal data.

The red line on Figure 64 is representing the mole fraction ratio of $X_{CH4} = 0.2$ mixture fuel. This fuel is not certified gas. Instead it is manually mixed fuel using the accumulator. Therefore, the accuracy of the methane gas mole fraction is not known.

However, the data results show the mole fraction ratio of ethylene to methane is close to four.

The average mole fraction ratio value is 3.444 ± 0.150. Based on this number, the calculated methane concentration is 22.522%. Those two mixed fuel mole fraction ratio is almost constant along the field of view axis, but the right side of $X_{CH4} = 0.2$ mixture fuel is higher than left side. This slight variation will largely affect to methane mole fraction due to the small amount of methane concentration.

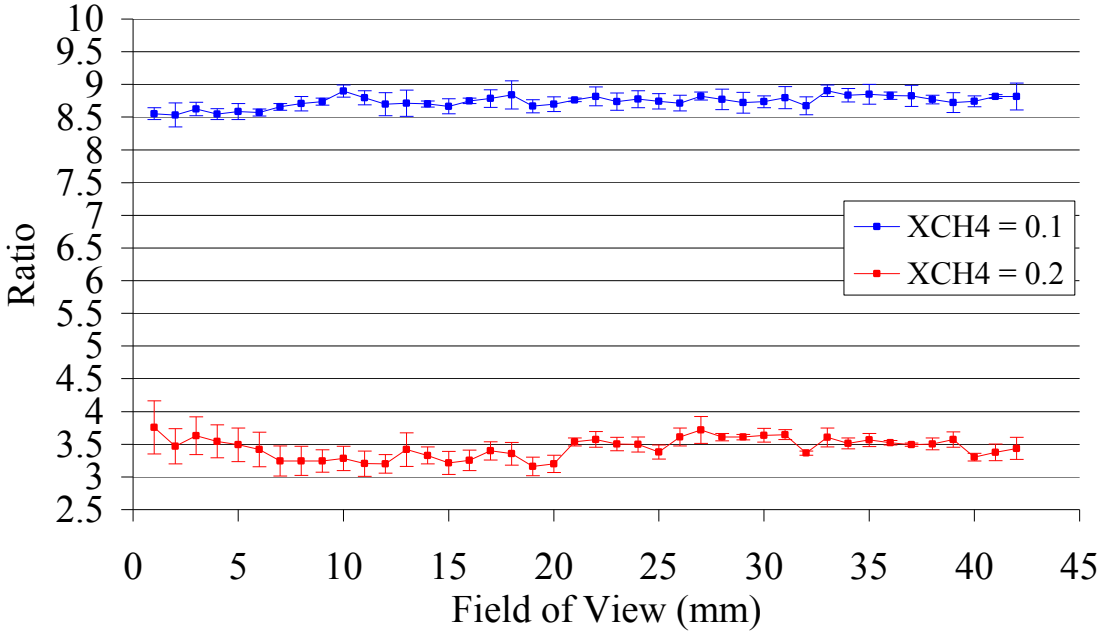

Figure 64. Ethylene to methane mole fraction ratio of $X_{CH4} = 0.1, 0.2$ mixture fuel without injection.

Supercritical Ethylene Fuel Injection.

Figure 65 shows the actual injection condition measured at the nozzle holder. The values are expressed in reduced values showing all conditions in the supercritical region. The pressure ratio of $T_r = 1.00$ is lower than the others simply because the fuel supply pressure was lowered. This is not related to the condensation issue. The pressure ratio of

the injection to the critical pressure is generally maintained constant. In addition, the ratio of the injection pressure to the chamber pressure is also maintained at a constant value, although it is not specifically shown in the figure. The average increase of the chamber pressure is 17Kpa, a small change compared to the injection pressure.

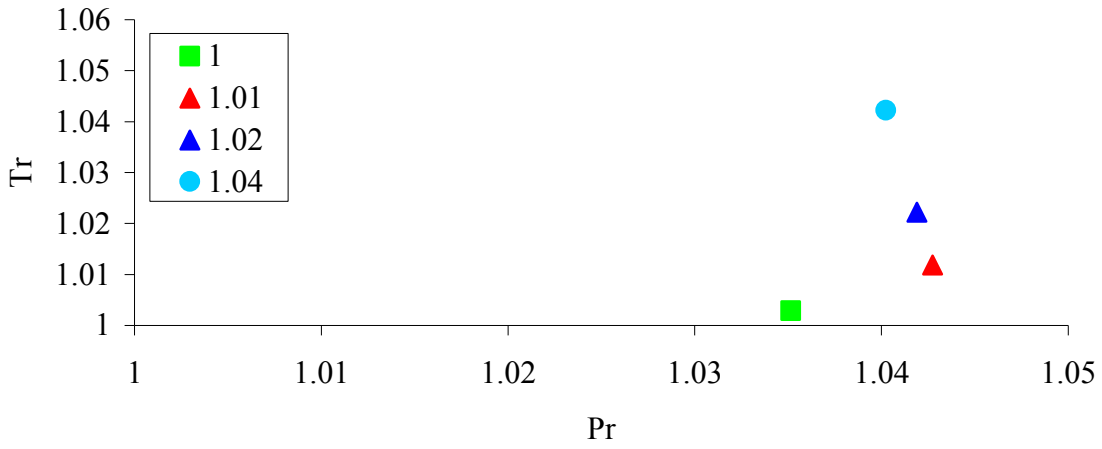

Figure 65. Raman scattering injection conditions, ethylene fuel.

The mole fractions of ethylene and nitrogen are shown in Figure 66 and Figure 69. Ethylene mole fractions shown here are calculated as:

$$X_{C2H4} = \frac{n_{C2H4} - n_{C2H4b}}{n_{C2H4} + n_{CH4} + n_{N2}} \tag{17}$$

where n_{C2H4b} is the ethylene number density accumulated inside the chamber before data collection. Other presented mole fraction values do not subtract the accumulated number density. As an example, the ethylene mole fraction without subtraction is presented in Figure 66. The nitrogen and methane mole fractions are actually calculated as:

$$X_{N2(CH4)} = \frac{n_{N2(CH4)}}{n_{C2H4} + n_{CH4} + n_{N2}} \tag{18}$$

The sum of the species mole fractions are one. The data points of each line represent the average value of three tests for the same condition and the error bar is the standard deviation of them.

As identified in Figure 66, the ethylene centerline mole fraction peak value decreases as the temperature ratio increases from 1.00 to 1.04. Based on the shadowgraph results, a condensed jet is observed close to the critical temperature. The condensation becomes less significant as the injection temperature increases above the critical temperature point. Thus, the higher mole fraction is caused by the fuel condensation process and the condensed jet is not mixed well with the air compared to other jets at higher injection temperature condition.

Previous research measured the jet width at the stoichiometric level of 0.065 and reported the jet width decreased 14mm to 13mm as the injection temperature ratio increases from 1.04 to 1.27 [5]. In this study, the jet width is calculated using full width half maximum (FWHM). The resulting jet width is 11.8mm for $T_r = 1.00$ and 11.9mm for $T_r = 1.04$. The jet width in this study is smaller than previous work done by Wu et al. [5], because the nozzle diameter of previous work is 1mm. Also, the jet width is almost constant value over the different injection temperatures in this study. This could be the result of the narrow temperature rage of this study. The temperature range of the previous study is from 294K to 354K compared to the 282K to 294K for this study. Therefore, the width appears as a constant value for this study.

The jet center value of ethylene mole fraction calculated by Wu et al. [5] at $T_r = 1.04$ is, $X_{CL} = 0.2$, higher than that ($X_{CL} = 0.16$) of 0.5mm diameter nozzle in this study. This difference is because of the different mass flow rate. The mass flow rate reported on

the previous paper was 12.1g/s at that particular temperature condition. The measured mass flow rate is 3.6g/s in this study. The mass flow rate is proportional to nozzle diameter. The bigger nozzle produces larger mass flow rates than the smaller nozzle does.

The ethylene mole fraction is divided by its centerline mole fraction to compare it to Wu et al. [5]. The previous study employs a pseudo-diameter approach to determine centerline mole fraction value and normalize the measured mole fraction to check the self-similar characteristics for the different injection temperature case [5]. But, there is 10% difference between pseudo-diameter centerline mole fraction and measured centerline mole fraction at the temperature close to the critical point. This is caused by condensation. However, the pseudo-diameter centerline mole fraction value agrees well with other temperature conditions where the condensation becomes less [5].

In this study, the ethylene mole fraction is divided by its own centerline mole fraction value without calculating pseudo-diameter centerline mole fraction. The calculation requires additional values not measured for this study (specific heat ratio). The radial ethylene mole fraction profile normalized by the centerline value is shown in Figure 68. All the curves collapse onto a single curve and can be modeled by the best curve fit:

$$\frac{X}{X_{CL}} = \exp\left(-\frac{y^2}{7.2^2}\right) \tag{19}$$

The previous curve fit is also presented on the same Figure 68 showing the jet width is narrower than for this study. Overall, the result agrees well with previous research in terms of mole fraction profile and temperature effects on the mole fraction values, although each value is not quite matched each other.

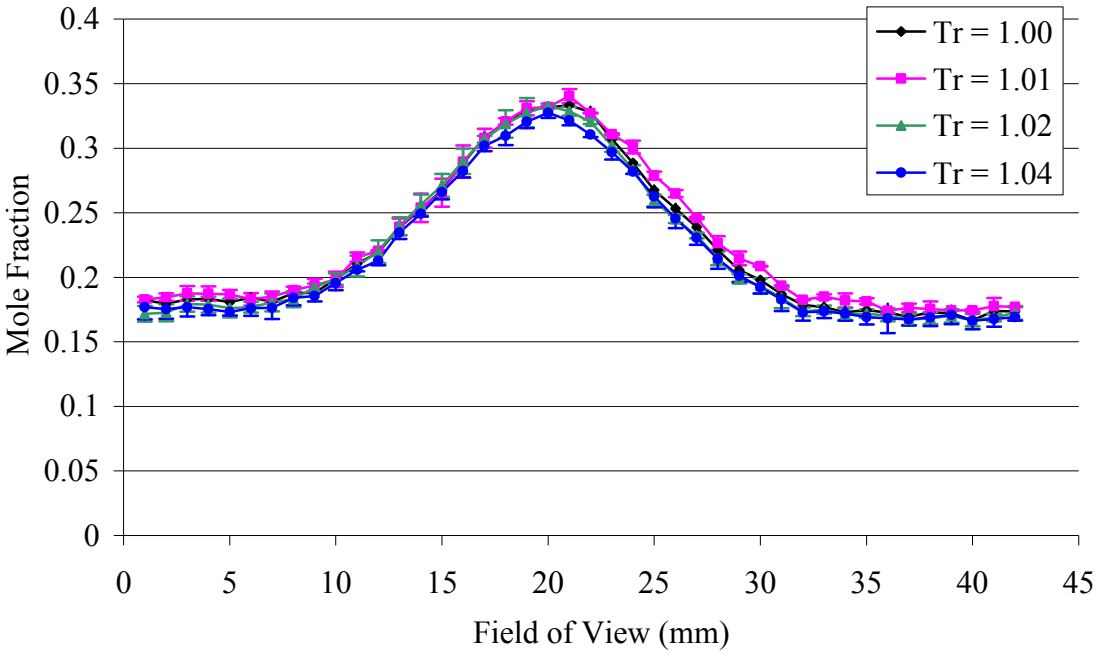

Figure 66. Ethylene mole fraction, ethylene, nozzle #1.

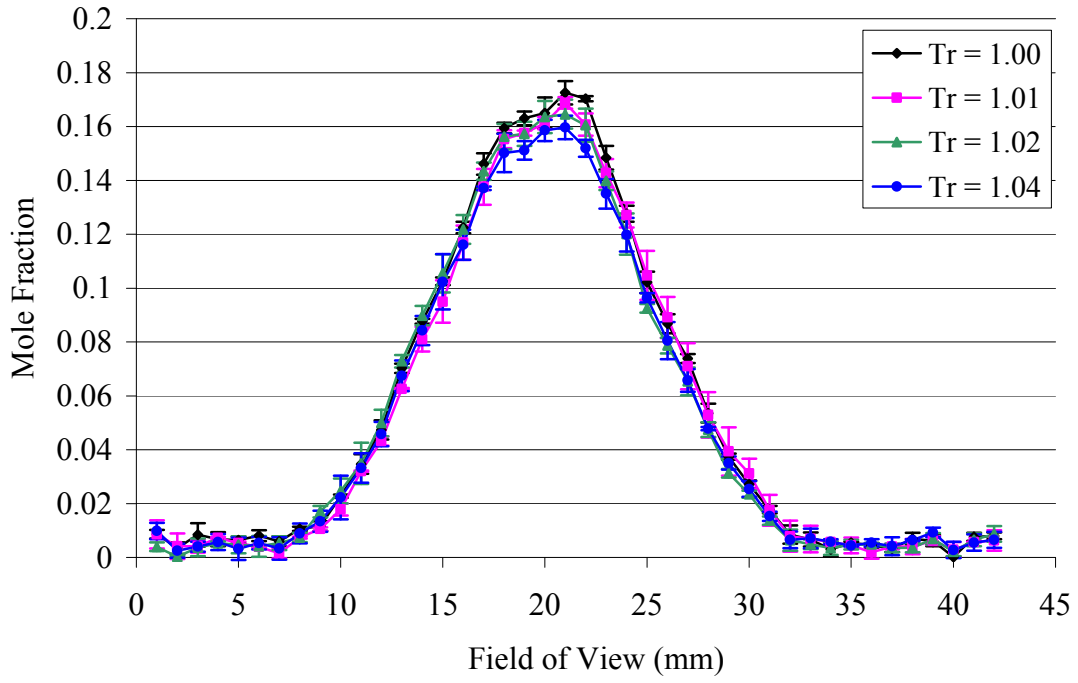

Figure 67. Ethylene mole fraction, ethylene, nozzle #1, without accumulated number density.

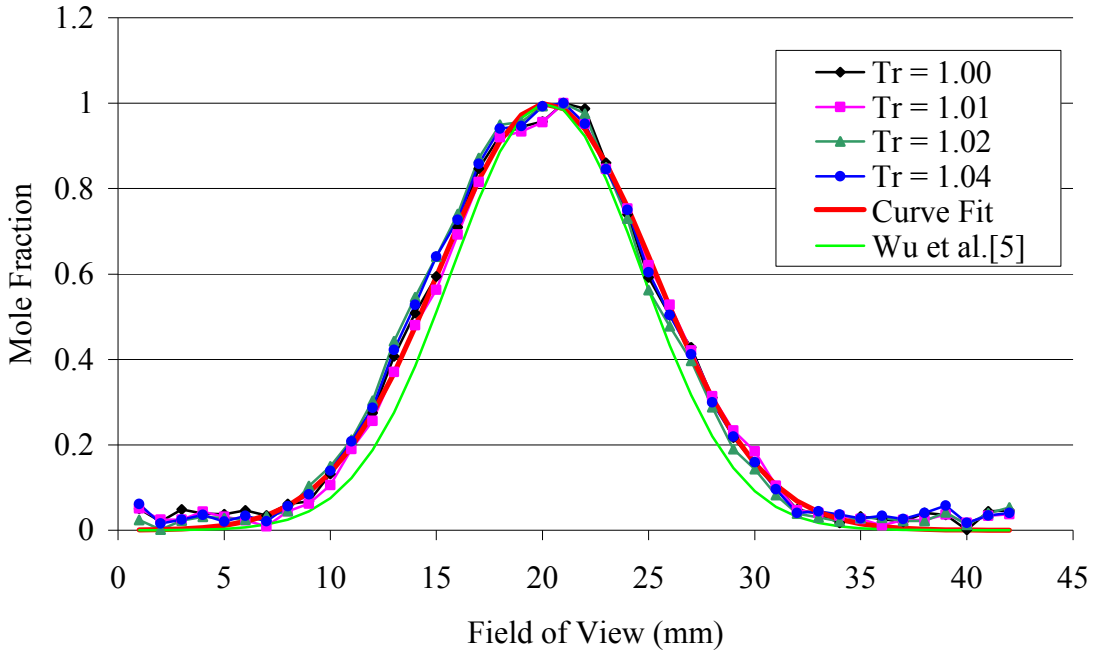

Figure 68. Normalized ethylene mole fraction, ethylene, nozzle #1.

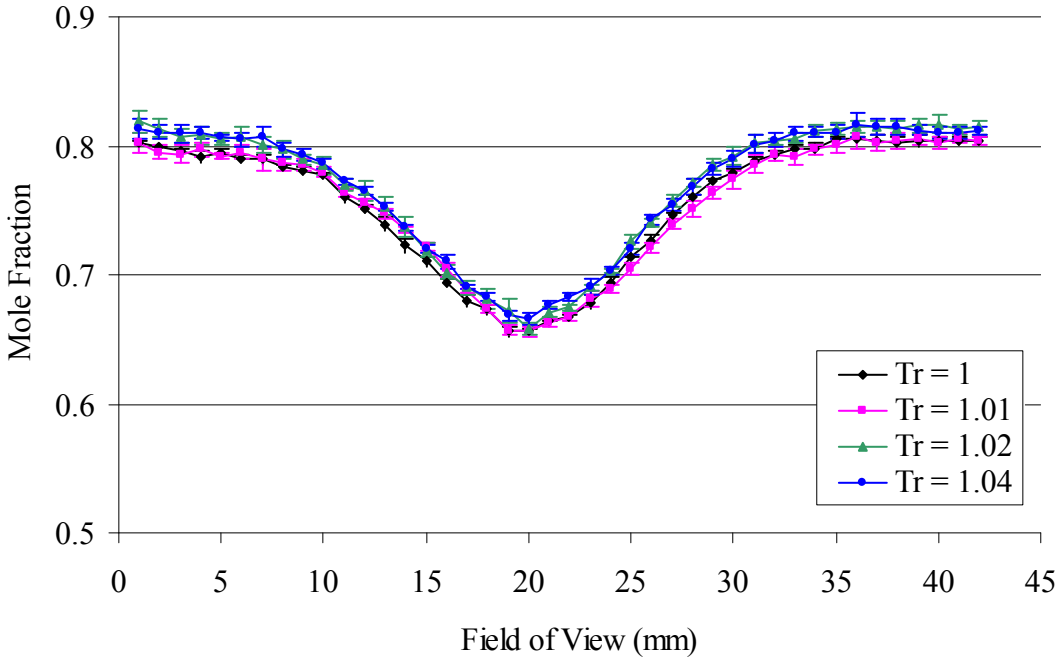

Figure 69. Nitrogen mole fraction, ethylene, nozzle #1.

Supercritical Methane and Ethylene Mixture (X_{CH4} = 0.2) Fuel Injection.

The supercritical X_{CH4} = 0.2 mixture fuel is injected the same way as the previous one. The fuel injection temperature and pressure is adjusted by the critical point value of the fuel according to the methane mole fraction ratio as discussed in chapter II. The chamber pressure is also increased to maintain the same pressure ratio of injection pressure to the chamber pressure as the other fuel cases. However, the injection temperature and pressure ratio value is not changed to maintain consistent ratio values for different fuel injections.

Figure 70 shows the injection conditions of this fuel case, again all the jets are well in the supercritical region. Both temperature ratio and pressure ratio is relatively constant. It is noted the fuel is manually mixed inside the accumulator. The same fuel is used to check the mixing ratio presented in Figure 64. The same data processing method is applied for this case.

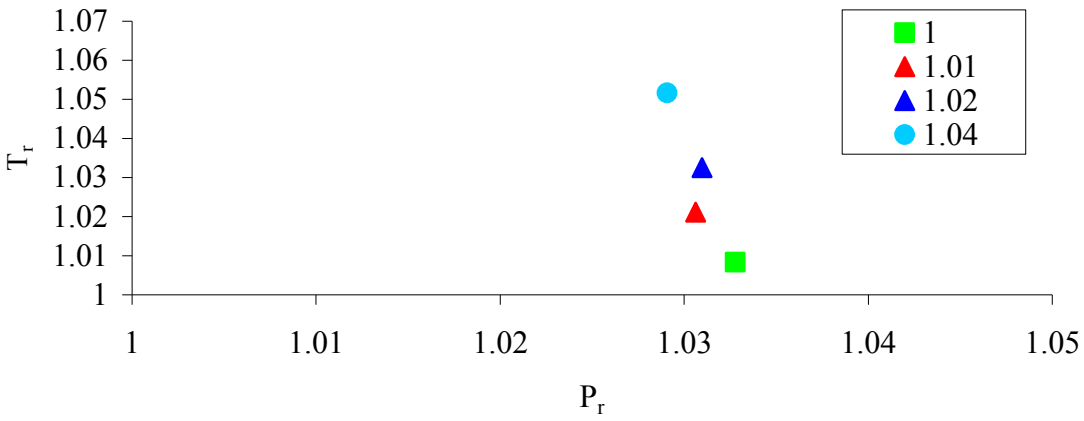

Figure 70. Raman scattering injection conditions, X_{CH4} = 0.2 mixture fuel, nozzle #1.

The ethylene mole fraction at the centerline of the Figure 71 and Figure 72 decreases compared to the previous case. That is also because of the small mass flow rate. The measured average mass flow rate value is 3.08g/s in this case. The condensed jet has the highest value of centerline mole fraction. It mixes relatively poorly mix, slowly spreading out into the nitrogen.

The lower mole fraction indicates better mixing with the nitrogen. Therefore, injection of the condensed jet is less preferred from a fuel mixing perspective. The higher nitrogen mole fraction shows better mixing, and the nitrogen mole fraction of condensed jet has the lowest number. The normalized ethylene mole fraction curve for different injection temperatures also collapses into a single curve. The curve fit denominator is 7.2, slightly smaller than for the ethylene jet.

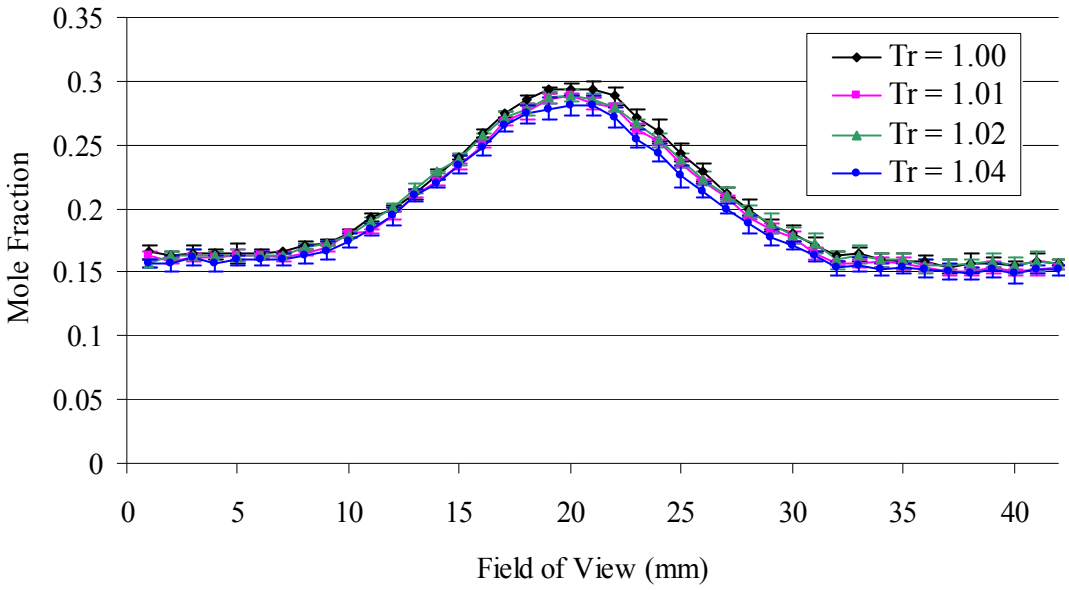

Figure 71. Ethylene mole fraction, $X_{CH4} = 0.2$ mixture, nozzle #1.

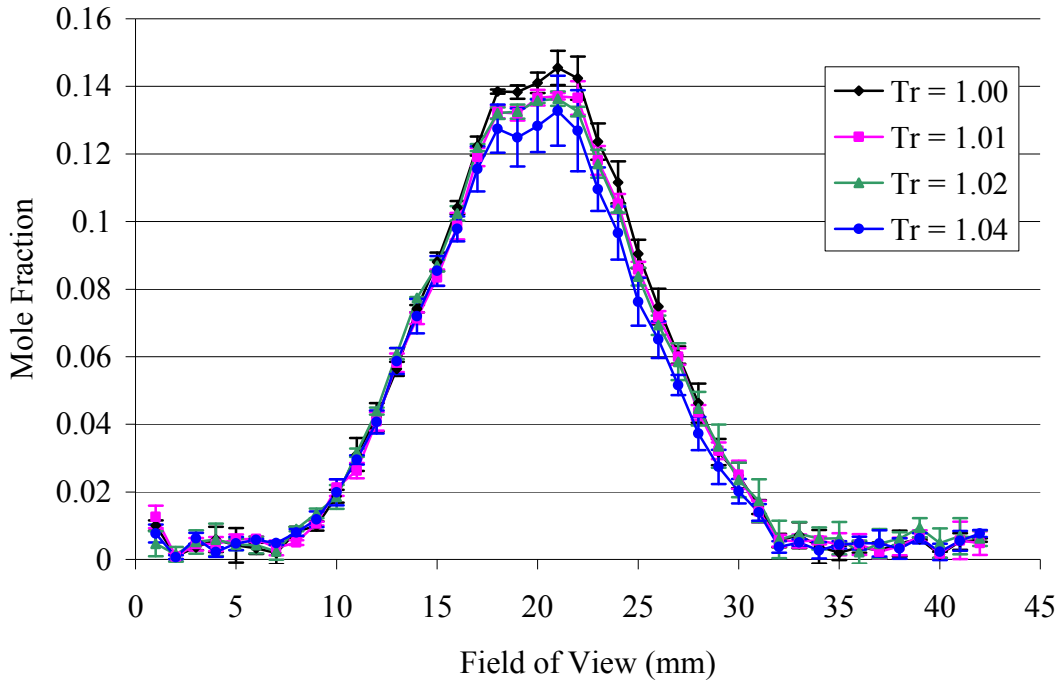

Figure 72. Ethylene mole fraction, $X_{CH4} = 0.2$ mixture, nozzle #1, without accumulated number density.

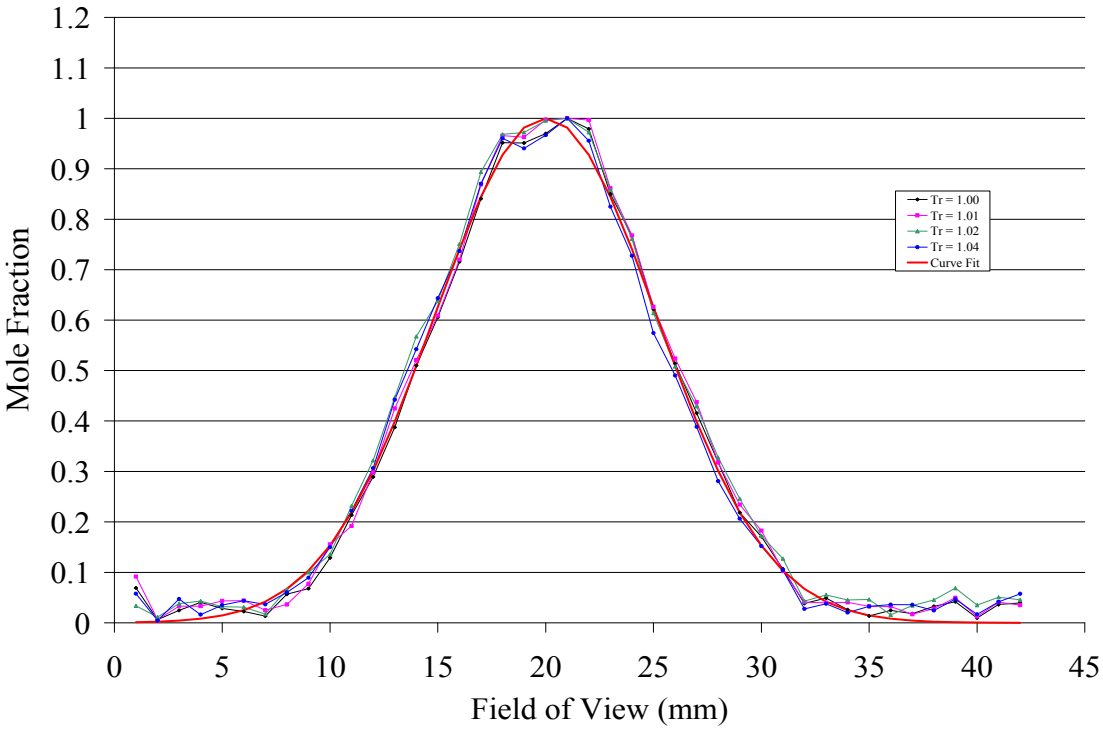

Figure 73. Normalized ethylene mole fraction, $X_{CH4} = 0.2$ mixture, nozzle #1.

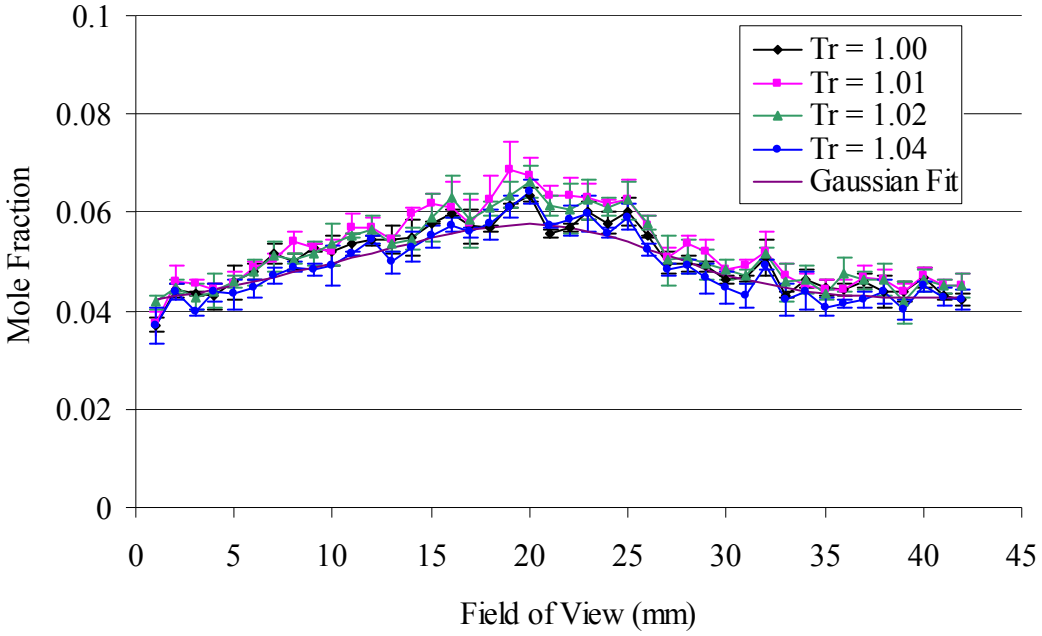

Figure 74. Methane mole fraction, $X_{CH4} = 0.2$ mixture, nozzle #1.

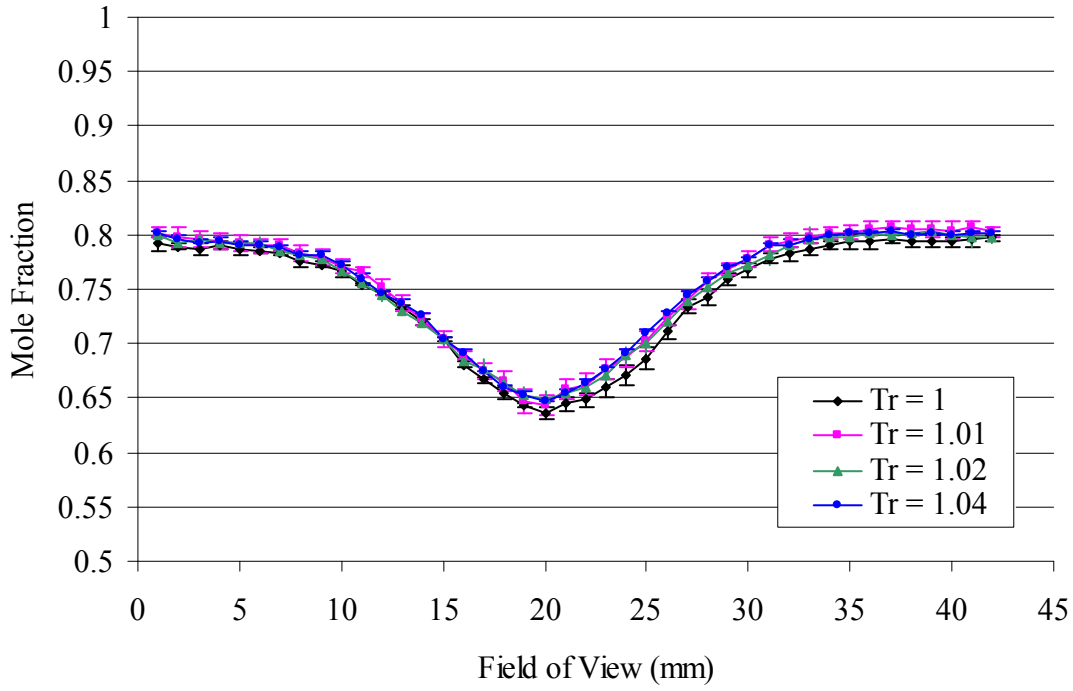

Figure 75. Nitrogen mole fraction, $X_{CH4} = 0.2$ mixture, nozzle #1.

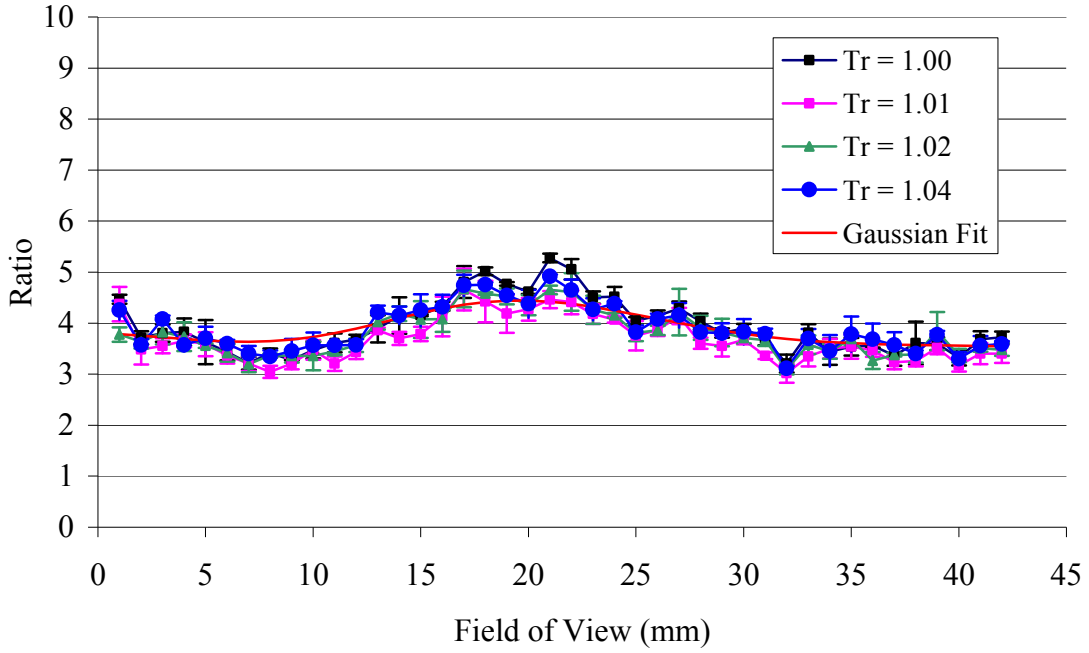

Figure 76. Ethylene to methane mole fraction ratio of $X_{CH4} = 0.2$ mixture fuel, nozzle #1.

The mole fraction ratio of ethylene to methane is shown in Figure 76. The mole fraction ratio of $X_{CH4} = 0.2$ mixture fuel has 3.44 ratio in Figure 64. The centerline mole fraction ratio is higher than its original mixture mole fraction ratio and the ratio is the same as the original mixture mole fraction ratio. It is somewhat inconstant between the two figures.

There are two possible reasons. One is the methane signal is very low compared to ethylene and nitrogen. Thus the methane SNR is a lot lower, particularly at the jet center. It is clearer on the next case with $X_{CH4} = 0.1$ mixture fuel. A small amount of methane at the jet center is causing the higher mole fraction ratio number. So for more accurate mole fraction ratios, the methane mole fraction should be increased when mixing the fuel.

The other possible reason is a turbulent flow effect. At the jet centerline of the nozzle exit plane, only ethylene and methane molecules will be detected with an initial mole fraction ratio, for this case it should be at 4. As it progresses further and further downstream, it is dispersed into the nitrogen environment, and the initial mole fraction ratio is no more maintained, because of two species different dispersion rates. The density of the jet centerline is smaller than of the nozzle exit plane but still higher than the ambient density. Therefore, the molecular mean free path is relatively short and the chance of collision between the ethylene and the methane molecules are high. Although the collision probability between the ethylene molecule themselves are much higher than the ethylene and the methane, the methane molecules can spread out faster than ethylene from the jet centerline. Because the methane kinetic energy is smaller than ethylene, the methane is easily bounced off from the ethylene gas molecule when two molecules collide each other. Once the methane is spread out from the jet center, it is overwhelmed by the turbulent flow. In this region, the gas molecule number density is fairly low and mean free path is long enough to mix well. In addition, the data is taken four seconds after the injection, there are a number of molecules already accumulated and mixed by the turbulent flow. That makes the mole fraction ratio at the jet edge the same as the original mixing ratio.

In short, the methane is spread out faster than the ethylene gas at the jet center. And as it moves to the jet edge it is overwhelmed by the turbulent flow forcing three gases are mixed. The data is taken after the fuel molecules are well mixed and accumulated at the jet edge. Therefore, the centerline mole fraction ratio is higher than at the jet edge.

Supercritical Methane and Ethylene Mixture (X_{CH4} = 0.1) Fuel Injection.

The supercritical $X_{CH4} = 0.1$ mixture of methane and ethylene fuel is injected with the same condition as the previous two cases. Figure 77 is showing the injection condition and the each injection temperature ratio. Again, all the injection conditions are in the supercritical region.

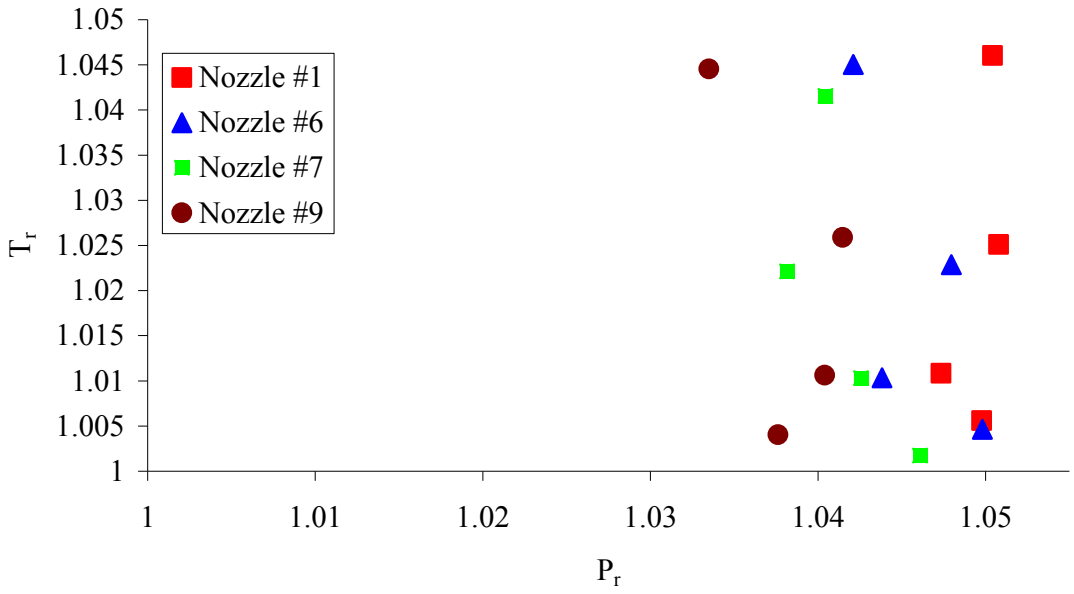

Figure 77. Raman scattering injection conditions, $X_{CH4} = 0.1$ mixture fuel.

This section has a lot more data than the other injection conditions. Four different nozzles are used instead of one. Most of the research objectives will be discussed with these cases. The following figures are arranged in the following order; ethylene mole fractions for different nozzles, ethylene mole fractions for different nozzles without accumulated ethylene number density during data acquisition, normalized ethylene mole fractions, ethylene mole fractions for different injection temperatures for nozzle

comparing purpose, methane and nitrogen mole fractions for different nozzles, ethylene and methane mole fraction ratios for different nozzles.

Ethylene Mole Fractions for Different Nozzles.

Again, the first four ethylene figures represent the ethylene mole fraction without subtracting accumulated number density to capture the total mole fractions of unity adding those of methane and nitrogen together. However, it is necessary to use the mole fraction without accumulated number density to determine the differences between condensed jets and less condensed jets. Generally, the ethylene molecules are still concentrated at the center of the jet at the downstream location shown in Figure 78 through Figure 81. The peak value is located at the jet center for all the different nozzles and injection cases although the values vary over the nozzles.

The condensed jet centerline mole fraction values are always higher than the different nozzles shown in Figure 82 through Figure 85. It demonstrates the ethylene molecules in condensed phase do not spread out fast compared to less condensed jet cases. In other words, the condensed ethylene molecules do not mix well with the nitrogen. That is undesired state from a combustion point of view. The nitrogen mole fractions shown in Figure 100 through 103 are showing the nitrogen mole fraction profile of the condensed jet case has a larger jet width as well as a lower mole fraction value at the centerline. This means the nitrogen number density at the condensed jet centerline is lower than others. A small number of nitrogen molecule presence means less mixing. Therefore, the condensed phase of an ethylene jet is affecting mixing rate and is not a desirable state inside the combustor. In addition, the ethylene mole fraction profile shape

is somewhat different depending on each nozzle, detailed discussion will be in the nozzle comparison section.

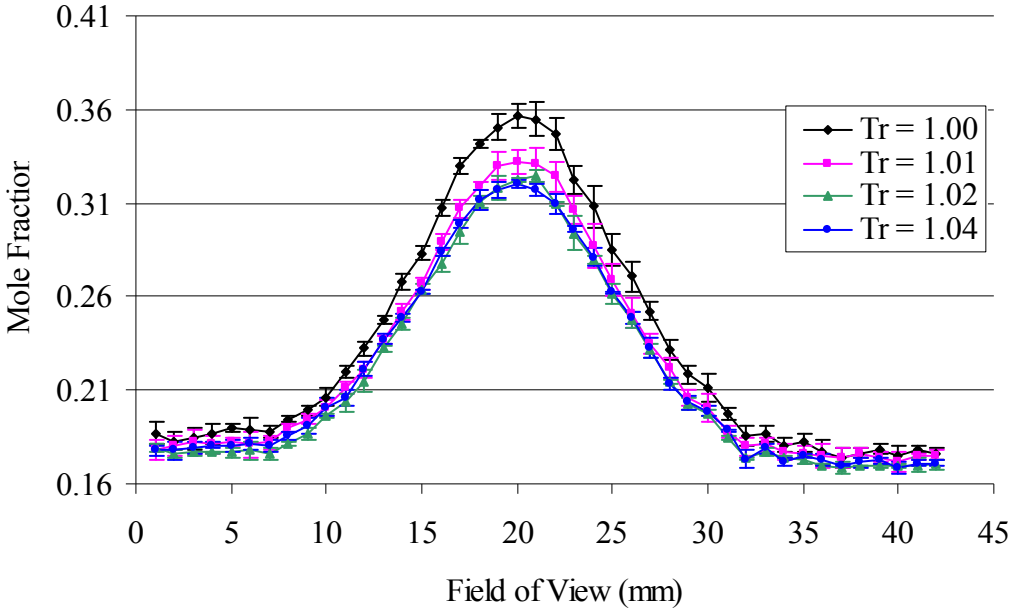

Figure 78. Ethylene mole fraction, X_{CH4} = 0.1 mixture, nozzle #1.

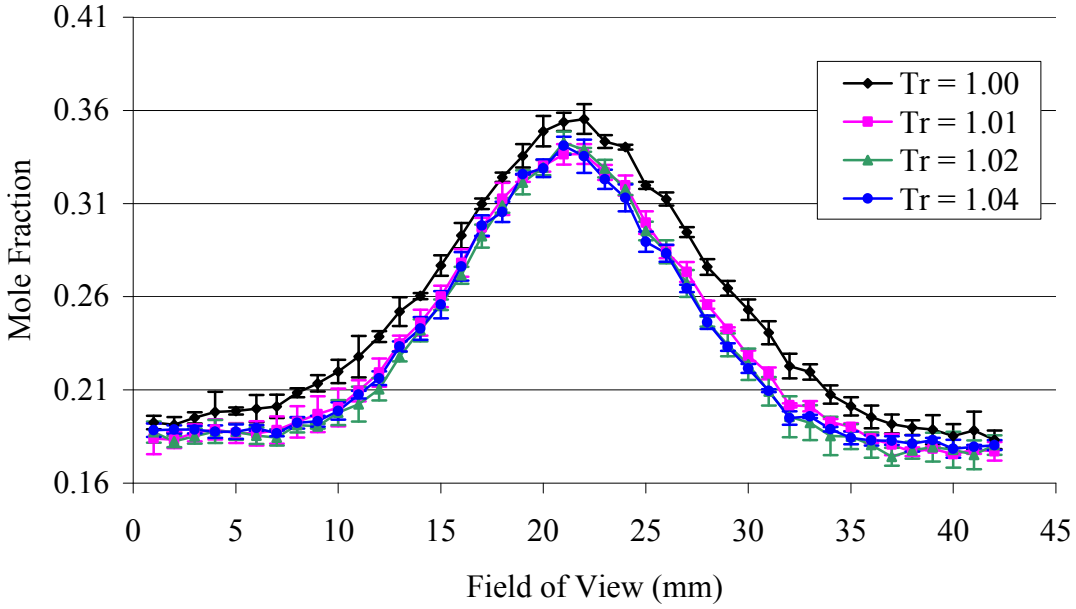

Figure 79. Ethylene mole fraction, X_{CH4} = 0.1 mixture, nozzle #6.

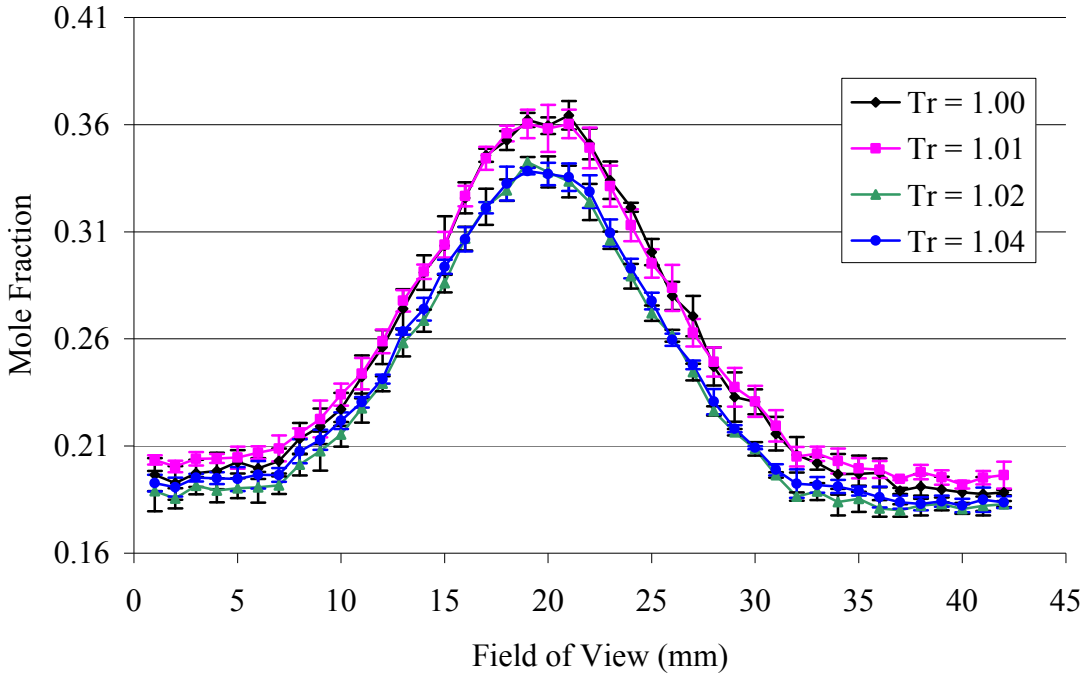

Figure 80. Ethylene mole fraction, X_{CH4} = 0.1 mixture, nozzle #7.

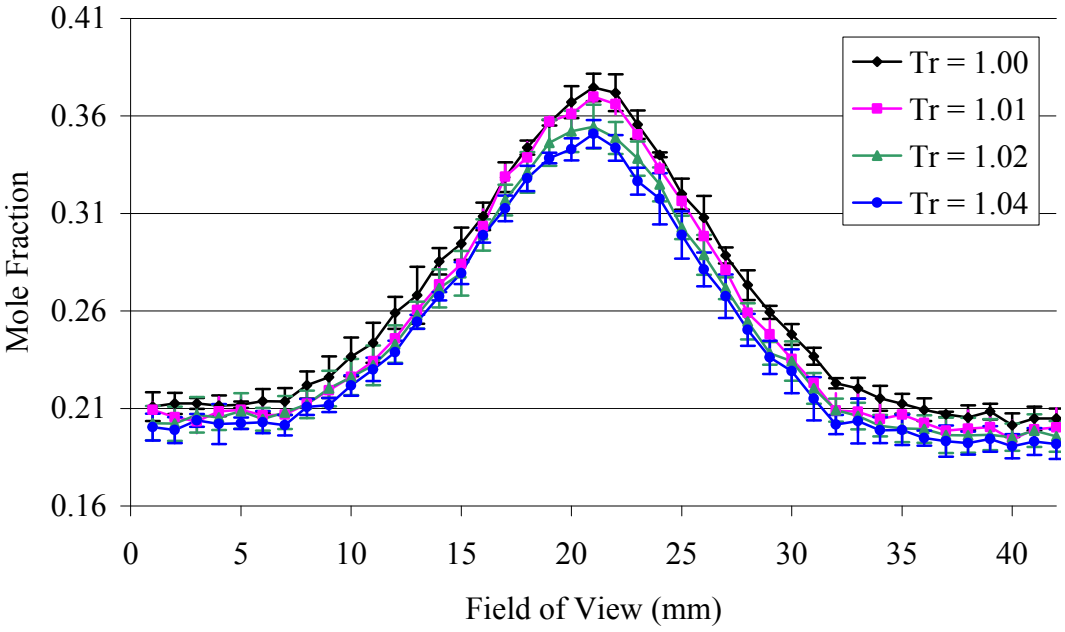

Figure 81. Ethylene mole fraction, X_{CH4} = 0.1 mixture, nozzle #9.

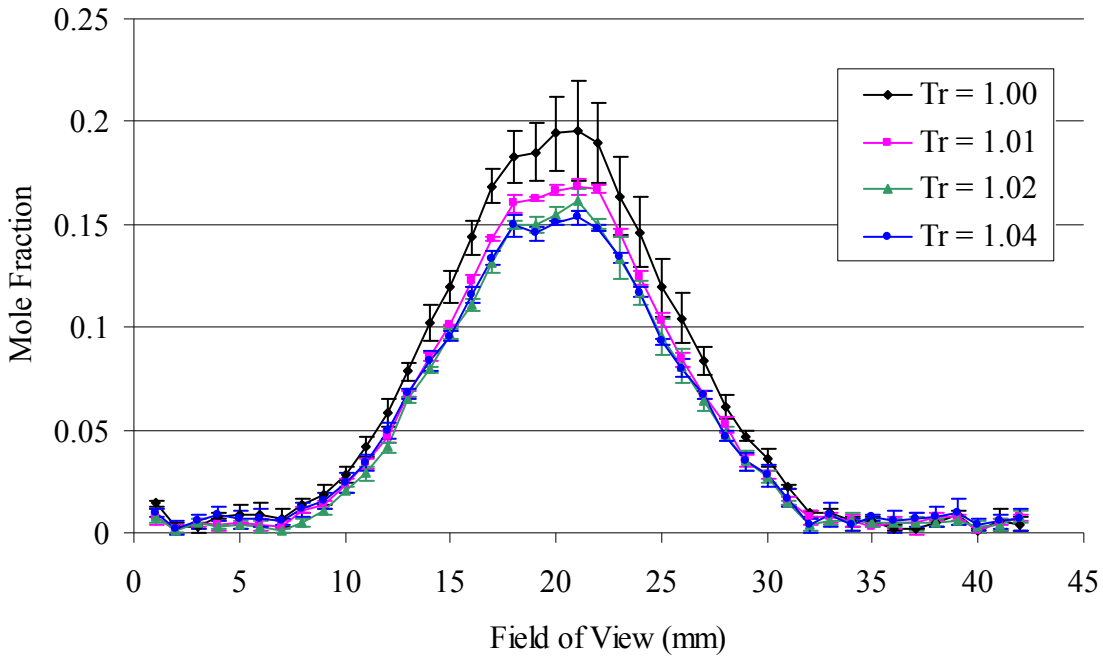

Figure 82. Ethylene mole fraction, X_{CH4} = 0.1 mixture, nozzle #1, without accumulated number density.

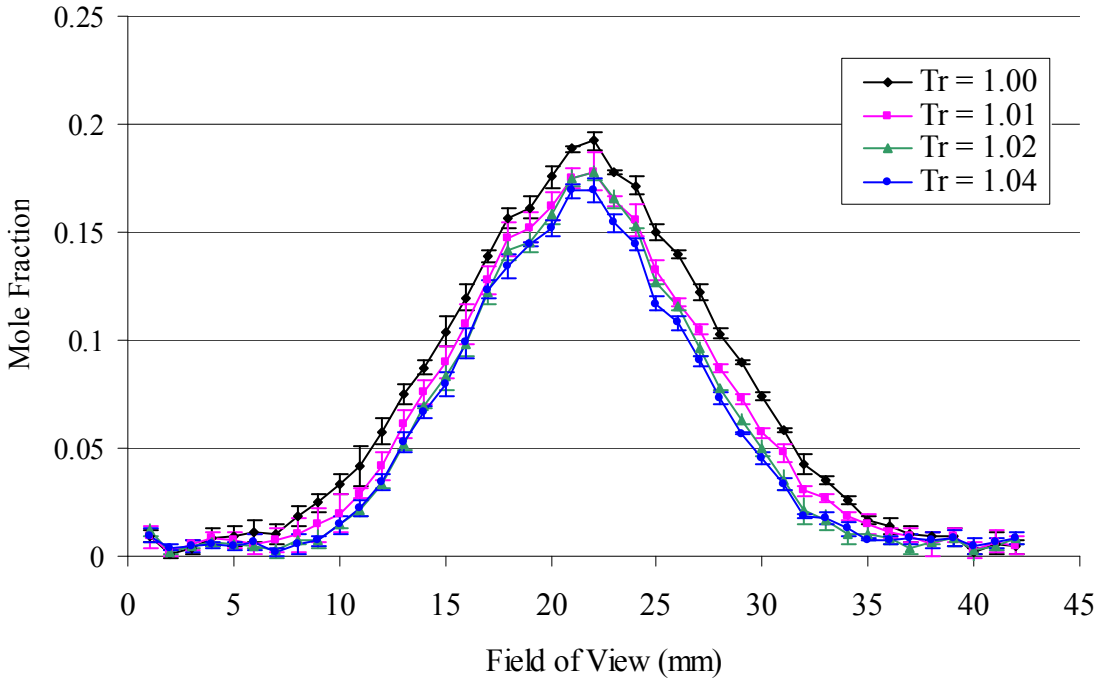

Figure 83. Ethylene mole fraction, X_{CH4} = 0.1 mixture, nozzle #6, without accumulated number density.

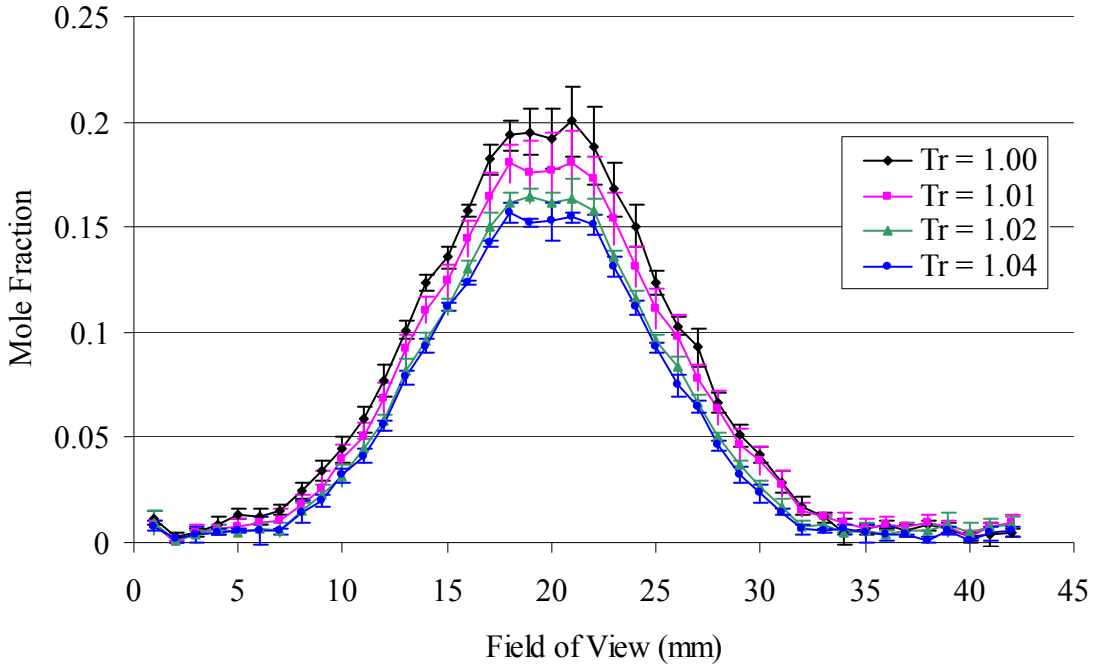

Figure 84. Ethylene mole fraction, X_{CH4} = 0.1 mixture, nozzle #7, without accumulated number density.

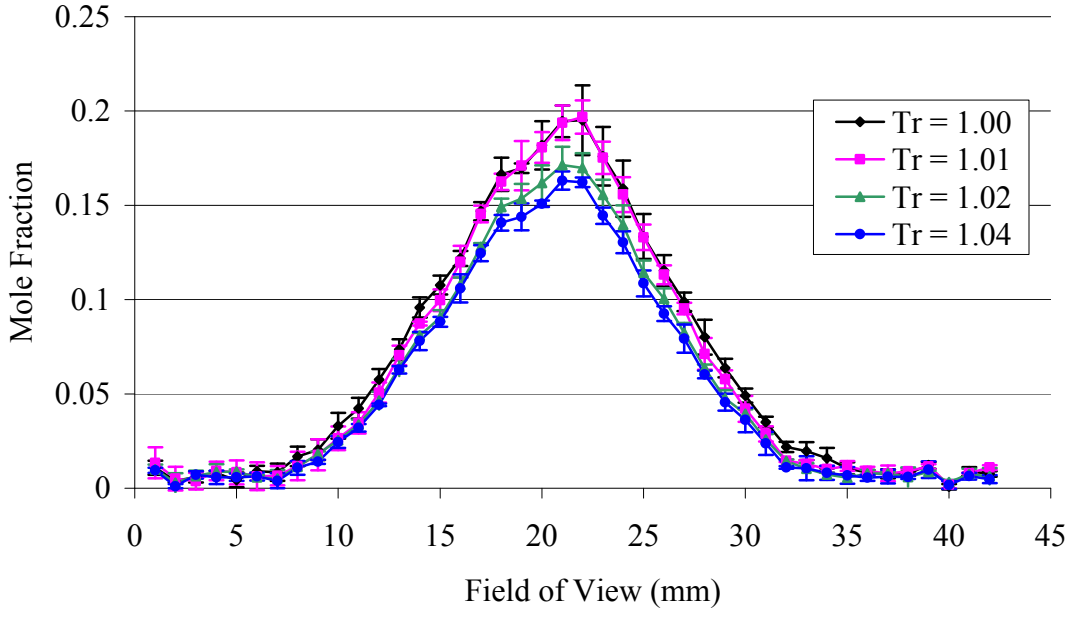

Figure 85. Ethylene mole fraction, X_{CH4} = 0.1 mixture, nozzle #9, without accumulated number density.

Normalized Ethylene Mole Fractions.

Next four figures are presenting normalized ethylene mole fractions divided by their own peak centerline value. Every mole fraction curve collapses onto almost one single curve for the same nozzle. The red line is the best curve fit and the relation is developed by Wu et al. [5]. The curve fit relation is also presented on equation 19. Since the jet width is different over the nozzles the denominator constant is varied in accordance with jet width. Table 5 is showing the denominator constant value of each nozzle as well as the best curve fit range. Large denominator indicates wide jet width.

Table 5. Best curve fit constants.

	Nozzle #1	Nozzle #6	Nozzle #7	Nozzle #9	Wu et al.
Denaminator	7.4	7.8	7.8	7.3	6.34
Best fit range	> 0.03	> 0.03	> 0.03	> 0.04	> 0.03

The ethylene jets of nozzle #6 and #7 have the widest dispersion profiles and spreading fast in the radial directions. Based on this parameter, nozzle #6 and #7 are better nozzles because these nozzles are spreading the fuel in the radial direction wider than others for better mixing with the nitrogen at the same concentration value. The best curve fit range is greater than 0.03 which is the same range to the previous work done by Wu et al. [5].

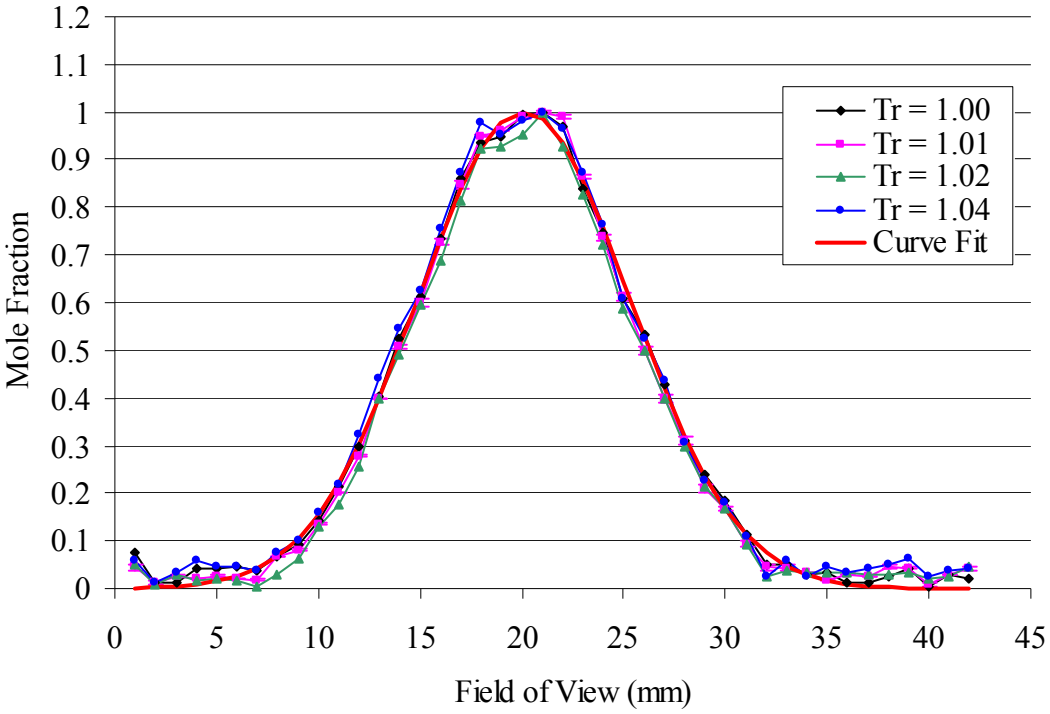

Figure 86. Normalized ethylene mole fraction, X_{CH4} = 0.1 mixture, nozzle #1.

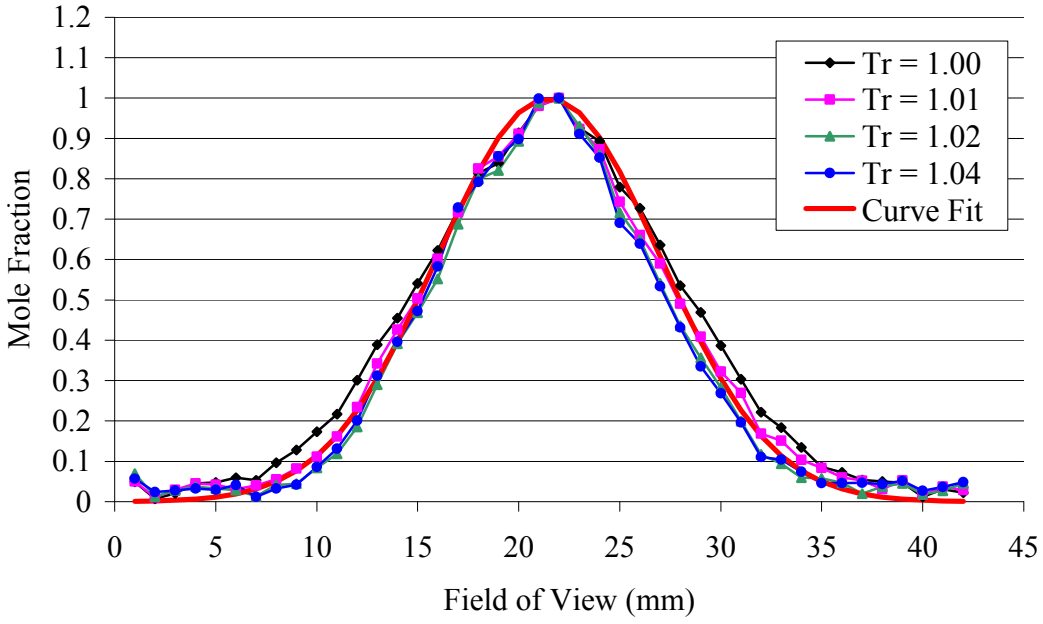

Figure 87. Normalized ethylene mole fraction, X_{CH4} = 0.1 mixture, nozzle #6.

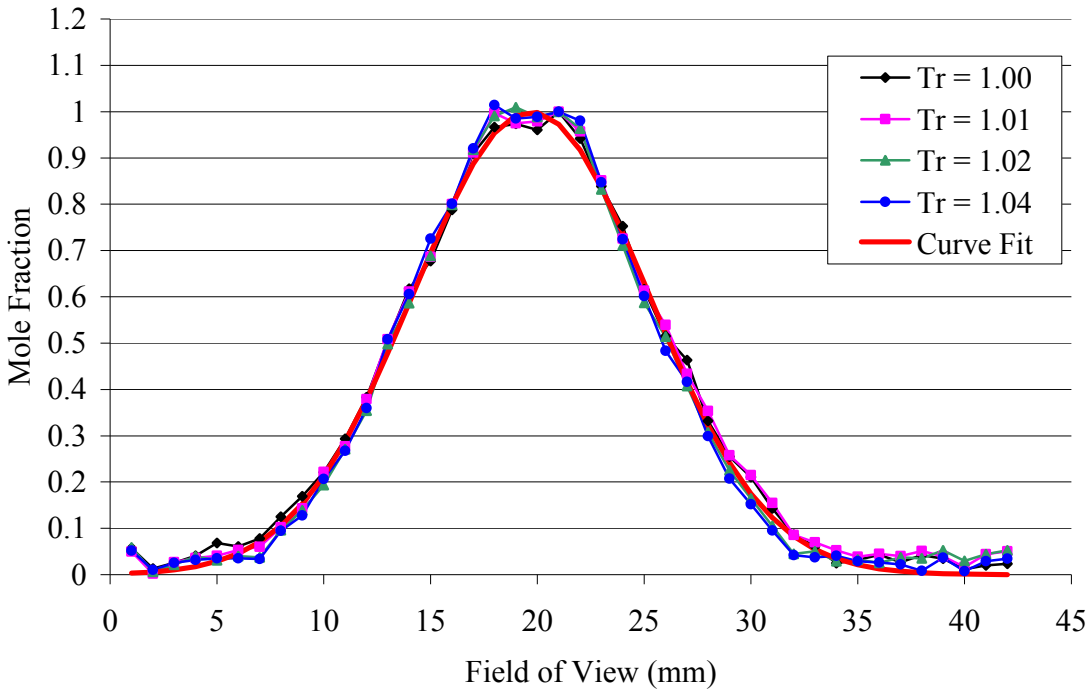

Figure 88. Normalized ethylene mole fraction, X_{CH4} = 0.1 mixture, nozzle #7.

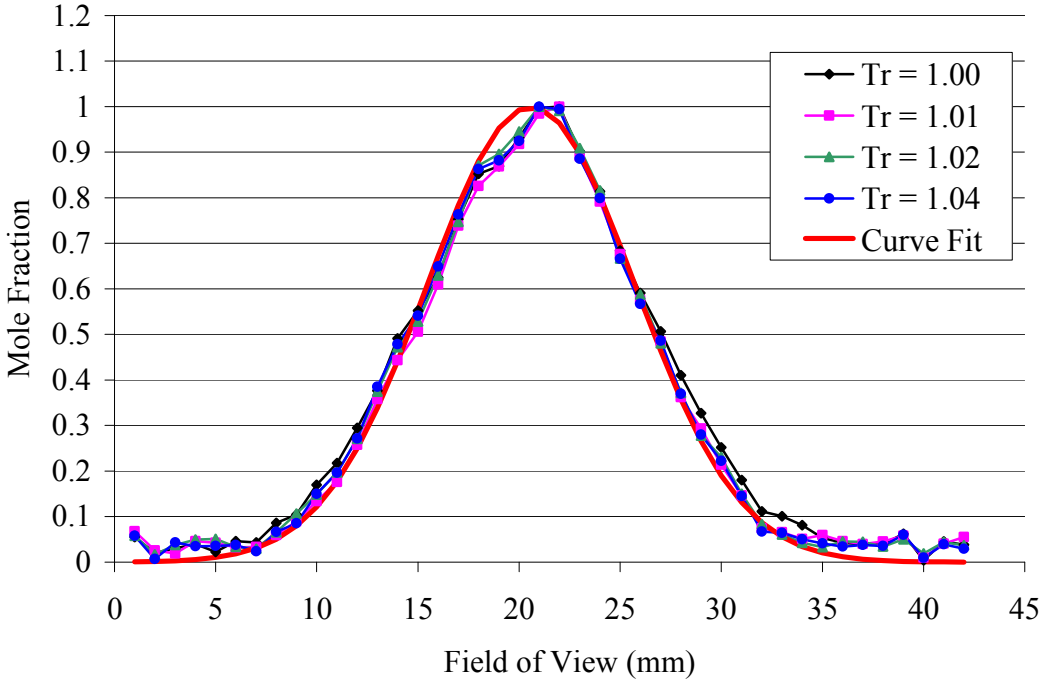

Figure 89. Normalized ethylene mole fraction, X_{CH4} = 0.1 mixture, nozzle #9.

Ethylene Mole Fractions for Different Injection Temperatures.

Ethylene mole fractions over different injection temperatures are shown in Figure 90 through 93 to identify whether there is any particularly outstanding performance nozzle or not. After changing the nozzle, the laser table is moved along the *y*-direction to find the new jet center. The ethylene mole fraction profiles over the different nozzles are little bit off to each other for this reason. The centerline mole fraction value is almost the same but nozzle #7 has centerline peak value over little wider range of jet center. Nozzle #1 is performing better nozzle based on the results shown in Figure 91, 92 and 93 in terms of jet centerline mole fraction value. Figure 94 shows centerline ethylene mole fraction values for each nozzle. It is clear ethylene centerline mole fraction value of nozzle #1 has the lowest value among four nozzles. This indicates the ethylene molecules of nozzle #1 are spreading out faster than others and mixing well with nitrogen, although nozzle #6 has the lowest value at $T_r = 1.00$. However the ethylene mole fraction value of nozzle #6 has the highest value as the injection temperature increases.

Another important parameter of comparing nozzle performance is a jet width. Figure 95 shows the jet widths determined by FWHM method. Generally, nozzle #7 shows better mixing except for $T_r = 1.00$. Nozzle #6 shows outstanding performance at $T_r = 1.00$ but rapidly decreases as the injection temperature increases until $T_r = 1.02$. Nozzle #1 shows the smallest jet width value which is not spreading well in the radial direction. Nozzle #9 increases as the injection temperature increases. It needs to compare over wide injection temperature range to identify individual nozzle's jet width trends more accurately. For this reason, centerline mole fraction value is the parameter used to compare each nozzle's performance in this study.

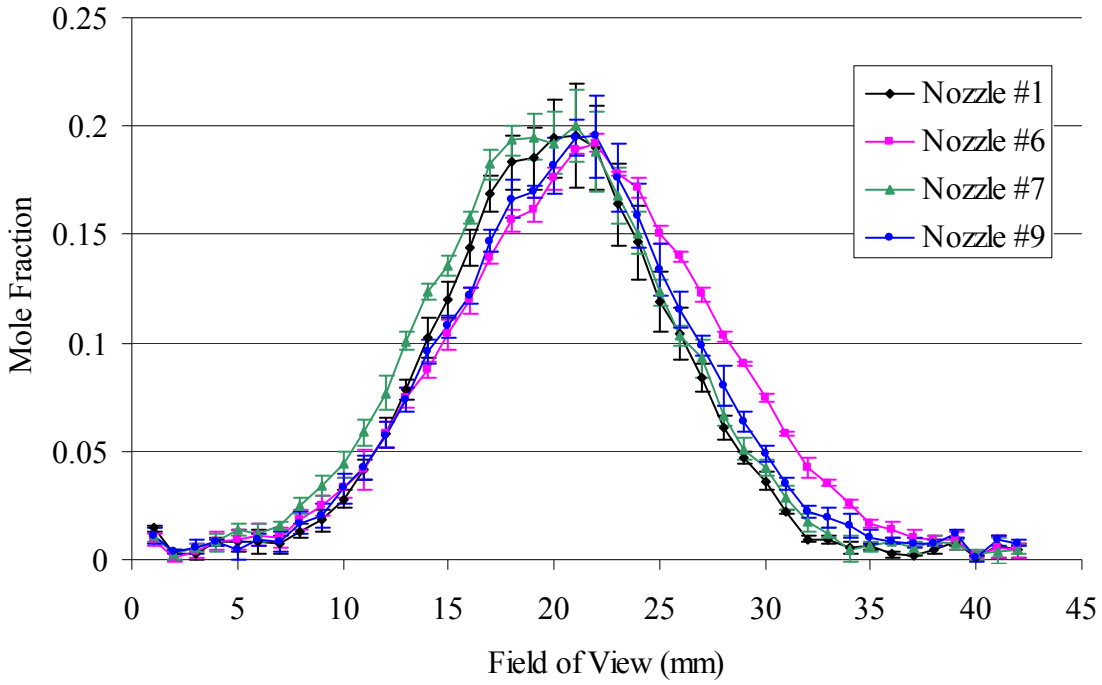

Figure 90. Ethylene mole fraction, X_{CH4} = 0.1 mixture, T_r = 1.00, without accumulated number density.

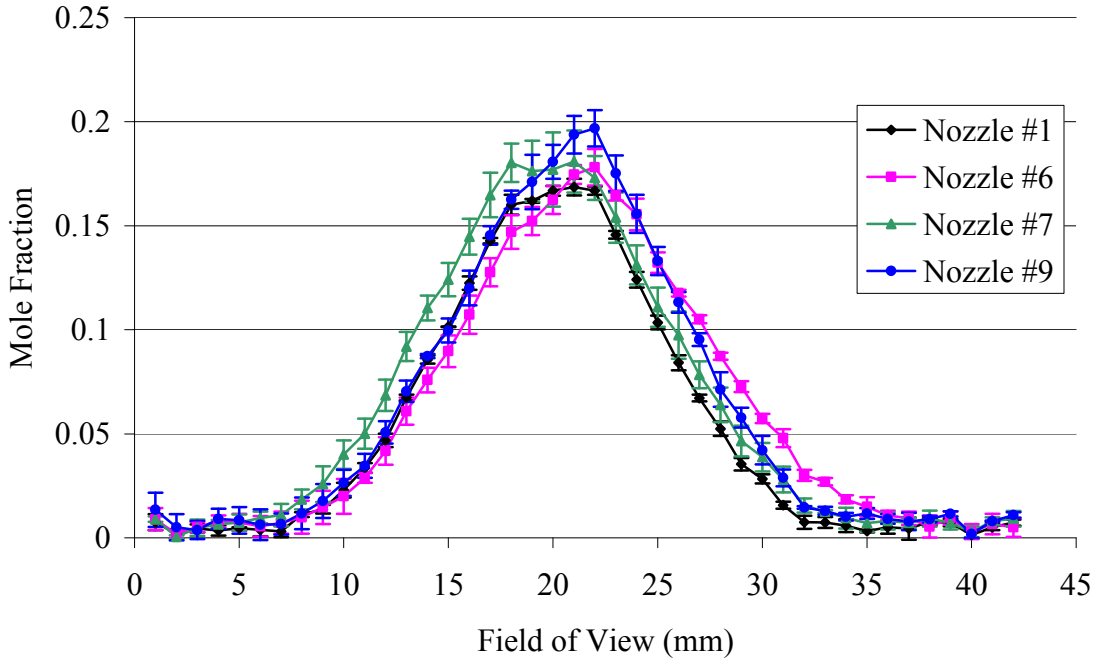

Figure 91. Ethylene mole fraction, X_{CH4} = 0.1 mixture, T_r = 1.01, without accumulated number density.

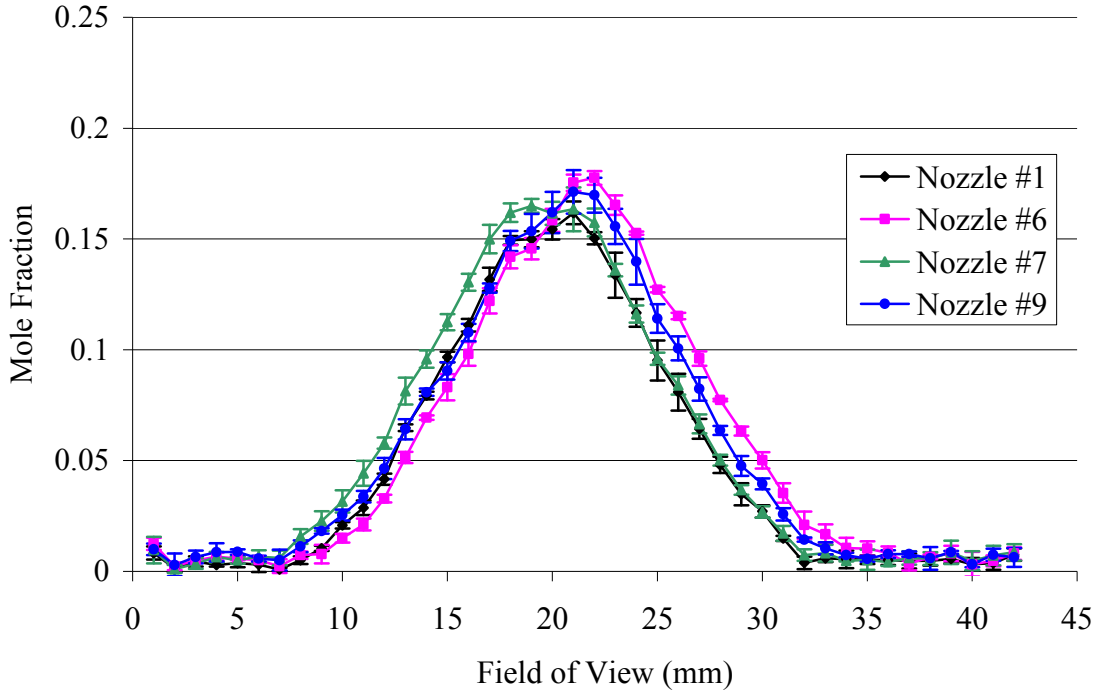

Figure 92. Ethylene mole fraction, X_{CH4}=0.1 mixture, T_r = 1.02, without accumulated number density.

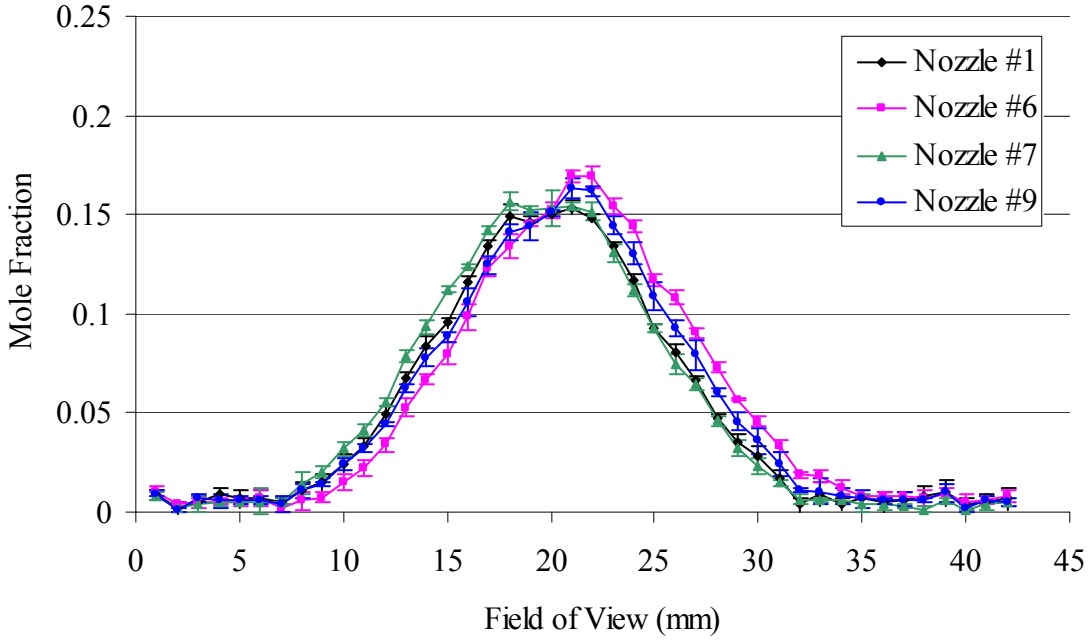

Figure 93. Ethylene mole fraction, X_{CH4}=0.1 mixture, T_r = 1.04, without accumulated number density.

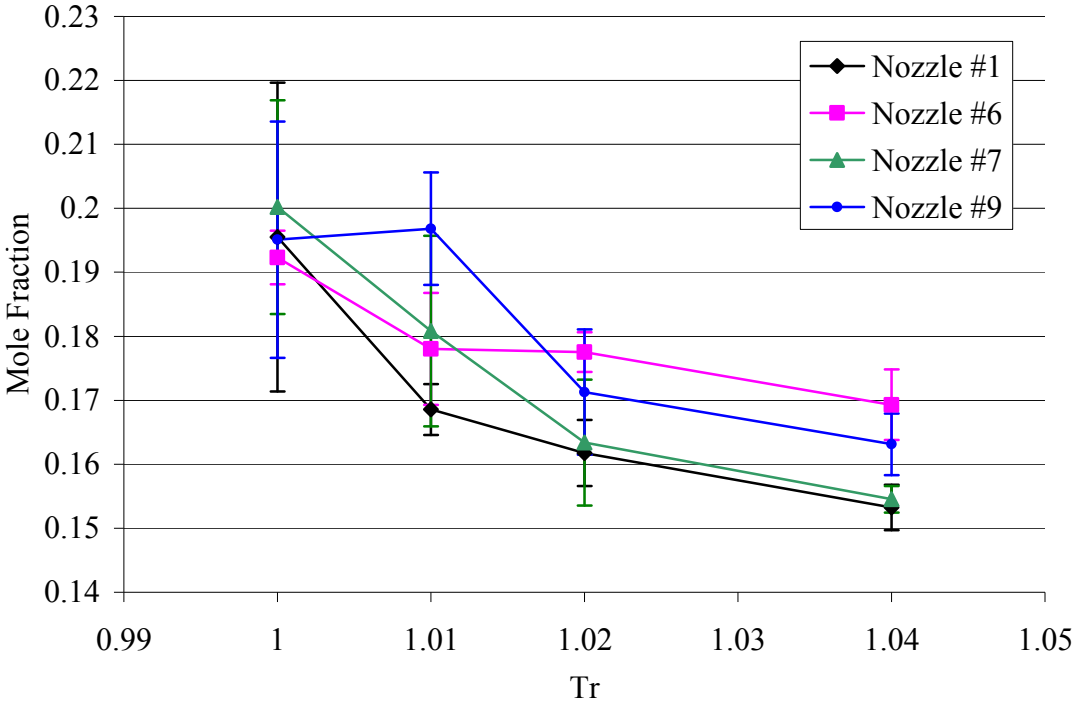

Figure 94. Ethylene centerline mole fraction values for different nozzles.

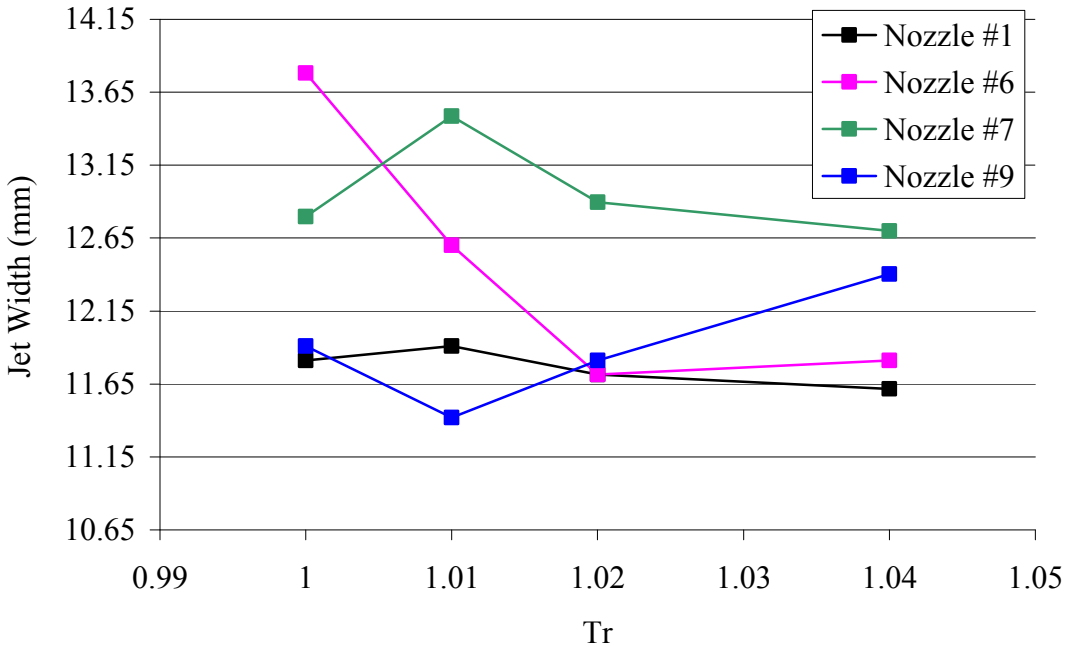

Figure 95. Ethylene jet widths for different nozzles.

Methane Mole Fractions for Different Nozzles.

Methane mole fraction profiles are presented for the next four figures, Figure 96 through Figure 99. The Gaussian curve fit of $T_r = 1.04$ case is also presented on each figure to show the general pattern. The left side mole fraction value is higher than the right side. That is caused by the calibration inaccuracy. As mentioned earlier, there is difference associated with calibration data shown in Figure 64. Due to the small methane concentration in the fuel compare to that of ethylene, the methane signal is easily overwhelmed by even small signal noise.

In spite of low SNR, the profiles are consistent over different nozzles and injection conditions. The mole fraction profile of condensed jet is distinctively above from other cases which are also less desirable condition from the fuel mixing point of view. As the injection temperature increases, the general pattern of mole fraction value converges into one line as shown in Figure 99 except for $T_r = 1.00$. More importantly, the mole fraction profile presented here for $X_{CH4} = 0.1$ mixture fuel has a different pattern comparing to that of $X_{CH4} = 0.2$ mixture fuel. There is methane concentration at the jet center of $X_{CH4} = 0.2$ mixture fuel. It is possible certain amount of methane molecules are dispersing faster, and the rest of the methane molecules are remained at the jet center. Furthermore, methane molecules are not condensed while ethylene molecules are condensed. Because methane critical temperature is much lower than that of mixture fuel. Thus it may not be in condensed phase letting methane disperses fast from the jet center. Also, it is relatively light gas molecule comparing to ethylene that could spread out quickly. And once it is dispersed to the jet edge, it is overwhelmed by turbulent flow for mixing with nitrogen.

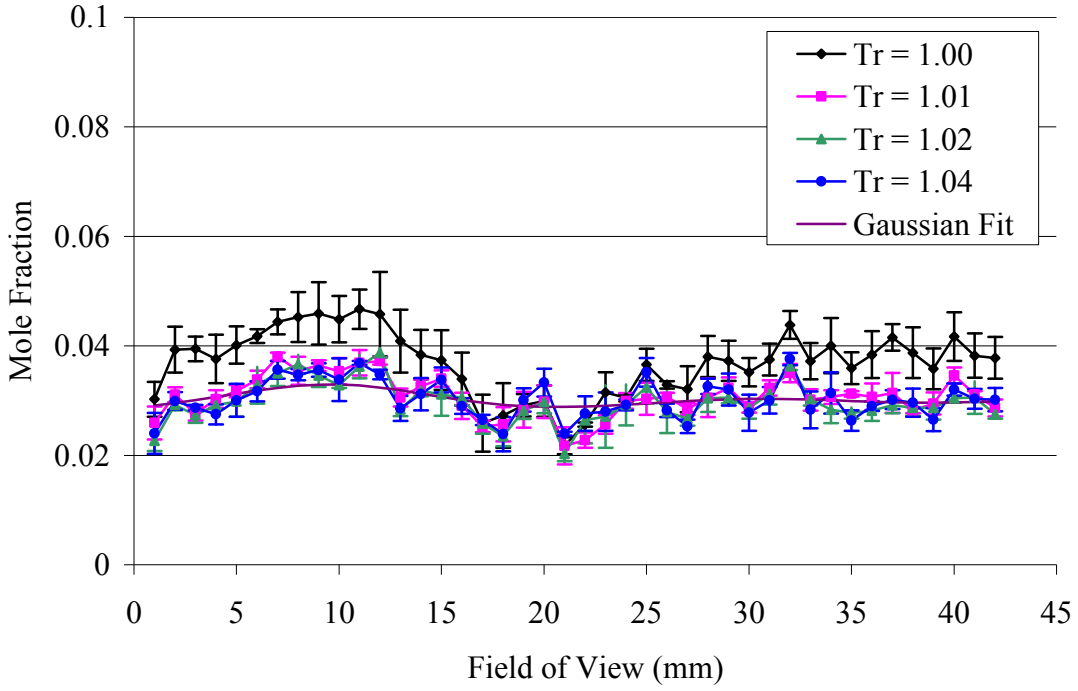

Figure 96. Methane mole fraction, X_{CH4} = 0.1 mixture, nozzle #1.

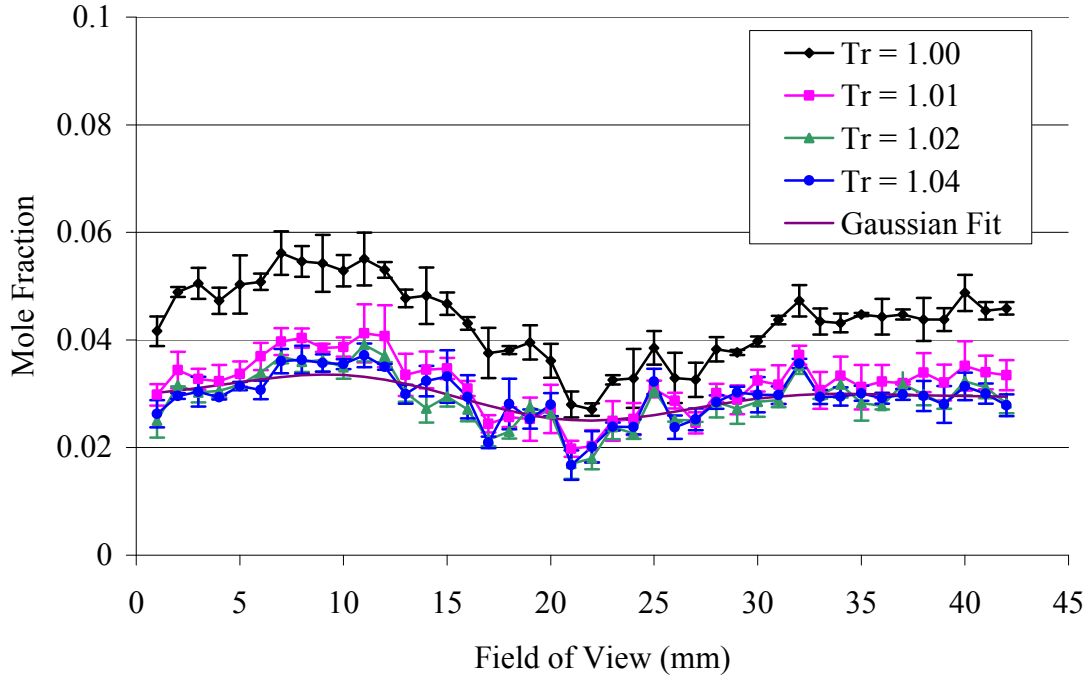

Figure 97. Methane mole fraction, X_{CH4} = 0.1 mixture, nozzle #6.

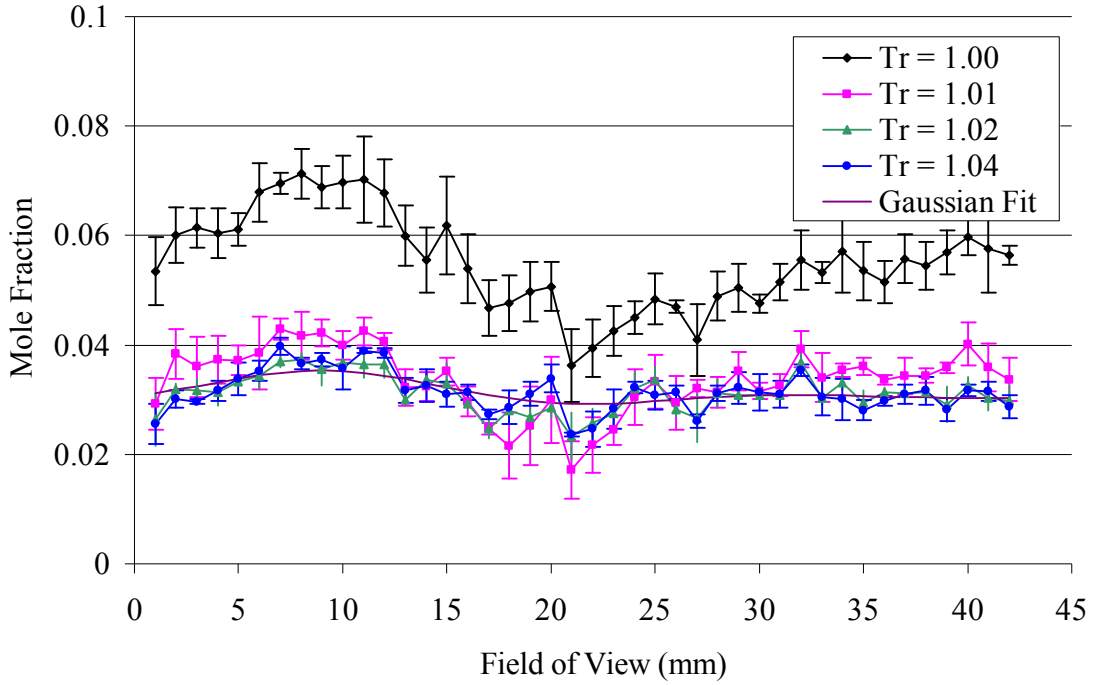

Figure 98. Methane mole fraction, X_{CH4} = 0.1 mixture, nozzle #7.

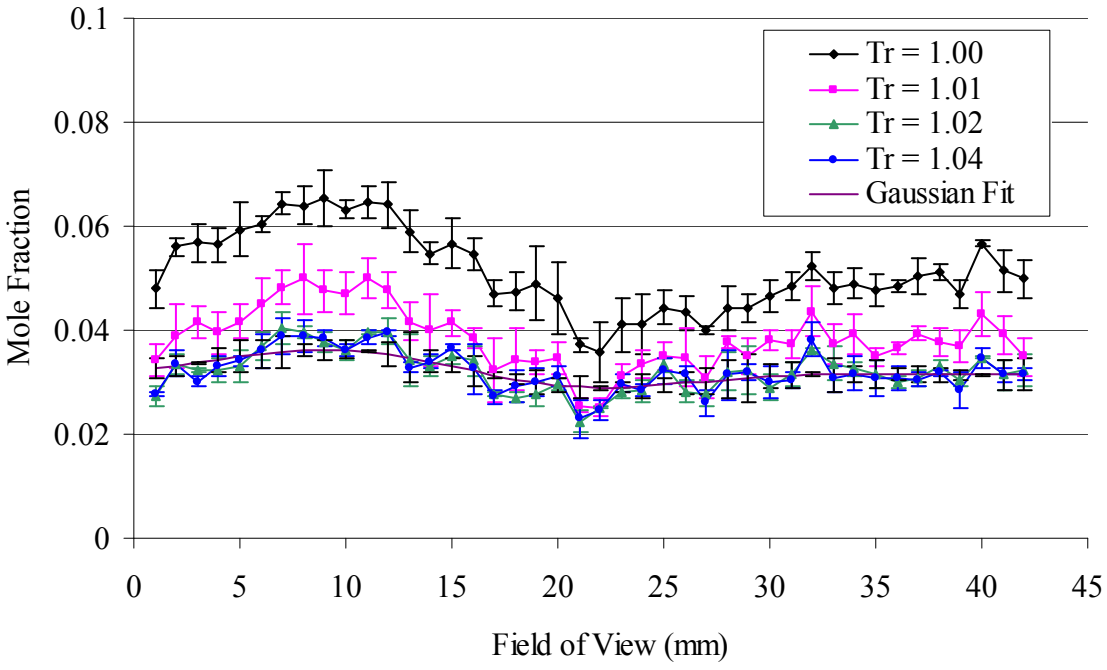

Figure 99. Methane mole fraction, X_{CH4} = 0.1 mixture, nozzle #9.

Nitrogen Mole Fractions for Different Nozzles.

Nitrogen mole fraction profiles are shown in Figure 100 through 103 as an ambient gas representing the air in the combustor. The centerline deficit is well expected because of the presence of the ethylene and methane molecules. These nitrogen mole fractions are supporting the fact that the condensed jet is not well mixed with the nitrogen. Because, the nitrogen mole fraction profile at the condensed jet has the lowest centerline value as well as widest deficit width. This fact indicates the ambient nitrogen molecules are not smeared to the condensed ethylene molecules. However, as the injection temperature increases nitrogen mole fraction is proving better mixing with the fuel. The centerline mole fraction is increased and the width is narrowed.

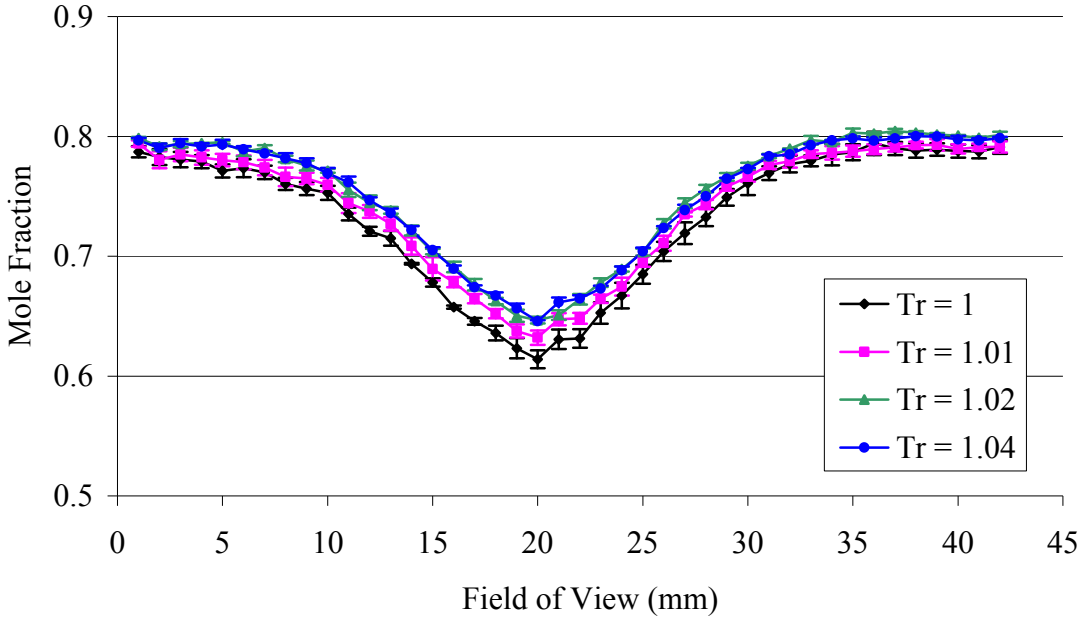

Figure 100. Nitrogen mole fraction, X_{CH4}=0.1 mixture, nozzle #1.

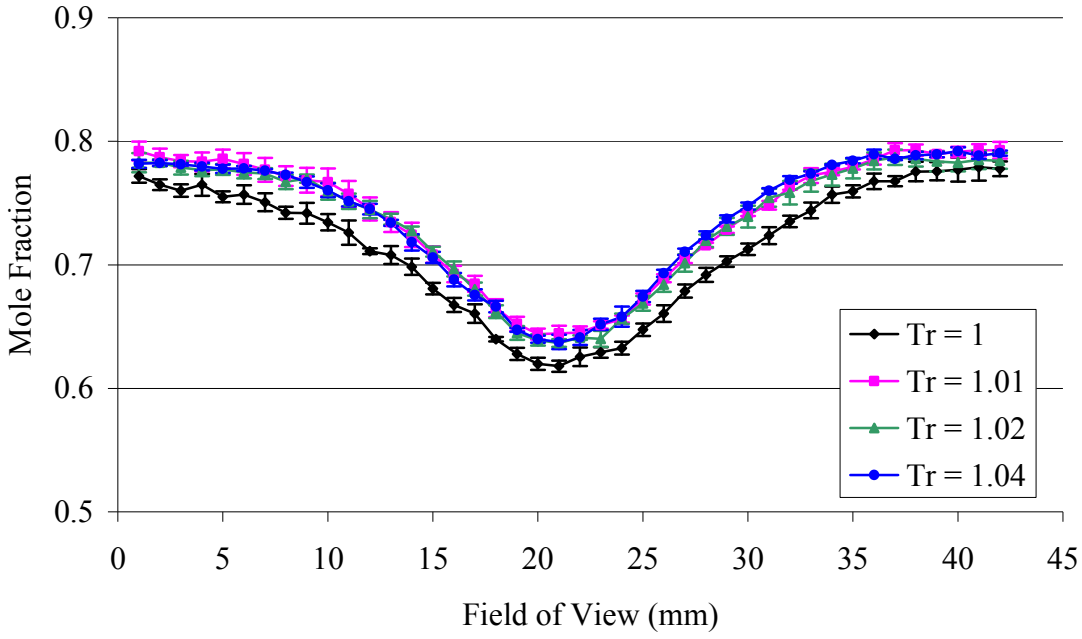

Figure 101. Nitrogen mole fraction, X_{CH4}=0.1 mixture, nozzle #6.

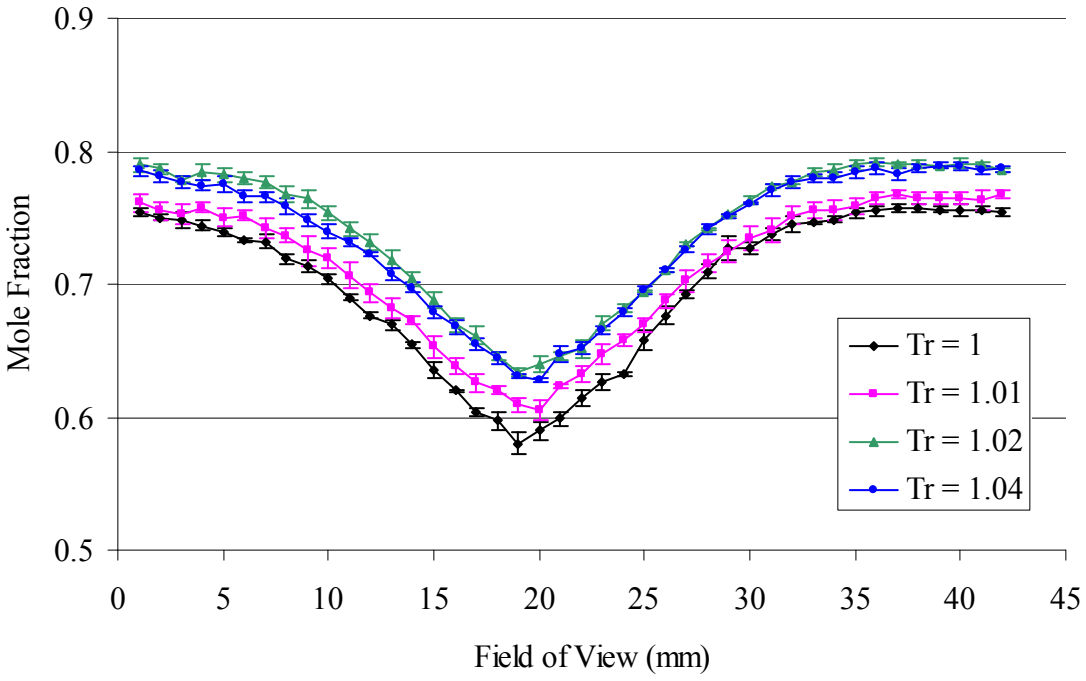

Figure 102. Nitrogen mole fraction, X_{CH4}=0.1 mixture, nozzle #7.

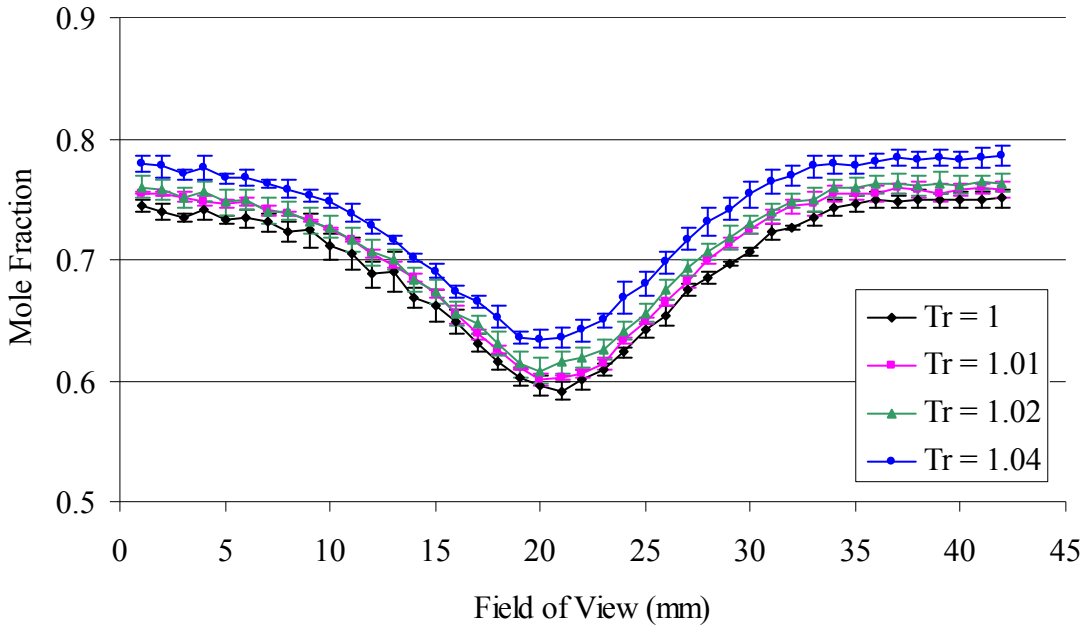

Figure 103. Nitrogen mole fraction, X_{CH4}=0.1 mixture, nozzle #9.

Mole Fraction Ratios of Ethylene to Methane for Different Nozzles.

Mole fraction ratio of ethylene to methane mole fraction is developed to determine whether there is any preferential condensation within the supercritical jet. The mole fraction ratios over the different nozzles are shown in Figure 104 through 107. The centerline ratio value is generally higher than jet edge value. Also, much lareger errors are involved at the jet center due to the small centerline mole fraction value of methane signal. The centerline value is much higher than the fuel initial mixing ratio. If two species are spreading out with the same rate, it should appear as a constant line at 9 the same as the one shown in Figure 64. However, there might be different dispersion rate is involved. The centerline value is much higher than initial mixing ratio and lower value at the jet edge region. As mentioned previously, high noise associated with methane mole fraction is primary reason for rising the centerline ratio value higher than it should be.

Every figure has large error bar at the jet center and unrealistic peak values which can be considered abnormal value. So this might be one possible reason to rise up the ratio value somewhat higher than where it should be, but generally high ratio value is observed as can be seen in Figure 104 which has relatively low signal noise.

At the methane mole fraction section, it is observed methane molecules are spreading out faster in the jet center. The differential dispersion rate between ethylene and methane gas molecule can produce high ratio value at the jet center. Methane molecules are spreading out faster than ethylene molecule at the jet center, this causes higher mole fraction value than initial mixing ratio. Possibly, methane is not condensed as much as ethylene. In other words, the condensation rate under the same temperature condition is not equal to both gases. Light methane molecule in gaseous phase is spreading out faster than heavy condensed ethylene molecules while both partially condensed molecules are spreading out at the same rate. This is possible, because the methane critical temperature is much lower than injection condition whereas the ethylene critical temperature is the same as $T_r = 1.02$ case that is the condition that could produce condensed ethylene jet, even if mixture gas exhibits different critical temperature point.

The ratio value at the jet edge is consistently lower than initial fuel mixing ratio. The gaseous phase of methane molecules are spreading faster than the ethylene. The number density of methane at the jet edge is larger than the number density in the fuel. The methane molecule presence at the jet center is relatively small. This is rising high mole fraction ratio at the jet center. Relatively large methane molecule as a result of differential spreading out rate exists at the jet edge. This is lowering the mole fraction

ratio. Consequently, there is ethylene preferential condensation within the jet based on the mole fraction ratios.

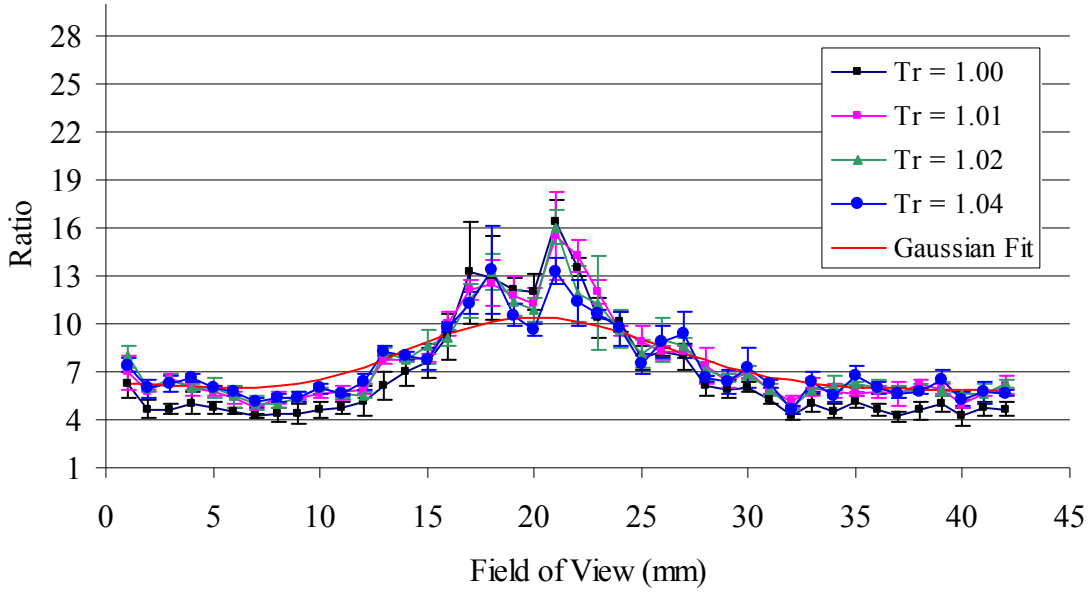

Figure 104. Mole fraction ratio, X_{CH4}=0.1 mixture, nozzle #1.

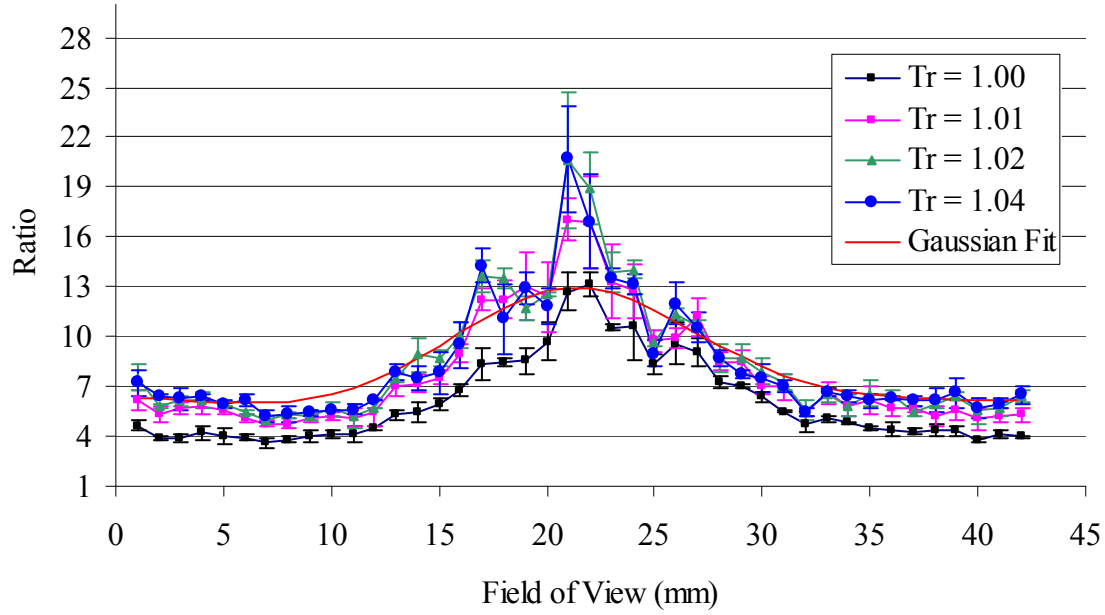

Figure 105. Mole fraction ratio, X_{CH4}=0.1 mixture, nozzle #6.

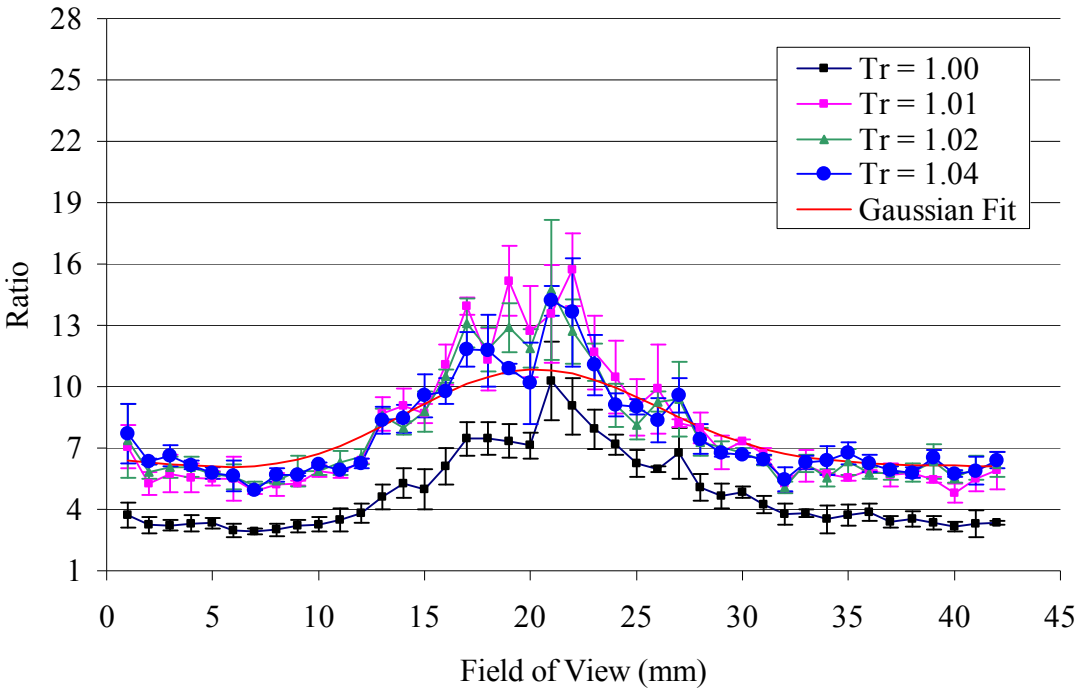

Figure 106. Mole fraction ratio, X_{CH4}=0.1 mixture, nozzle #7.

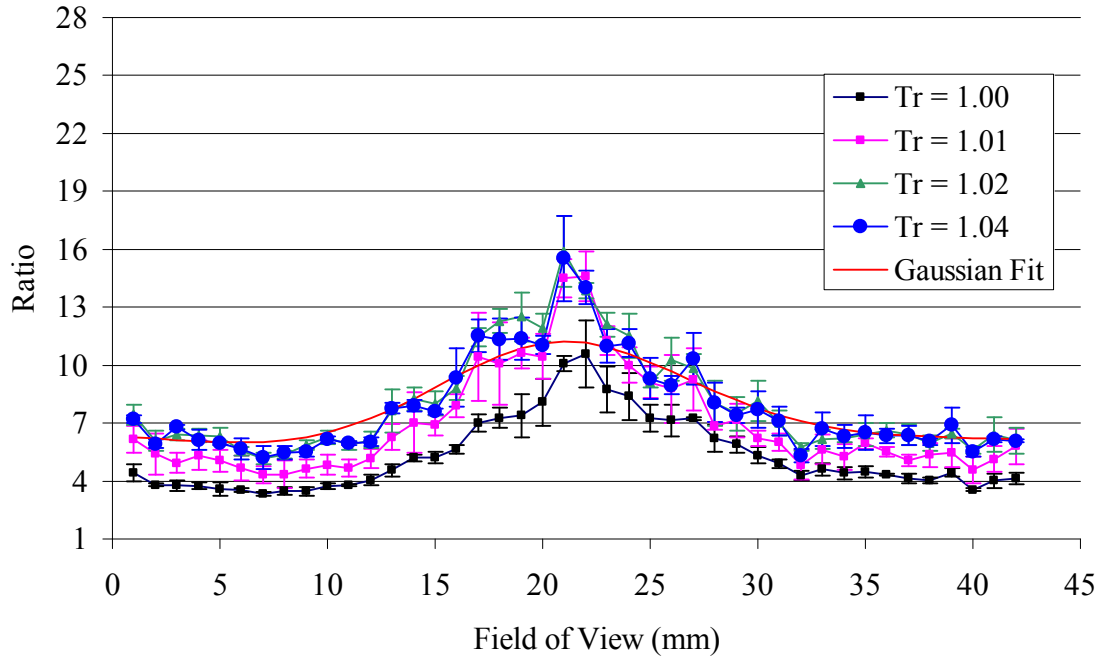

Figure 107. Mole fraction ratio, X_{CH4}=0.1 mixture, nozzle #9.

Jet Divergence Angle and Potential Core Length

The calculated potential core length is presented in the Figure 108 from the given relations by Chehroudi et al. [10]. Generally, the potential liquid core decreases as the injection temperature is increased, because the liquid jet produced at the lower injection temperature has larger density. Therefore, the potential core length is longer than gaseous jet which is increased injection temperature.

Also the jet divergence angle is calculated based on the relation given by Dimotakis et al. [22]. This relationship is depends on bulk velocity and density ratio of the sheer layer. See Appendix D for detailed relationship developed by him. The jet divergence angle is shown in Figure 109. The condensed jet has relatively small divergence angle and it is almost linearly increased as the injection temperature increases. And based on this result, nozzle #9 has a little bit larger divergence angle but the difference is not significantly large.

Consequently, the injection performance of nozzle 9 is spreading the fuel in a redial direction and nozzle #1 is injecting the fuel in a axial direction. Because the nozzle #9 has shortest potential core length while largest fuel divergence angle. In case of nozzle #1 has longest potential core while narrowest divergence angle. Therefore, the nozzle #1 is suitable injector injecting the fuel to long supersonic flow combustor such as scramjet engine.

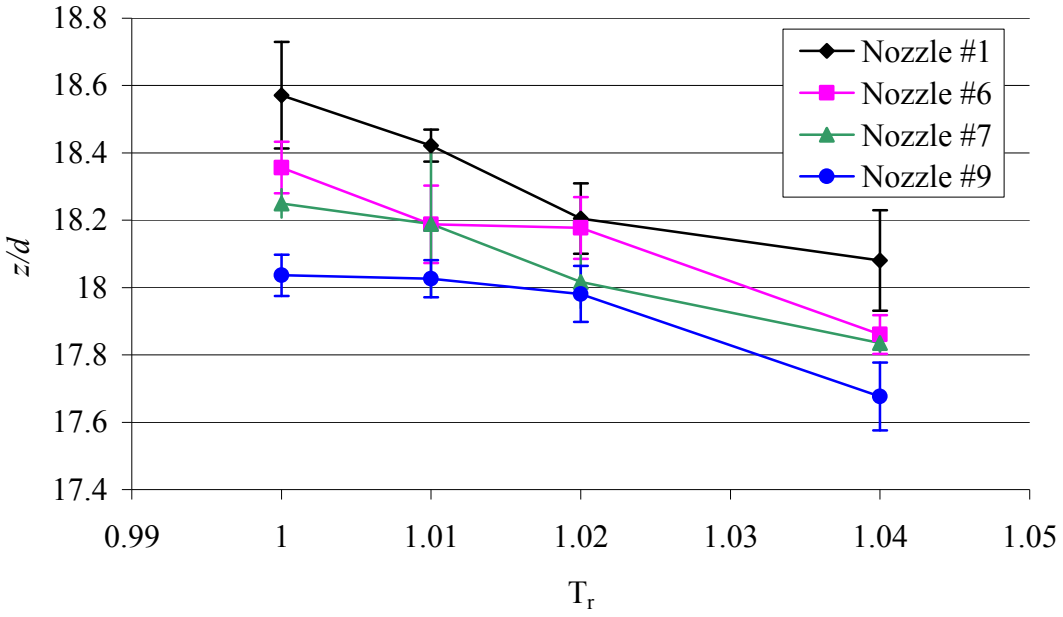

Figure 108. Potential core length for different injection temperature.

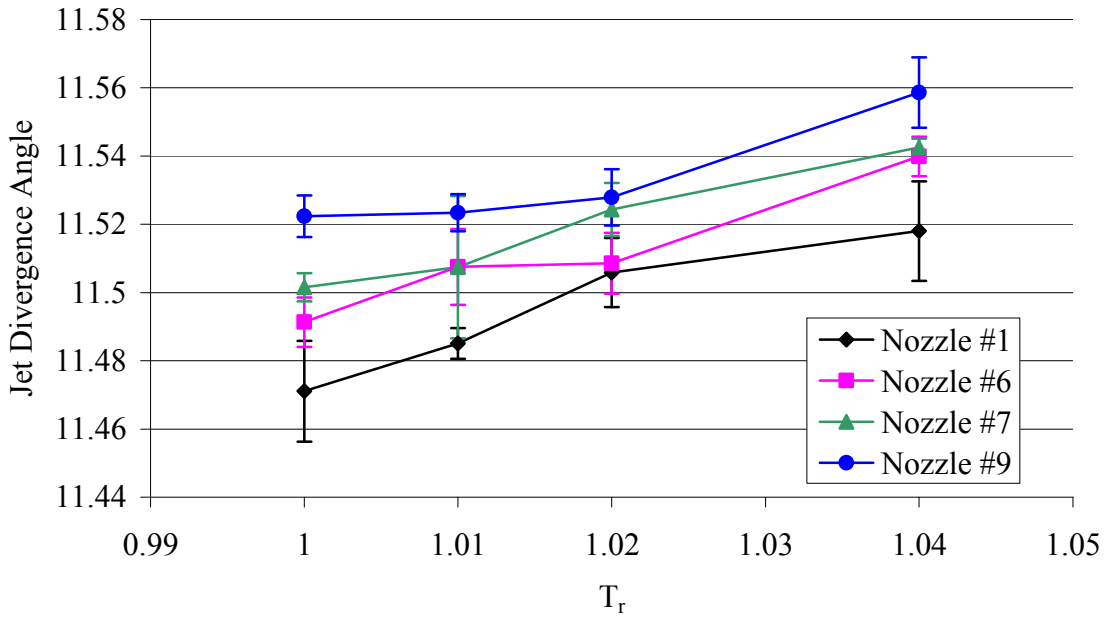

Figure 109. Jet divergence angle for different injection temperature, Units are in degrees.

V. Conclusions and Recommendations

Conclusions

Experiment Overview.

All tests are performed in a supercritical region injecting vertically into the quiescent chamber simulating the environment of a Ramjet or scramjet combustor section. Experimental research is conducted with four different research objectives of determining species distribution profile in terms of mole fraction at the down-stream location using Raman scattering technique.

This research starts with visualizing the global appearance of supercritical jet using shadowgraph imaging technique to find the jet condensation condition. Then, the Raman scattering technique is employed to identify species concentration profile at down-stream location associated with the injection condition found by shadowgraph technique.

Three different fuels are used for testing fluid along with four injection temperature conditions with four injection nozzles.

Conclusions.

All the species concentration profile is determined over the different nozzles and injection conditions. Each species mole fraction is determined based on the number density. Ethylene mole fraction profile shows that the peak mole fraction value is located at the jet centerline. Certain amounts of ethylene species are still concentrated at the jet centerline at that location. Nitrogen has lowest value at the jet centerline which is expected. The nitrogen deficit at the jet center is primarily due to the presence of ethylene

gas. Methane mole fraction also demonstrates that its peak value is maintained at the jet centerline on $X_{CH4} = 0.2$ mixture case whereas evenly distributed methane mole fraction is observed on $X_{CH4} = 0.1$ mixture case. Therefore, the first research objective determining species distribution profile is accomplished.

The second research objective is determining whether the condensed jet effects on the fuel mixing process or not. For this research objective, the test is conducted with four different injection conditions from where a lot of condensed droplets are produced within the jet to where the condensation is not significant elevating the injection temperature from the each fuel's critical temperature point. Centerline ethylene mole fraction of condensed jet ($T_r = 1.00$) is higher than other injection cases which are less condensed jets produce. As the injection temperature increases the centerline mole fraction value decreases. Whereas, the nitrogen mole fraction profile shows that the centerline value goes the other way as the injection temperature increases. In essence, the condensed jet demonstrates relatively poor mixing behavior with the air. This phenomenon is the strong evidence that the condensed jet is affecting on the fuel mixing rate and the condensed jet is not preferable from fuel mixing perspective. In addition, the methane mole fraction has the same trends to that of ethylene gas. The question of the second research objective has been answered, therefore it is also accomplished.

The third research objectively is clarifying whether there is any preferential condensation within the mixture jet or not. The mole fraction ratio of ethylene to methane mole fraction of each mixture fuel is presented for this research objective. The methane Raman signal is weak and has high SNR due to its small amount of presence in the fuel. In spite of this reason, the mole fraction ratio of each fuel case consistently demonstrates

that there is preferential condensation within the jet. The methane which is light molecule compare to ethylene is dispersing faster than ethylene (heavy molecule) at the jet center. Both mixture cases, the methane mole fraction shows almost uniform dispersion which means spreading out faster than the ethylene molecule does. This is because possibly the amount of gaseous methane molecule is larger than that of ethylene molecules, since the liquid phase ethylene jet is slowly spreading out at the jet center based on the answer of previous objective. This differential spreading out rate forms relatively high mole fraction ratio at the jet center and it becomes leveled at the outer edge of the jet by the turbulent flow effects. In short, the methane molecules (light molecule) spread out faster than the ethylene (heavy molecule) at the jet center. Therefore, the gas mole fraction ratio at the downstream location does not have evenly distributed value in stead its centerline value is higher than that of surrounds. The conclusion of third research objective is that there is ethylene preferential condensation within jet.

The last research objective is to choose the nozzle performing better mixing behavior with the air. Four nozzles are used and ethylene mole fraction profile is compared at the same injection temperature ratio. The nozzle which has the smallest centerline mole fraction value and the largest jet width is better nozzle than others. Generally every four nozzle has almost the same performance in terms of centerline value and jet width. It is hard to determine, but nozzle #1 which has no internal convergence section and shortest final flow pass length is demonstrating better performance in terms of centerline mole fraction value at each condition. Therefore, the nozzle #1 is recommended for long combustion chamber.

Consequently, experimental results satisfy four research objectives. Furthermore, this Raman study results will give enough information for comparing to the results of Computer Fluid Dynamics (CFD) which will be studied in the near future.

Recommendations for Future Research

Since the thermo-dynamical property of the supercritical fuel is unique, there might be a difference when it is injected into the air. This research is initially attempted study to identify molecular distribution profile at z/d = 100 down-stream location injecting the supercritical fuel into the quiescent chamber. It is difficult to draw conclusion of the supercritical fuel species distribution profile with single observation point. Therefore, the first recommendation for future research is to diversify the observation point vertically along the jet line; near-field or potential core region, transition region, and self-similar region. Thus the observation location might be z/d = 10, 40, 70, 100 to determine supercritical molecular species diffusion profile as it moves away from nozzle exit plane.

The methane mole fraction of the fuel is small which is the primary reason decreasing SNR and it degrades the accurate measurement of methane signal at that far down-stream location. Increasing the methane mole fraction higher than 30% would be recommended for the accurate measurement. In addition, increasing the chamber pressure also recommended to the accurate measurement for the future research.

Appendix A: Injection Nozzle Design

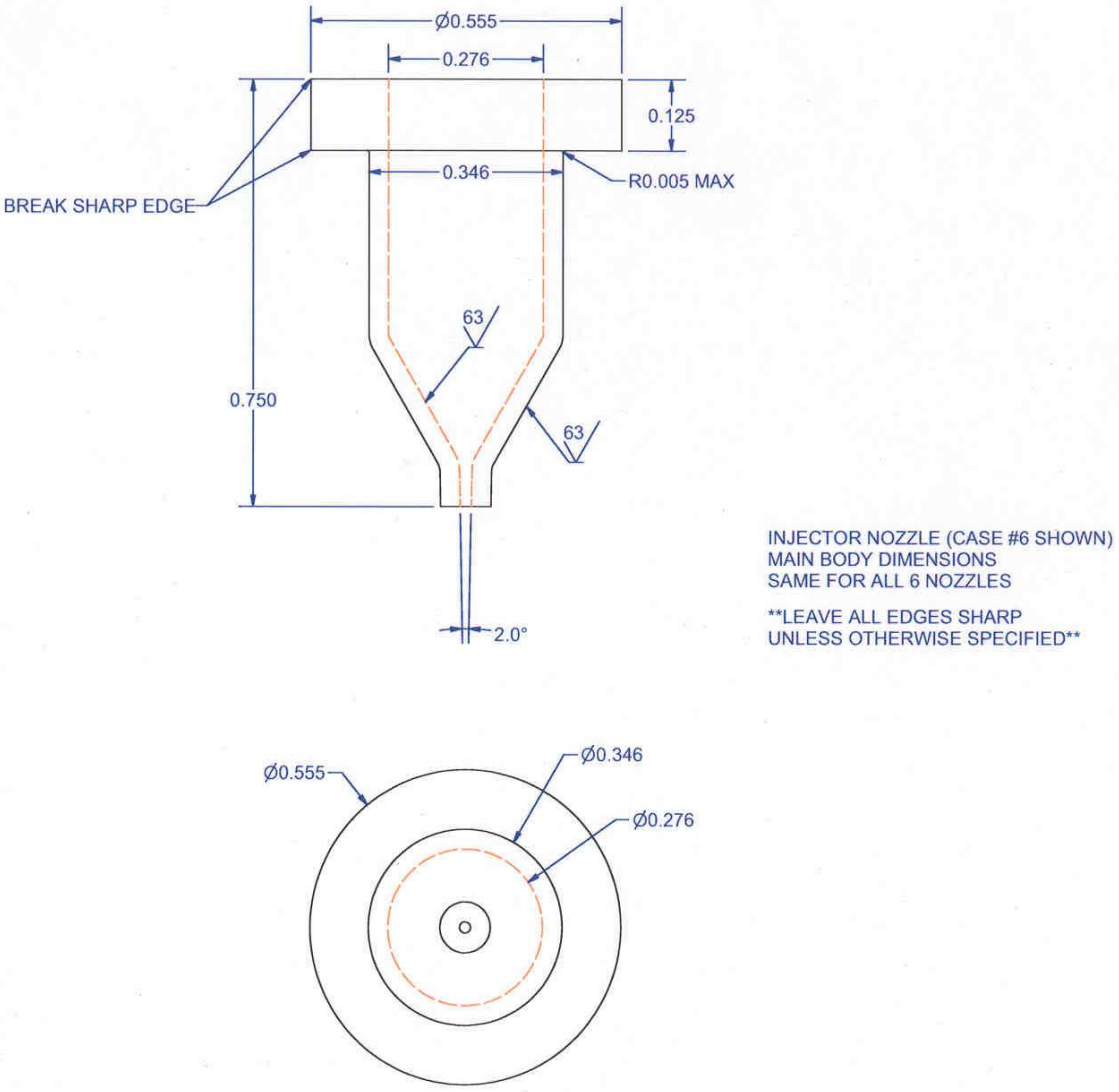

Figure 110. Injection nozzle #6 base design, units are in inches.

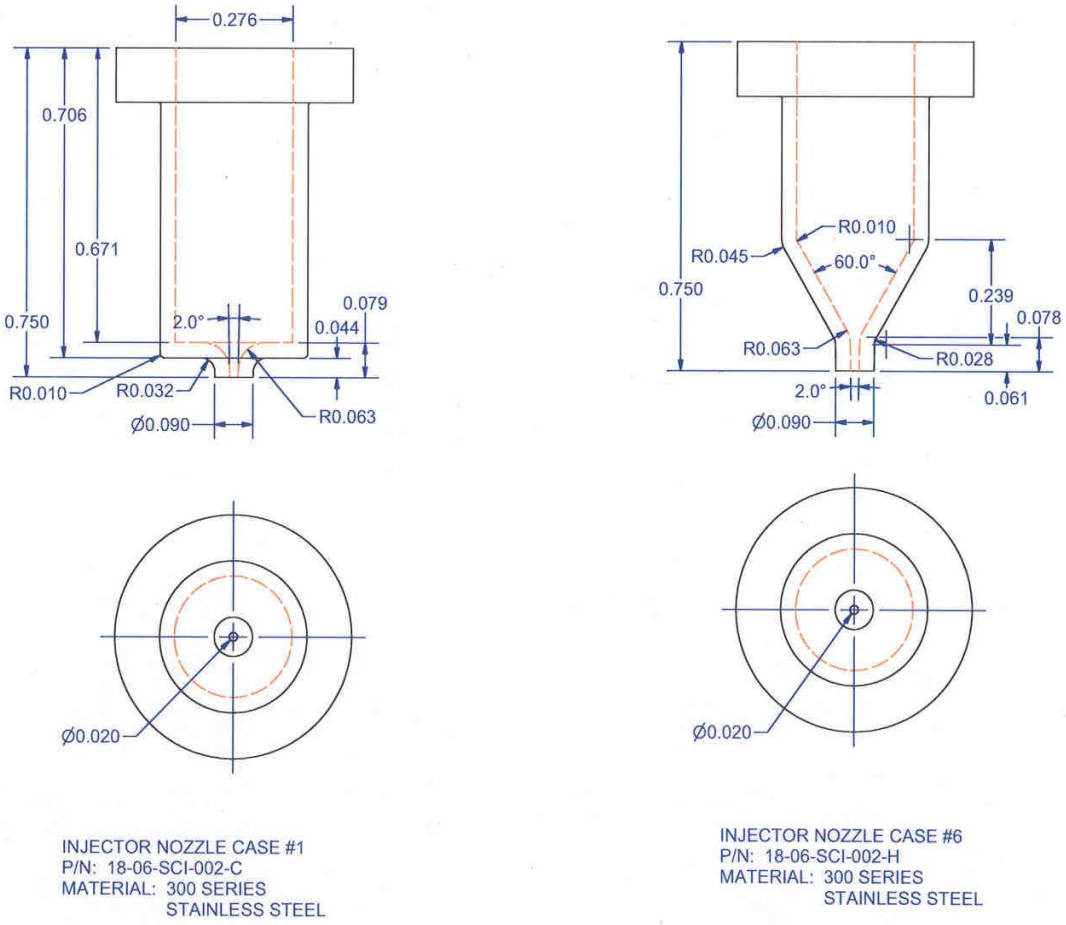

Figure 111. Injection nozzle #1 and #6 designs.

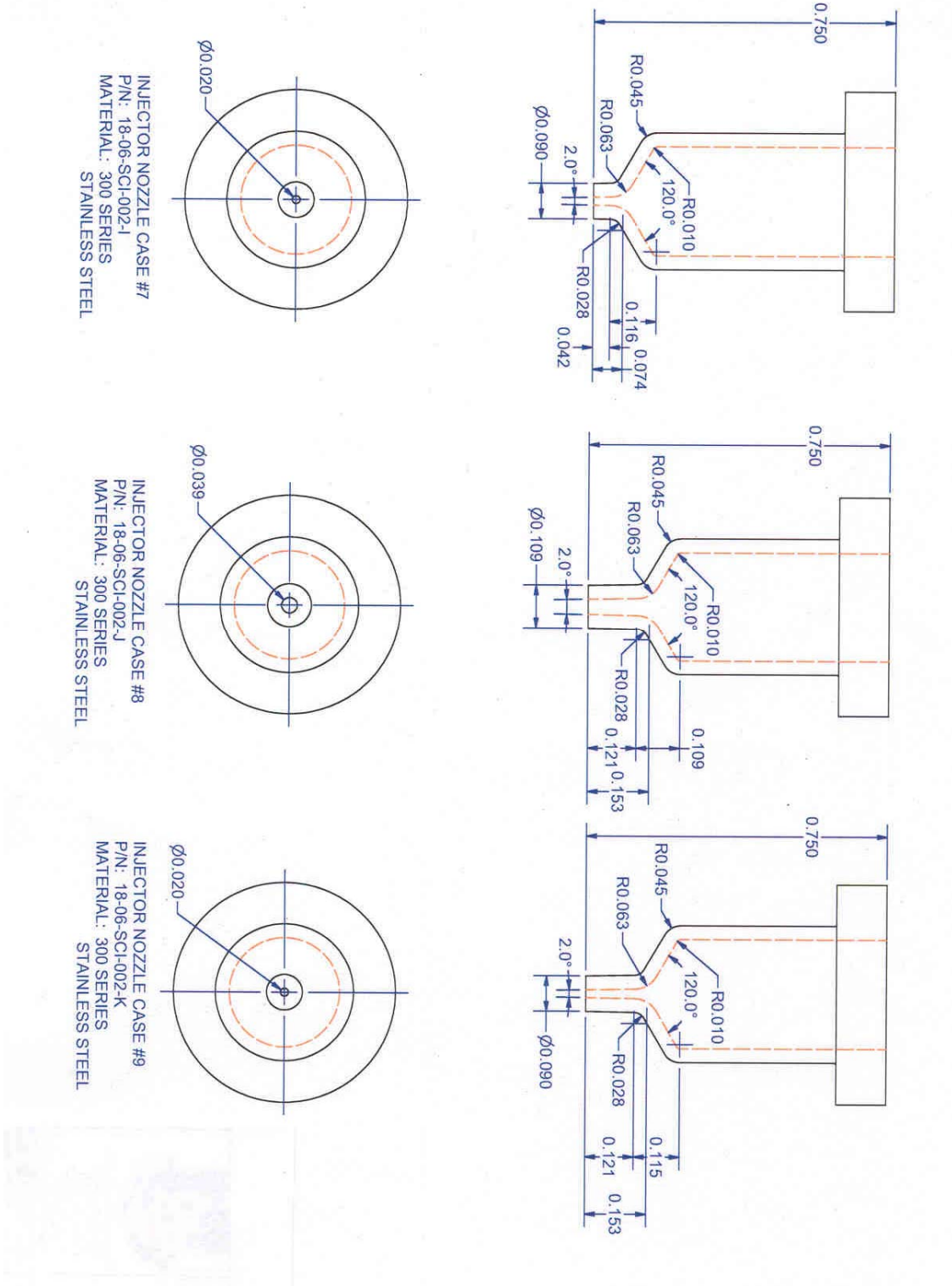

Figure 112. Injection nozzle #7, #8, and #9 designs.

Appendix B: Least Square Method

The method of least square is used to find correlations to calibration of number density of nitrogen and methane, ethylene. The purpose of the method of least square is to minimize the sum of the squares of the fit's offset (residual). If there is no experimental error, the two sets of data point will form the line Y=C + DX. But, if there is error, the line can be formed and it is necessary to find the best fitted line between the two points. Consider seven different points, (x_i, y_i), i = 1..7.

$$\begin{aligned} C + Dx_1 &= y_1 \\ C + Dx_2 &= y_2 \\ &\vdots \\ C + Dx_7 &= y_7 \end{aligned}$$

There are two unknowns and seven equations. If there is an error, this set of equation will not have a solution. Rewriting this equation set in a matrix form,

$$\begin{pmatrix} 1 & x_1 \\ 1 & x_2 \\ 1 & x_3 \\ 1 & x_4 \\ 1 & x_5 \\ 1 & x_6 \\ 1 & x_7 \end{pmatrix} \begin{pmatrix} C \\ D \end{pmatrix} = \begin{pmatrix} y_1 \\ y_2 \\ y_3 \\ y_4 \\ y_5 \\ y_6 \\ y_7 \end{pmatrix}, \quad \text{or} \quad AX = b$$

It can't be solved because the points are not on a line. Therefore they are solved by least squares:

$$A^T A \hat{X} = A^T b, \quad or \quad \hat{X} = (A^T A)^{-1} A^T b$$

In this study, variable, x_i, (i = 1..7) are the species number density determined by the perfect gas law. b is the corresponding signal intensities.

Appendix C: Supercritical Fuel Injection System and Operating Procedure

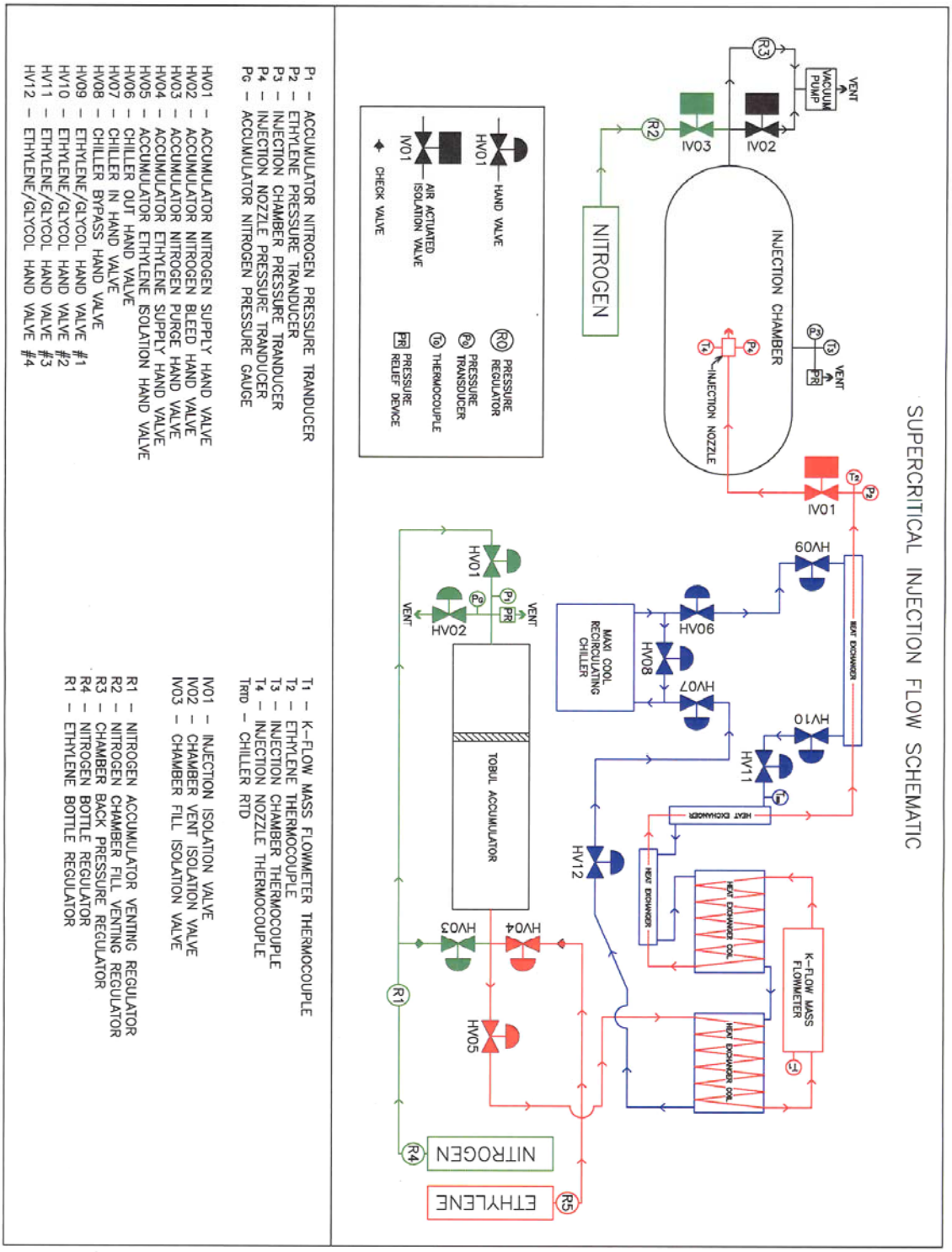

Figure 113. Schematic of supercritical injection flow.

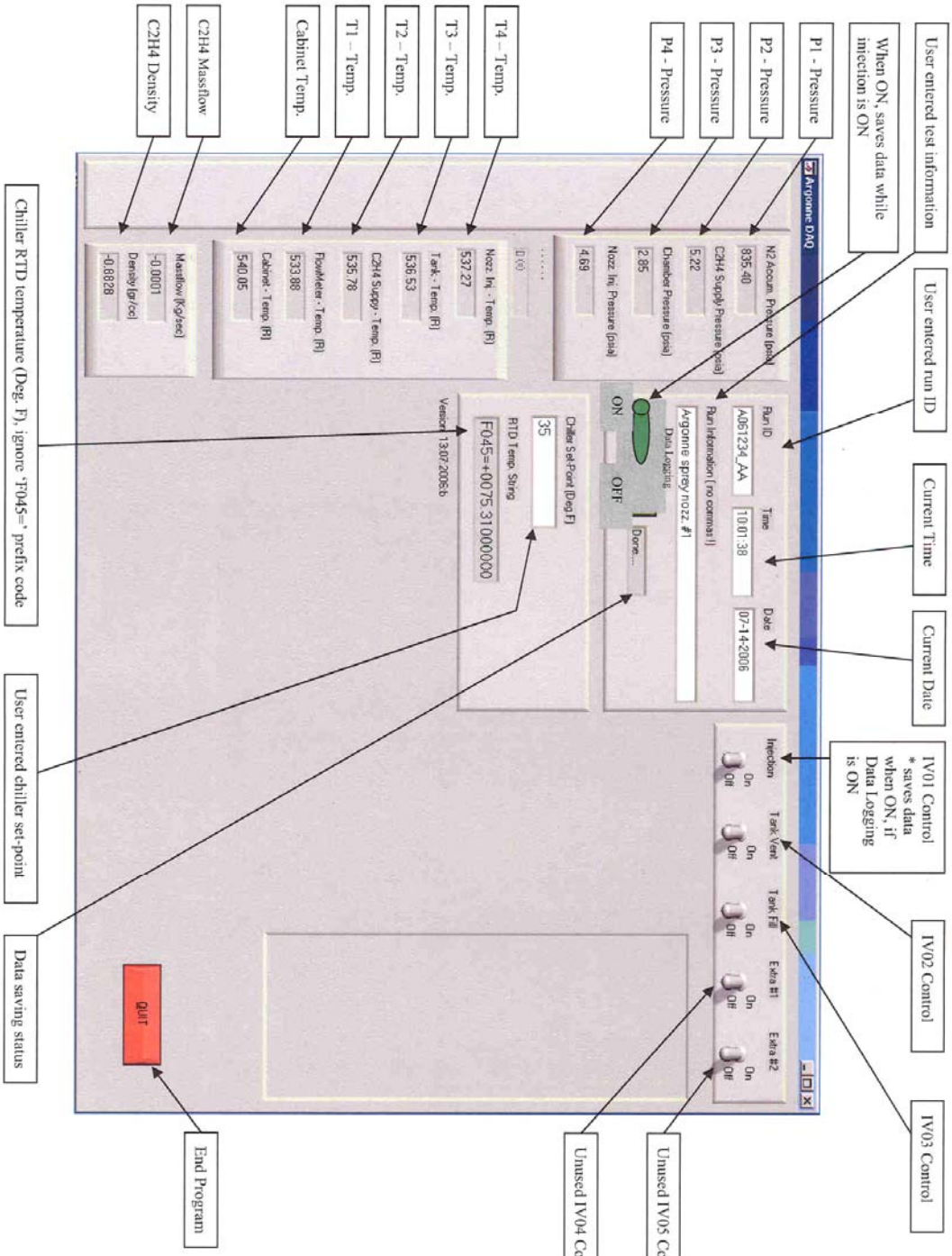

Figure 114. Supercritical injection jet control program.

Set Up Preparation:

1. Plumbing – verify all connections are made and tight
    a. Verify shop air is ON for the venturi vacuum pump
    b. Verify shop air is ON for the control cart supply
2. Maxi-Cool Recirculating Chiller
    a. Plug Chiller in – 208V single phase
    b. Verify 'MAINS' light on chiller is on
    c. Verify all connections are complete to make a closed loop system
    d. Open Hv06, HV07, HV09, HV10, HV11 and HV12
    e. Close HV08
    f. Pull Red Mushroom Out
    g. Verify chiller is NOT in Remote – Light on Remote button should be OFF – Press Remote button to switch between Local and Remote
    h. Check / Change chiller set point
        i. Press either the Up or Down button – SP will appear on the display. Followed by the actual set point (°F)
        ii. Change the set point using the Up and Down buttons
    i. Press the START button to activate the chiller
    j. Press the PUMP button to turn the pump on
    k. Press the REFR button – chiller will approach the set point
    l. Press the REMOTE button to put the chiller in remote mode
3. Instrument / Control Box
    a. Plug terminal strip in
    b. Turn terminal strip switch ON
        i. Verify power is on to the K-Flow Mass Flowmeter (Panel should illuminate)
    c. Verify there is pressure to the shop air supply for the air actuated valves – 80 psi min.
4. Computer(s)
    a. If using remote terminal – connect both computers to network switch
    b. Turn computer(s) ON
    c. Enter 'Argonne' account (no password needed) – Dell Laptop (Steven's)
        i. Click Argonne icon to start program
        ii. After a few seconds: pressure, temperature, and mass flow measurements should display
        iii. Verify communication with the chiller
            1. At chiller, verify RX/TX light is blinking – confirms RS-232 communication
            2. RTD Temp.String should read similar to this: F045=+0067.9400
            3. Verify chiller set point is correct
                a. If not, change set point by entering value into set point box
                b. At the chiller, press Up or Down button see new set point
    d. Using Linux – enter 'visitor' account (password: visitor) – Toshiba Laptop
        i. Open an 'xterm' terminal – Right click mouse on desktop, select new terminal
        ii. Enter 'vncviewer'
        iii. Enter '200.200.200.99' (address to Dell Laptop)
        iv. Windows desktop should appear on the Toshiba Laptop

v. Use F8 key and select Full Screen

5. Purging Accumulator
   a. Close HV01 and HV04
   b. Open HV02, HV03, and HV05
   c. Back R1 all the way off
   d. Verify nitrogen supply is connected
      i. If using bottle, back R4 (N_2 bottle regulator) all the way off
      ii. Open N_2 bottle valve
      iii. Adjust R4 to ≈ 200 psi
      iv. Adjust R1 to ≈ 200 psi
      v. Verify system charged with N_2 by looking at P_2
      vi. Close HV03
      vii. Open IV02
      viii. Open IV01 to vent N_2 from the accumulator
      ix. Close HV02
      x. Open HV01 to pressurize opposite side of the accumulator
      xi. Wait until P_2 reaches atmospheric pressure
6. Vacating Accumulator – necessary before initial filling of accumulator only
   a. Verify that there is NO nozzle installed
      i. See Changing Nozzles – Step 8 for assistance
   b. Open HV02 and HV05
   c. Close HV01, HV03, and HV04
   d. Verify IV03 is Closed
   e. Open IV01 and IV02
   f. Wait until P_3 reaches 3 psia
   g. Close IV01 and IV02
7. Filling Accumulator
   a. Close HV01 and HV03
   b. Open HV02, HV04, and HV05
   c. Verify IV01 is Closed
   d. Verify Ethylene bottle is connected to the ¼" tube ethylene supply fitting
      i. Note: Ethylene bottles will have left handed threads
      ii. Back off R5 – Ethylene bottle regulator
      iii. Open valve on the ethylene bottle
      iv. Adjust R5 (ethylene bottle regulator) to desired pressure
   e. Close Ethylene bottle valve and back off R5
   f. Close HV02 and HV04
   g. Open HV01
   h. Adjust R1 to desired pressure
8. Changing Nozzles
   a. Verify IV01 is closed
   b. Verify injection is at atmospheric pressure – P_3
   c. Disconnect 1/16" tube from pressure transducer – P_4

d. Disconnect thermocouple connector – T_4
e. Disconnect ½" flex hose from IV01 and nozzle tube
f. Loosen bolts connecting 2" – 150# flanges – (Qty: 4)
g. Remove bolts connecting 2" – 150# flanges – (Qty: 4)
h. Delicately pull injector nozzle assembly out of the injection chamber
i. Loosen the six 6-32 socket head cap screws holding nozzle in place
j. Remove the six 6-32 socket head cap screws
k. Place nozzle back in its appropriate plastic bag and slot in the plastic case
l. Remove new nozzle from plastic bag and case, replace plastic bag in corresponding slot in case
m. Check condition of the O-ring that seals the nozzle – replace if necessary
n. Hand tighten the six 6-32 socket head cap screws
o. Tighten the six 6-32 socket head cap screws going in star pattern
p. Check flange O-ring, replace if necessary
q. Delicately put injector nozzle assembly into the injection chamber
r. Verify Up arrow is pointing up
s. Replace four nuts and bolts to connect the nozzle assembly to the chamber
t. Tighten in a star pattern
u. Connect 1/16" pressure tube to P_4 pressure transducer
v. Connect thermocouple wire to T_4 thermocouple
w. Connect ½" flex hose from IV01 to nozzle tube

Operating Procedures:

1. Initially Filling Injection Chamber with Nitrogen at New Desired Pressure
    a. Open IV02
    b. Using vacuum pump, vacate chamber to ≈ 3 psia
    c. Close IV02
    d. Open nitrogen bottle valve to R2 inlet
    e. Set R2 to slightly higher than desired chamber pressure
    f. Open IV03
    g. Adjust R3 to desire chamber pressure
    h. Once chamber reaches desired pressure, Close IV03
    i. Repeat steps e-h as necessary
2. Re-Filling Injection Chamber with Nitrogen at the same pressure
    a. Open IV02
    b. Using vacuum pump, vacate chamber to ≈ 3 psia
    c. Close IV02
    d. Open IV03
    e. Once chamber reaches desired pressure, Close IV03
3. Injecting Ethylene into Chamber
    a. Verify Data Logging Switch is turned ON – This logs data when IV01 is Open
        i. Note: This data is stored in c:\streby\argonne_data.txt. ***DO NOT*** open the file with excel while control program is running. You can copy the file to a different name if you need to open it.
    b. Verify P2 is at desired pressure
        i. Adjust R1 accordingly
    c. Verify T2 is at desired temperature
        i. Adjust chiller set point accordingly
    d. Verify P3 is at the desired pressure
        i. See steps 7 – 8 to adjust P3
    e. Verify IV02 and IV03 are Closed
    f. Open IV01 to inject
    g. Wait for K-Flow Mass Flowmeter to give steady measurement
    h. Close IV01 to stop injection

Shutdown Procedures:

1. Venting excess Ethylene
    a. Close Ethylene bottle valve
    b. Back R5 all the way off
    c. Open IV01 and IV02
    d. Wait until P_2 is reading atmospheric pressure, then continue
    e. Repeat Step 5 of the Set Up Preparation – Purging Accumulator
    f. Close HV04, HV03, and HV05
    g. Disconnect Ethylene bottle from control cart
2. Venting excess Nitrogen
    a. Close Nitrogen bottle valve
    b. Back R4 all the way off
    c. Back R1 all the way off
    d. Open HV02
    e. Wait until P_G is at atmospheric pressure
    f. Close HV01 and HV03
    g. Disconnect Nitrogen bottle from control cart
3. Chiller Shut Down
    a. Turn off REMOTE
    b. Turn off REFR
    c. Turn off PUMP
    d. Press STOP
    e. Press Red Mushroom
    f. Unplug Chiller
4. Computer(s)
    a. Dell Laptop
        i. Press Quit button to exit Argonne program
        ii. Logoff or Shutdown the computer
    b. Toshiba Laptop
        i. Press F8 key – select quit to end VNC remote mode
        ii. Logoff or Shutdown the computer
5. Control Cart
    a. Turn power off to control cart
    b. Turn shop air pressure off to venturi vacuum pump

Appendix D: Jet Divergence Angle Equation

Jet divergence angles of different nozzles calculated using the relationship presented by Dimotakis et al. [22]. This relationship is based on bulk velocity and density ratio of the shear layer.

$$\delta = 0.17 \left\{ \frac{\left(1 - \frac{u_\infty}{u_0}\right)}{\left[1 + \left(\frac{\rho_\infty}{\rho_0}\right)^{1/2} \left(\frac{u_\infty}{u_0}\right)\right]} \right\} \left\{ 1 + \left(\frac{\rho_\infty}{\rho_0}\right)^{1/2} - \frac{\left[1 - \left(\frac{\rho_\infty}{\rho_0}\right)^{1/2}\right]}{\left[1 + 2.9 \frac{\left(1 + u_\infty / u_0\right)}{\left(1 - u_\infty / u_0\right)}\right]} \right\} \tag{20}$$

For this study, a supercritical jet is injected into a quiescent chamber, the velocity ratio is zero, simplifying the following equation.

$$\delta = 0.17 \left[1 - \left(\frac{\rho_\infty}{\rho_0}\right)^{1/2} \right] \tag{21}$$

Appendix E: Ethylene Vibrational Mode

There are six different kinds of vibrational modes for every molecules [23]. Generally, it has stretching and bending vibrations. Stretching vibration has symmetric and asymmectric vibrations. Bending vibaration has in-plane and out of plane vibrations. In-plane vibration has rocking and scissoring vibrations while out of plane has wagging and twisting vibrations [23].

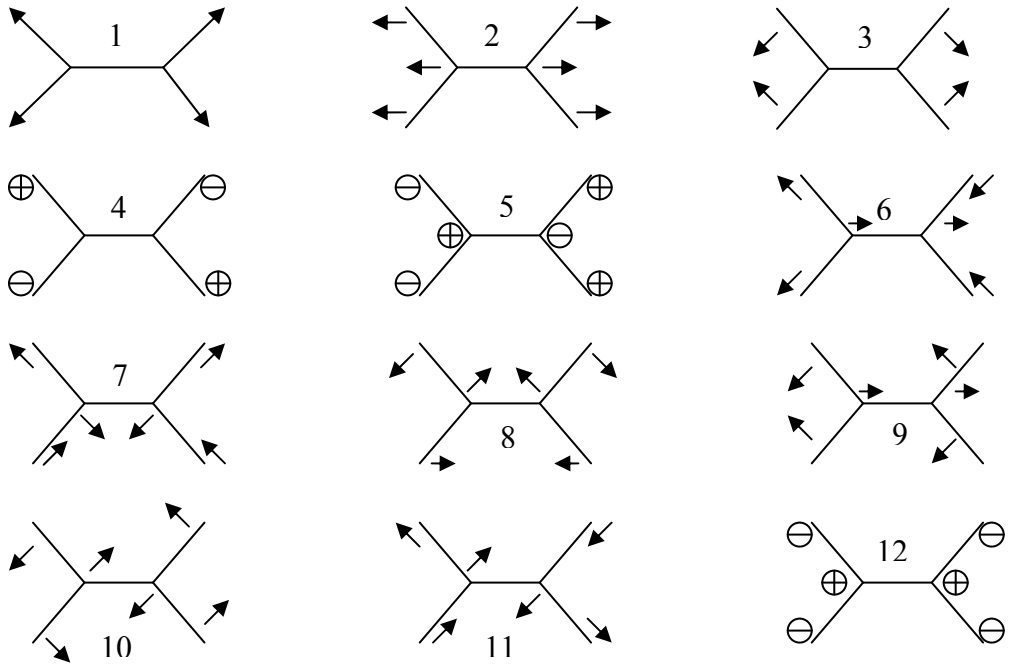

Figure 115. Ethylene molecule's vibrational modes [23].

Ethylene molecule has twelve different types of vibration as shown in Figure 108. 1 is a CH2 symmetric stretching, 2 is a CC stretching, and 3 is a CH2 scissoring. 4 is a CH2 twisting, 5 is a asymmetric CH2 stretching, and 6 is a CH2 rocking. 7 and 8 are CH2 wagging, 9 is a CH2 asymmetric stretching, and 10 is a CH2 rocking. 11 is CH2 symmetric stretching, 12 is a CH2 scissoring mode. Each vibrational mode has specific frequencies that can be detected by molecular spectroscopy. Table 6 is showing the

specific Raman frequencies corresponding to the ethylene vibrational modes [24]. Other vibrational mode is not the Raman active. According to Table 6, ethylene I is a vibrational mode 3 (v_3), ethylene II is a vibrational mode 2 (v_2), and ethylene III is a vibrational mode 1 (v_1).

Table 6. Raman shift for ethylene molecule's vibrational mode [24].

Mode	Type of mode	Raman frequency (cm^{-1})	Phase
1	CH2 symmetric stretching	3026.4	Gas
2	CC stretching	1622.6	Gas
3	CH2 scissoring	1342.2	Gas
5	CH2 asymmetric stretching	3102.5	Gas
6	CH2 rocking	1236	Liquid
8	CH2 wagging	943	Liquid

References

1. Edwards, T., "USAF Supercritical Hydrocarbon Fuels Interests", AIAA paper 93-0807*,* January 1993

2. Maurice, L., Edwards, T., and Griffiths, J. "Liquid Hydrocarbon Fuels for Hypersonic Combustion". Progress in Astronautics and Aeronautics V189: *Scramjet Propulsion,* Ed. E.T. Curran and S.N.B. Murthy. American Institute of Aeronautics and Astronautics, Inc. VA, 2000, pp 757-822.

3. Edwards, T., Anderson, S. D., "Results of High Temperature JP-7 Cracking Asscssment," AIAA Paper 93-0806, AIAA Aerospace Sciences Meeting, Reno, NV, Jan. 1993.

4. Lin, K.-C., Cox-Stouffer, S. K., Kennedy, P.J., and Jackson, T. A., "expansion of Supercritical Methane/Ethylene Jets in a Quiescent Subcritical Environment" *AIAA paper 03-0483,* January 2003.

5. Wu, P.-k., Shahnam, M., Kirkendall, K. A., Carter, C. D., and Nejad, A. S., "Expansion and Mixing Processes of Underexpanded Supercritical Fuel Jets Injected into Superheated Conditions", *Journal of Propulsion and Power,* Vol. 15, No. 5, pp.642-649, 1999.

6. http://www.pnl.gov/supercriticalfluid/about.stm

7. Huber, M. L., NIST Standard Reference Database 4: NIST Thermophysical Properties of Hydrocarbon Mixtures Database (SUPERTRAPP), Version 4, 1999.

8. Lin, K.-C., Cox-Stouffer, S. K., and Jackson, T. A., "Structures and Phase Transition Processes of Supercritical Methane/Ethylene Mixtures Injected into a Subcritical Environment" *Combustion and Science Technology,* 178: pp 129-160, 2006.

9. Crist, S., Sherman, P. M., and Glass, D. R., "Study of the highly underexpanded sonic jet", AIAA Journal, 4, 68. 1968.

10. Branam, R., and Mayer, W., "Characterization of Cryogenic Injection at Supercritical Pressure," *Journal of Propulsion and power*, Vol. 19, No. 3, pp. 342-355, May/Jun 2003

11. Chehroudi, B., Talley, D., and Coy, E., "Initial Growth Rate and Visual Characteristics of a Round Jet into a Sub- to Supercritical Environment of Relevance to Rocket, Gas Turbine, and Diesel Engines," AIAA paper number 99-0206, 37th AIAA Aerospace Sciences Meeting and Exhibit, Reno, NV, pp. 6-7, 1999.

12. Schetz, J. A., "Injection and Mixing in Turbulent Flow", *Progress in Aeronautics and Astronautics*, Vol 68, AIAA 1980, pp. 19-84.

13. Ewen, smith., and Geoffrey, Dent., Modern Raman Spectroscopy: A Practical Approach. Southern Gate : John Wiley and sons Ltd. England. 2005.

14. Schrader, B., Infrared and Raman Spectroscopy; Chapter 4. New York : VCH Publishers Inc. 1995.

15. Eckbreth, Alan C., Laser Diagnostics for Combustion Temperature and Species. Cambridge: Abacus. 1995.

16. Ferraro, J.R., and Kazuo, N. Introductory Raman Spectroscopy. San Diego: Academic Press. 1994.

17. McCreery, R. L., Raman Spectroscopy for Chemical Analysis. John Wiley & Sons, Inc. 2000.

18. Holman, J. P., Experimental Methods for Engineers. McGrow-Hill, Co. 2001.

19. Yang, Wen-Jei. Handbook of Flow Visualization. Taylor and Francis. 1989.

20. www.geocities.com

21. http://webbook.nist.gov

22. Dimotakis, P.E., "Two-dimensional Shear-layer Entrainment," *AIAA Journal*, vol. 24, no. 11, pp. 1791-1796, 1986.

23. www.shodor.org/succeed/compchem/labs/vibrations/

24. www.webbook.nist.gov/cgi/cbook/

Vita

Captain Young Man An, Republic of Korea Army, graduated from Korea Military Academy where he graduated with a Bachelor of Science degree in Physics in March 2000. He was commissioned as a 2nd lieutenant and assigned to 28th infantry division as a platoon leader. He served as an aid-de-camp of a division commander for one year. He entered Infantry Officer's Advanced Course for six months where he could broaden and enrich the knowledge on military operations and command philosophy. Upon graduation he was selected to the Graduate School of Engineering and management, Air Force Institute of Technology.

Upon achievement of a masters of science in Aeronautical Engineering, Capt. An will continue on to conduct his military career assuming company commander of 11th Mechanized Infantry Division in the First ROK field army, South Korea.

REPORT DOCUMENTATION PAGE

Form Approved
OMB No. 074-0188

1. REPORT DATE *(DD-MM-YYYY)*	**2. REPORT TYPE**	**3. DATES COVERED** *(From – To)*
13-09-2007	Master's Thesis	August 2005 – September 2007

4. TITLE AND SUBTITLE
RAMAN SCATTERING STUDY OF SUPERCRITICAL BI-COMPONENT MIXTURES INJECTED INTO A SUBCRITICAL ENVIRONMENT

5a. CONTRACT NUMBER
5b. GRANT NUMBER
5c. PROGRAM ELEMENT NUMBER

6. AUTHOR(S)
An, Young Man., Captain, ROKA

5d. PROJECT NUMBER
5e. TASK NUMBER
5f. WORK UNIT NUMBER

7. PERFORMING ORGANIZATION NAMES(S) AND ADDRESS(S)
Air Force Institute of Technology
Graduate School of Engineering and Management (AFIT/EN)
2950 Hobson Way, Building 640
WPAFB OH 45433-8865

8. PERFORMING ORGANIZATION REPORT NUMBER
AFIT/GA/ENY/07-S01

9. SPONSORING/MONITORING AGENCY NAME(S) AND ADDRESS(ES)
AFRL Propulsion Directorate
1950 5th street WPAFB OH 45433-7251

10. SPONSOR/MONITOR'S ACRONYM(S)
AFRL/PRAS

11. SPONSOR/MONITOR'S REPORT NUMBER(S)

12. DISTRIBUTION/AVAILABILITY STATEMENT
APPROVED FOR PUBLIC RELEASE; DISTRIBUTION UNLIMITED.

13. SUPPLEMENTARY NOTES

14. ABSTRACT
This research studies the species distribution profiles of methane/ethylene bi-components at downstream locations filled with subcritical nitrogen in a closed chamber. Unique thermodynamic and transport properties of supercritical fluids along with phase transition phenomena during fuel injection process can significantly change combustion characteristics inside a scramjet combustor. Plume properties of supercritical jets are of great interests to the studies of fuel/air mixing and subsequent combustion. The primary goal of this research is to help to clarify whether there is any preferential condensation within the condensed jets. The Raman Scattering technique is used to quantify spatial distribution of injected methane and ethylene. Each species distribution profile is developed in terms of mole fraction. Results demonstrated there is ethylene preferential condensation within the supercritical bi-component mixture of the jet. It also showed the condensation phenomenon is less desirable for combustion.

15. SUBJECT TERMS
Ethylene/methane mixture fuel, Supercritical injection jet, Raman scattering, Condensation, Mole fraction profile

16. SECURITY CLASSIFICATION OF:			**17. LIMITATION OF ABSTRACT**	**18. NUMBER OF PAGES**	**19a. NAME OF RESPONSIBLE PERSON**
a. REPORT	**b. ABSTRACT**	**c. THIS PAGE**			Dr. Paul I. King
U	**U**	**U**	**UU**	154	**19b. TELEPHONE NUMBER** *(Include area code)* (937) 255-3636, ext 4628 (Paul.King@afit.edu)

Standard Form 298 (Rev. 8-98)
Prescribed by ANSI Std. Z39-18